Forschungszentrum Jülich

Institut für Schicht- und Ionentechnik

Electron Spin Resonance Studies on Microcrystalline Silicon

Joachim Müller

JUL-4193

Electron Spin Resonance Studies on Microcrystalline Silicon

Joachim Müller

Berichte des Forschungszentrums Jülich ; 3615
ISSN 0944-2952
Institut für Schicht- und Ionentechnik Jül-3615
D82 (Diss. RWTH Aachen)

Zu beziehen durch: Forschungszentrum Jülich GmbH · Zentralbibliothek
D-52425 Jülich · Bundesrepublik Deutschland
☎ 02461/61-6102 · Telefax: 02461/61-6103 · e-mail: zb-publikation@fz-juelich.de

Abstract: VHF-PECVD was used to prepare undoped as well as p- and n-type microcrystalline silicon with gas phase doping levels between 1 and 160 ppm and high crystalline volume fractions. The material was studied by steady state and transient electron spin resonance (ESR) at temperatures between 4.2 and 300 K in the dark and under light illumination. The results are related to transport measurements, and the nature and energy position of the respective electronic states is clarified. Two resonances of defect states appear at g-values of 2.0043 and 2.0052 over a wide doping range pointing to either a wide distribution in energy (0.6 eV) or considerable potential fluctuations. A third resonance (g-value around 1.998) is due to donor, conduction band or conduction band tail states, the respective occupancies depending on both temperature and doping level. In particular, for n-type samples the spin density of this latter resonance equals the donor density over two orders of magnitude. Hyperfine interaction with phosphorus nuclei is only observed at intermediate doping levels. A value of 12 Å is found for the localization length of the donor wavefunction. The conduction process at temperatures below 20 K takes place via hopping between donor or conduction band tail states with a thermal activation energy of 3.5 meV, while at higher temperatures carriers are excited into the conduction band. Illumination with white light (energy > 1.75 eV) at low temperatures enhances different resonances depending on type and level of doping. In contrast to amorphous silicon, infrared light with energies smaller than 0.67 eV also leads to a light-induced signal enhancement. Transient light-induced ESR data are discussed in terms of a simple model, which includes both crystalline and disordered/grain boundary regions separated from each other by potential barriers.

Kurzfassung: Mittels VHF-PECVD wurde undotiertes und p- bzw. n-dotiertes mikrokristallines Silizium mit Gasphasendotierungen zwischen 1 und 160 ppm sowie hohem kristallinem Volumenanteil hergestellt. An diesem Material wurden in einem Temperaturbereich von 4.2 bis 300 K stationäre und transiente Elektronenspinresonanz(ESR)-Messungen im Dunkeln oder unter Lichteinstrahlung durchgeführt. Die Ergebnisse werden mit Transportmessungen verglichen, und es erfolgt eine Zuordnung sowie eine Bestimmung der energetischen Lage der elektronischen Zustände. Über einen weiten Dotierbereich lassen sich zwei Defektzustands-Resonanzen bei g-Werten von 2.0043 und 2.0052 beobachten, was entweder auf eine breite energetische Verteilung der Zustände (0.6 eV) oder auf Potentialfluktuationen im Material hinweist. Eine dritte Resonanz (etwa bei g = 1.998) ist Donator-, Leitungsband- oder Leitungsbandausläuferzuständen zuzuordnen, deren Besetzung stark von Temperatur und Dotierung abhängt. Insbesondere stimmt in n-dotierten Proben die Spindichte dieser Linie über zwei Größenordnungen mit der Donatorendichte überein. Hyperfeinwechselwirkung mit Phosphorkernen läßt sich nur im mittleren Dotierungsbereich beobachten. Die Lokalisierungslänge der Donatorwellenfunktion beträgt etwa 12 Å. Der Ladungstransport bei Temperaturen unter 20 K findet durch Hopping-Prozesse zwischen Donator- oder Leitungsbandausläuferzuständen mit einer thermischen Aktivierungsenergie von 3.5 meV statt, während bei höheren Temperaturen die Ladungsträger zunehmend ins Leitungsband angeregt werden. Beleuchtung mit weißem Licht (Energie > 1.75 eV) bei tiefen Temperaturen verstärkt je nach Art und Höhe der Dotierung unterschiedliche Resonanzen. Im Gegensatz zu amorphem Silizium führt auch infrarotes Licht mit Energien kleiner als 0.67 eV zu einer lichtinduzierten Signalerhöhung. Die transienten lichtinduzierten ESR-Messungen werden im Rahmen einer einfachen Modellvorstellung diskutiert, die von einer Mischung aus kristallinen und ungeordneten bzw. Korngrenzbereichen ausgeht, welche durch Potentialbarrieren voneinander getrennt sind.

Contents

List of Figures

List of Tables

Chapter 1

Introduction

It was back in the year 1839 when Alexandre-Edmond Becquerel discovered that illumination of an electrolyte cell produces an electrical voltage. (Becquerel, 1839) Long before the understanding of the physical processes involved this observation was the first hint that light can generate electricity. Some time later, 1886, the researchers Adams and Day made the same observation while illuminating the semiconducting selenium and thus gave birth to the use of semiconductors in a field nowadays called *photovoltaics*. However, the technological breakthrough did not come before the year 1954 when G. L. Pearson, D. M. Chapin and C. S. Fuller of the Bell Laboratories (USA) handed in a patent for what was the first solar cell on the basis of crystalline silicon.

Some two decades later Carlson and Wronski reported the development of the first solar cell using *amorphous* silicon (Carlson and Wronski, 1976) and opened the way for extensive research activities on silicon-based so-called *thin film* solar cells with thicknesses of the semiconducting absorber material of less than one micron, in contrast to the several hundred microns necessary for crystalline cells. In 1997 about 12 % of the total production of photovoltaic cells was based on the use of amorphous silicon (Maycock (ed.), 1998).

As amorphous silicon (a-Si:H) possesses a wide optical band gap of about 1.75 eV (Street, 1991), light with smaller energies cannot be absorbed. However, one can partly overcome this problem by combining amorphous silicon with cells made from material of lower energy gap (*stacked cell structure*) such as amorphous silicon-germanium compounds (see e. g. Ovshinski, 1985; Yang *et al.*, 1988), leading to stable efficiencies of 13 % (Yang *et al.*, 1998).

During the last few years another material gained increasing attention as absorber material for the bottom cell in stacked cell structures. It was first produced as a thin film in 1968 by Vepřek and Mareček (1968) who employed a hydrogen plasma chemical transport technique. Consisting of a phase mixture of amorphous and crystalline silicon regions, grain boundaries and internal voids it is referred to as *microcrystalline* (μc-Si) or *nanocrystalline* (nc-Si) silicon[1]. In 1979 Usui and Kikuchi (1979) prepared the first micro-

[1]The terms "nanocrystalline" and "microcrystalline" are not strictly differentiated and are most often

crystalline silicon material out of silane and hydrogen using the plasma enhanced chemical vapour deposition (PECVD) technique, and from there on much effort was dedicated to the further development of this method (see f. ex. Willeke *et al.*, 1982). A recent review which contains most of the important references was given by Willeke (1992). One of the advantages is that in PECVD microcrystalline silicon the hydrogen in the process gases terminates unsaturated bonds leading to a strong reduction of the defect density and a higher material quality. Due to the high hydrogen content one speaks of hydrogenated μc-Si or μc-Si:H.

Early structural investigations (Tsai, 1988) already exhibited a typical columnar structure which is also found in TEM measurements of the material used in the present work (Luysberg *et al.*, 1997; Houben *et al.*, 1998). They show that the material consists of areas of perfect crystallinity with an average size of 20 nm forming larger columns perpendicular to the film growth axis and extending over the entire film thickness. Between these columns one finds disordered regions or internal voids, but the individual small domains are separated from each other only by crystalline imperfections like stacking faults.

Having routinely been incorporated as highly conductive contact layers in a-Si:H solar cells, recently microcrystalline silicon was successfully used in an a-Si:H/μc-Si:H stacked cell structure (Meier *et al.*, 1996). Another example of a technologically relevant application of μc-Si:H is its use in colour sensors as shown by Stiebig *et al.* (1998).

A detailed understanding of the electrical and optical properties is essential for the improvement of device performance. One of the key questions is the mechanism of electronic transport. The conductivity of microcrystalline silicon is a decreasing function of temperature and is different from the typical behaviour of both crystalline and amorphous silicon. It cannot be characterized by a single activation energy over a wide temperature range (Stutzmann *et al.*, 1989; Dubois *et al.*, 1992; Finger *et al.*, 1993, 1994b; Hapke *et al.*, 1996). Such an activation energy appears for example in low-defect-density amorphous silicon where it corresponds to the difference between transport channel and Fermi level. The so-called *grain boundary trapping model*, developed for polycrystalline silicon (Seto, 1975; Baccarani *et al.*, 1978; Orton and Powell, 1980), has been applied to μc-Si:H assuming a distribution of barrier heights. It is, however, insufficient for a complete description of the transport process and only yields the correct temperature behaviour of the conductivity, if one additionally allows for tunneling of charge carriers through barriers (Hapke, 1995). For highly conductive n-type samples a percolation model has been successfully employed recently to interpret conductivity and Hall-effect data (Carius *et al.*, 1997b; Overhof and Otte, 1997; Carius *et al.*, 1997a) for samples with different crystalline volume fractions. However, especially in intrinsic samples or samples with low doping levels, a lot of open questions concerning the transport mechanism and the nature of the involved electronic states (defects and charge carriers) remain. In particular, one would like to know the influence of the crystalline imperfections (between the individual domains), the disordered or void-rich regions (between the columnar shaped

used as synonyms. In this work the material wil be termed "microcrystalline" throughout the text.

grains), and the rather small average sizes of the unperturbed domains (about 20 nm) on the electronic states and the transport properties of μc-Si:H.

To obtain such detailed information the use of a *microscopic* probe is necessary which can distinguish between different electronic states. Here *electron spin resonance* (ESR) is a suitable technique which was proven to be very useful in gaining microscopic information on amorphous silicon and its alloys (see e. g. Stutzmann and Biegelsen, 1988; Stutzmann, 1987; Yamasaki *et al.*, 1996). For microcrystalline silicon, however, a systematic study of the ESR behaviour upon changes of preparation conditions (like hydrogen dilution or plasma excitation frequency) or doping-induced Fermi level shifts has been missing.

It is the aim of the present work to fill in this "gap" by performing systematic ESR studies on a large number of μc-Si:H samples with controlled variations of preparation parameters. This has become possible by the combination of a modern computerized ESR spectrometer with a state-of-the-art deposition system. In particular, the use of "very high frequencies" (VHF), i. e. higher than the standard PECVD radio frequency of 13.56 MHz, allows the growth of high-quality, device-grade microcrystalline silicon material (defect density several times 10^{16} cm^{-3}) at a higher deposition rate so that a sufficient amount of material for ESR studies can be obtained within a reasonable time (see Finger *et al.*, 1997a, for a recent review).

In intrinsic microcrystalline silicon an ESR spectrum consists of two overlapping contributions from defect states, one of them being attributed to silicon dangling bonds like in a-Si:H and the other one not unambiguously identified. In n-type samples a third resonance appears which is not observed in amorphous silicon and has been attributed to conduction electrons (Hasegawa *et al.*, 1983b; Finger *et al.*, 1994b). Note that the term "conduction electron resonance" (or 'CE' in short) for this third contribution was adopted from crystalline silicon literature where it is often used both for delocalized electrons in the conduction band and for electrons in shallow localized states. One result of the present work will be to resolve this ambiguity and attribute the CE ESR signal to distinct electronic states.

In a first study ESR measurements were performed on a series of samples prepared at different plasma excitation frequencies between 13.56 and 115 MHz and different silane concentrations. Detailed results have already been published by Finger *et al.* (1998) and will therefore not be repeated here.

This work will be concerned with the study of μc-Si:H material as a function of n- and p-type doping level both in the dark and under various light illumination conditions. From these results conclusions will be drawn concerning the energy position and the location (in space) of the respective electronic states investigated. Furthermore the implications on charge carrier excitation and recombination processes will be discussed. By relating the results to conductivity measurements, information can be gained on how the electronic transport is influenced by the microscopic properties of the material. In particular, it will be shown that the conduction electron line can be identified with electrons located at donor centers or in conduction band tail states at low temperatures, whereas an increasing

number of the electrons contributing to this resonance are activated into delocalized conduction band states at elevated temperatures.

The outline is as follows: In chapter 2 details of the material preparation and structure of microcrystalline silicon as well as the consequences of this structure for the electronic states will be discussed. After that some theoretical background information will be given (chapter 3) which is necessary as a basis for the subsequent discussion. Here the focus will mainly be on the ESR technique but some theory on conduction mechanisms as well as recombination processes in μc-Si:H will also be recalled. In chapter 4 some details of ESR and conductivity measurements will be described. The following chapters 5 and 6 contain the experimental results. Here a division into measurements performed in the dark (chapter 5) and those which include light illumination of the samples was chosen. The main part of chapter 5 is concerned with ESR results, temperature dependent conductivity data will follow and finally the data will be related to each other. In chapter 6 the ESR results are further devided into time independent measurements and transient data. They will be interpreted in terms of a simple band diagram. Even though the data will usually be discussed at the point where they are presented, a concluding summary will follow in chapter 7. This includes the relation between ESR and transport data, the question of localization or delocalization of charge carriers, the defect structure as well as the locations and recombination mechanisms of photoexcited carriers. The work ends with a brief review of the questions remaining and an outlook to further experiments necessary to clarify them.

Chapter 2

Material Preparation and Structure

In this chapter first a short description of the deposition technique and the sample preparation is given, concluded by a listing of all samples used in this work and some of their material parameters. After that the material structure as obtained from transmission electron microscopy (TEM), X-ray defraction (XRD) and Raman scattering will be elaborated on. It will be explained later how the structure compares to the other experimental results (ESR and transport measurements) shown in this work.

2.1 Deposition Technique and Sample Preparation

Various different methods for the preparation of amorphous, micro- or poly-crystalline silicon are currently in use. The preparation technique for the samples presented in this work is called *plasma enhanced chemical vapour deposition* or in short PECVD. In this process hydrogen containing gases (like silane, SiH_4) are decomposed in an rf-glow discharge between planar electrodes, that serve to couple-in the rf-power of frequency ν_{ex}. A detailed description of the different possible configurations and the underlying physical principles of the process can be found e. g. in Chapman (1980).

The properties of the resulting films strongly depend on the deposition parameters such as total gas pressure, substrate temperature T_s, discharge power density p_{dis}, and plasma excitation frequency ν_{ex}. Often a considerable amount of hydrogen is added to the process gases, and the silane-to-hydrogen ratio $[SiH_4]$:$[H_2]$ in the gas mixture is another important parameter. In particular, high hydrogen dilution is essential to establish microcrystalline growth conditions. Furthermore an increase in the plasma excitation frequency not only increases the deposition rate from 0.3 Å/s to more than 1 Å/s (Hapke, 1995), but also leads to a higher crystalline volume fraction X_c and larger crystallites (see section 2.2). If higher values for ν_{ex} than the industrial standard frequency of 13.56 MHz are applied the process is referred to as very high frequency PECVD, or VHF-PECVD. The dependence of the structural and electronic properties on ν_{ex} has recently been treated in detail by Hapke (1995). It is emphasized once again that a work of the present kind has only become possible because of the favourable property of VHF deposition to

combine a high deposition rate with an improved material quality.

The material studied in this work was mostly prepared with the following parameters: total gas pressure p = 300 mTorr, p_{dis} = 35 mW/cm^2 and 50 mW/cm^2 for n- and p-type material, respectively, T_s = 200°C, ν_{ex} = 95 MHz, [SiH_4]:[H_2] = 3:97. In one sample series phosphine PH_3 was added for n-type doping with gas phase doping ratios[1] [PH_3]:[SiH_4] between 1 and 133 ppm resulting in room temperature dark conductivities σ_d^{RT} between $2.7 \cdot 10^{-4}$ S/cm and $5.1 \cdot 10^{-1}$ S/cm. In a second p-doped series doping was done by adding diborane B_2H_6 with doping ratios between 1 and 167 ppm and $4.0 \cdot 10^{-7}$ S/cm $< \sigma_d^{RT} < 4.9 \cdot 10^{-1}$ S/cm. Furthermore intrinsic samples without any intentional doping are included. They were taken from the sample series where the plasma excitation frequency was varied as mentioned in chapter 1 and described by Finger *et al.* (1998).

For ESR measurements the use of powdered samples allows to place a large amount of material in the center of the resonant cavity resulting in high signal intensity and an improved signal-to-noise ratio. Therefore samples were deposited both on aluminum foil and on roughened borosilicate glass[2] in the same run to have material for both ESR and conductivity measurements. The aluminum foil was etched away by HCl after deposition, leaving only the microcrystalline material as a suspension of small flakes in the solution. After that, the flakes were filtered out of the fluid solution and thoroughly rinsed with de-ionized water. Finally they were dried overnight at air. This procedure yielded between 18 and 60 mg of material for ESR measurements. If consisting of very loosely packed flakes, the material was additionally crushed to obtain comparable packing densities and filling heights. The resulting powder was finally sealed in quartz tubes (filling height 0.5–1 cm) under He atmosphere to maintain a defined environment after the sealing. The use of roughened substrates for conductivity measurements was necessary as films with thicknesses larger than 1 μm tend to peel off from flat substrates.

Throughout the text the notation of the samples will be as follows: For the n- and p-type samples each sample is denoted by its type of doping, i. e. n or p, followed by a number equal to the gas phase doping ratio of the sample in ppm. Thus for example 'p67' refers to a sample of the p-series with 67 ppm doping. For the intrinsic samples the notation 'i' is used followed by the value of the plasma excitation frequency, since they are taken from a series where ν_{ex} was varied (see Finger *et al.*, 1998). Sample i95 is therefore an undoped sample prepared at 95 MHz. Table 2.1 gives an overview of all samples. Included are the respective doping ratios, deposition rates r, film thicknesses d, masses of the ESR powder samples m as well as their room temperature dark conductivities σ_d^{RT}. The dependence of

[1] 'Gas phase doping ratio' means the ratio of the respective gas flows under standard conditions, measured in sccm.

[2] Sample n1 and the intrinsic samples were prepared on roughened quartz subtrates. However, exposition of quartz glass to a reactive plasma leads to the creation of so-called 'E'-centers' at g = 2.0008 (see e. g. Griscom *et al.*, 1974), which are strongly visible in the ESR spectra. Therefore later-on the use of borosilicate glass was preferred which leads to almost no additional and disturbing signal.

sample	doping (ppm)	r(Å/s)	d(μm)	m(mg)	σ_d^{RT}(S/cm)	remark
p1	1	1.21	3.0	52	$4.0 \cdot 10^{-7}$	—
p3	3	1.15	3.4	59	$3.1 \cdot 10^{-5}$	—
p7	7	1.16	3.2	55	$1.8 \cdot 10^{-4}$	—
p23	23	1.12	3.5	54	$3.9 \cdot 10^{-3}$	—
p57	57	1.41	3.8	44	$3.4 \cdot 10^{-2}$	—
p133	133	1.24	2.7	48	$4.6 \cdot 10^{-1}$	—
p162	162	1.13	3.3	54	$4.9 \cdot 10^{-1}$	—
n1	1	0.84	2.6	57	$2.7 \cdot 10^{-4}$	115 MHz, 150 mTorr
n2	2	1.0	3.0	51	$7.2 \cdot 10^{-4}$	—
n3a	3	1.0	2.1	39	$1.1 \cdot 10^{-3}$	—
n3b	3	0.71	1.7	30	$5.0 \cdot 10^{-3}$	—
n17	17	1.18	3.1	57	$1.1 \cdot 10^{-2}$	—
n33	33	0.61	1.7	29	$9.8 \cdot 10^{-2}$	—
n67	67	0.76	2.2	36	$1.8 \cdot 10^{-1}$	—
n133	133	0.87	1.1	18	$5.1 \cdot 10^{-1}$	—
i13	–	0.36	2.2	42	$3.4 \cdot 10^{-5}$	13.56 MHz, 500 mTorr
i50	–	0.6	3.8	65	$8.5 \cdot 10^{-6}$	49.7 MHz, 300 mTorr
i95	–	0.9	6.6*	55	$3.0 \cdot 10^{-6}$	94.7 MHz, 300 mTorr
i115	–	1.1	2.3	31	$4.2 \cdot 10^{-6}$	115 MHz, 150 mTorr

Table 2.1: Doping ratio, deposition rate r, film thickness d, mass m of powder samples and room temperature dark conductivity σ_d^{RT} of all samples. The last column mentions deviations from the standard preparation conditions described in the text.
* Not the whole film was used for ESR measurements.

the σ_d^{RT} on the gas phase doping ratio is illustrated in Fig. 2.1. It is seen that for both types of doping the conductivity nicely increases with increasing doping level. Sample p1 with a p-type doping level of 1 ppm exhibits a conductivity even smaller than the <i>-samples. This makes sense as nominally undoped samples are generally slightly n-type and adding small amounts of boron as p-type dopant will lead to compensation effects. Note that compensation by boron doping has also been observed in early measurements on microcrystalline silicon (Willeke, 1983; Spear *et al.*, 1983), even though in these works higher boron concentrations were necessary.

2.2 Material Structure

The structure of the microcrystalline material is strongly influenced by the deposition parameters used. There have been a number of studies treating the dependence of structural, electronic and optical properties of μc-Si:H on hydrogen dilution and plasma excitation frequency ν_{ex} (Finger *et al.*, 1994a; Hapke, 1995; Houben, 1995; Luysberg *et al.*, 1997;

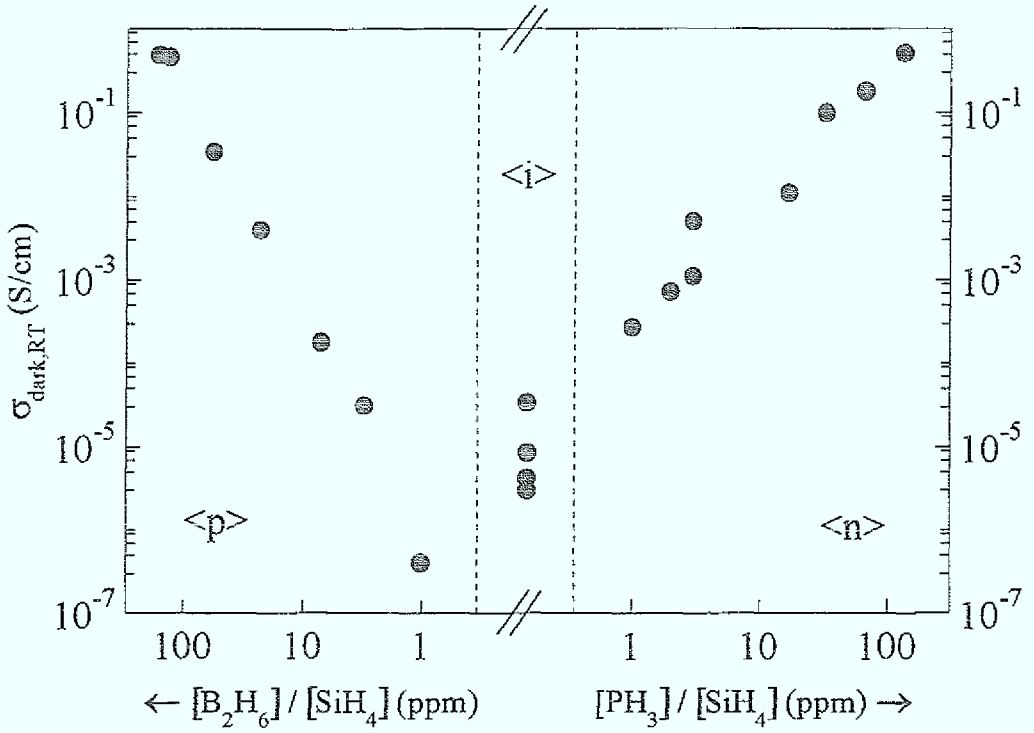

Figure 2.1: Dependence of σ_d^{RT} on gas phase doping ratio for p-type (left), undoped (center) and n-type (right) samples. Undoped samples were prepared at different plasma excitation frequencies (see Tab. 2.1).

Finger *et al.*, 1997a; Backhausen, 1996; Backhausen *et al.*, 1997; Houben *et al.*, 1998). The cited studies were performed on material prepared in the same deposition system as was used in the present work. They contain many references to the work of other groups which will therefore not be cited again here. Very good summaries of the material properties of VHF-PECVD grown μc-Si:H were recently given by Finger *et al.* (1997b), Carius *et al.* (1997b) and Luysberg *et al.* (1997). In particular it was found that both the average grain size δ and the crystalline volume fraction X_c increase with increasing plasma excitation frequency.

Furthermore the complex mixed phase structure of microcrystalline silicon is likely to have an important influence and might impose some constraints on electronic states in the material, some aspects of which will be outlined below. A discussion of this topic was also given by Finger *et al.* (1998). Most useful information on the structure of μc-Si:H was obtained from a combination of transmission electron microscopy (TEM), Raman scattering and X-ray diffraction (XRD) experiments (Luysberg *et al.*, 1997; Houben *et al.*, 1998). Raman spectroscopy provides a qualitative measure of the crystalline volume fraction by comparing the intensities of the crystalline and amorphous contributions in the Raman

spectra (Hapke, 1995). Although Raman results tend to underestimate the crystalline volume fraction they can be 'calibrated' by TEM measurements which yield crystalline volume fractions of more than 90% for all of the samples studied in this work. XRD, which probes the size of coherent regions, yields average sizes of 20 nm for domains with perfect, unperturbed long-range order. Fig. 2.2 shows dark-field (a) and high-resolution (b) images of microcrystalline silicon grown on a crystalline silicon(100)-substrate with native oxide. Recalling that in dark-field images crystalline regions appear with bright contrast Fig. 2.2(a) clearly shows columnar shaped crystalline grains perpendicular to the substrate with typical lateral dimensions of 50 nm and vertical sizes extending over the entire film thickness. These columns, which comprise 90% of the sample volume, are separated from each other by disordered regions or regions of low density (voids). Also very narrow grain boundaries between adjacent crystalline columns are possible. An example is nicely seen in the high resolution (HR) TEM image of Fig. 2.2(b) indicated by the black arrow. Fig. 2.2(b) exhibits the same columnar structure as the dark field image in (a) but with smaller lateral dimensions reflecting the nucleation zone close to the substrate interface. The crystalline regions in Fig. 2.2(b) appear as the traces of the (111)-lattice planes.

A column can be regarded as a crystalline grain which is only perturbed by the typical crystalline imperfections like stacking faults, twinning (seen as the zig-zag contrast in Fig. 2.2(b)) or gradual tilting of the crystal planes. These imperfections lead to the observed subdomain structure of the columnar grains. To avoid confusion, in the following the columns will be referred to as 'grains' whereas the regions with perfect long-range order making up the columns are called 'domains'. Since the interfaces between these domains are known to preserve the local tetrahedral coordination, they are not expected to lead to paramagnetically active deep defect states. On the other hand the disordered regions separating columnar grains are likely to have a much higher density of point defects (dangling bonds).

The problem now is to know the influence of these crystalline imperfections (between the individual domains), the disordered or void-rich regions (between the columnar shaped grains), the possible potential barriers and the small average sizes of the unperturbed crystalline domains (20 nm) on the electronic states in the material.

For the 20 nm size areas we can assume a crystalline silicon band structure with less than one defect per every ten domains, calculated from a typical dangling bond spin density of $2.5 \cdot 10^{16}$ cm^{-3} (see section 5.1) and averaging over the entire sample volume (Finger *et al.*, 1998). This should strongly affect the energies of adjacent 20 nm domains with or without defect. Similarly, for the charge carriers (or dopant atoms), taking a typical spin density of the conduction electron (in short: CE) resonance of $N_s = 2.5 \cdot 10^{17}$ cm^{-3} of a very lightly n-doped μc-Si:H-sample and assuming the electrons contributing to the CE resonance to be within the crystalline regions this would mean only one electron per domain. So, in any case, the defect and charge distribution will be extremely inhomogeneous on a 20 nm scale, the extension of perfect, unperturbed long-range order.

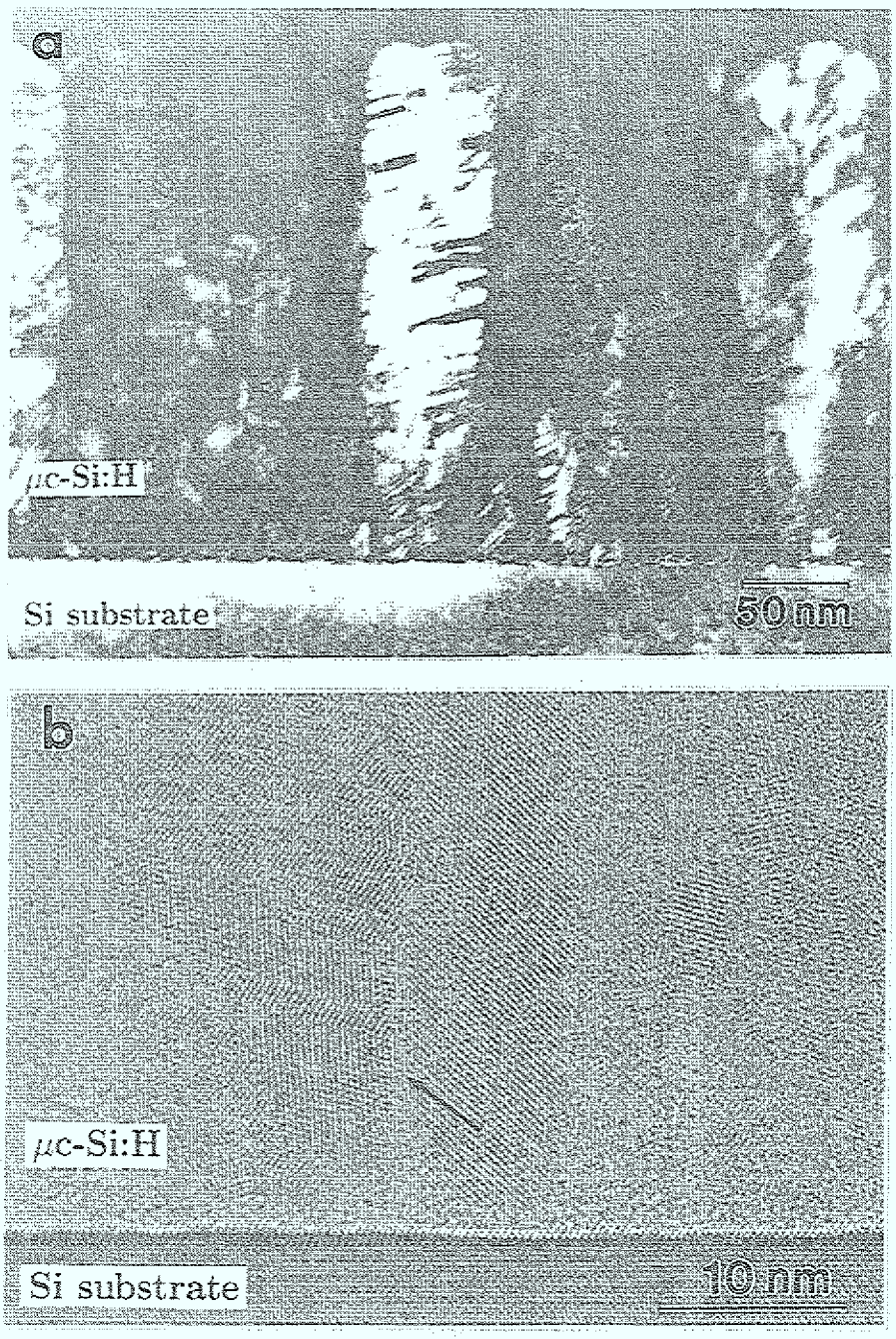

Figure 2.2: Dark-field (a) and high-resolution (b) TEM images of microcrystalline silicon grown on a crystalline silicon(100)-substrate with native oxide. The dark field image shows a typical columnar structure of extended crystalline regions (bright contrast). In the HR-TEM picture (note the smaller length scale) crystalline regions are seen as the traces of the (111)-lattice planes. The arrow indicates the case of a narrow boundary between adjacent crystalline columns. The grains themselves consist of perfect crystalline domains and only contain crystalline imperfections like stacking faults or twinning (seen as zig-zag contrast). The pictures are taken from Houben *et al.* (1998).

While not containing many point defects, structural disorder may lead to the formation of localized band tail states within the grains. In a-Si:H such states extend from the band edges into the gap over an energy range of 200 meV (conduction band tail) or 300–400 meV (valence band tail) (Stutzmann *et al.*, 1987). In polycrystalline silicon various experimental studies indicate the existence of band tail states at grain boundaries in silicon or germanium (see e. g. Werner and Peisl, 1985b,a; Jousse *et al.*, 1991). They originate generally from local distortions in bond length, bond angles and dihedral angles. Such disorder at grain boundaries leads to small wavelength potential fluctuations on a length scale of the lattice constant resulting in a localization of free carriers (Werner, 1989). Recently Kohyama and Yamamoto (1994) performed detailed theoretical calculations on the effects of structural disorder at grain boundaries in silicon on the electronic structure. They found that bond stretchings of several percent and bond angle distortions of about $20° - 30°$ are necessary to generate states inside the energy gap.

In high resolution TEM studies on microcrystalline silicon the grain boundaries are highly reconstructed and the bond angle and bond length distortions found so far are not sufficient to lead to substantial band tailing (Houben, 1998). However, it is noted that for example so-called *twist* boundaries which can indeed generate localized tail states, can generally not be detected by TEM in a material like microcrystalline silicon. Therefore, given the various experimental proofs of band tailing in polycrystalline silicon and the large number of crystalline imperfections and grain-column boundaries in μc-Si:H, the existence of band tails can also be assumed here even for samples with the observed high crystalline volume fractions.

Chapter 3

Theoretical Background

3.1 Electron Spin Resonance

When speaking of *electron spin resonance* (ESR)[1] one has to distinguish between so-called *continuous wave*-(CW) techniques and *pulsed* ESR. The former is the conventional method which employs permanent electromagnetic microwave radiation and was mainly developed in the 1950's being a rapidly growing field as the experimental equipment became available. It is nowadays established as an every-day technique in chemical analysis and is also widely used in different fields of solid state physics.

Pulsed or *time-domain* ESR on the other hand works with very short (typically nanoseconds) microwave pulses of high power and records the response of the system on a time scale. As especially for the case of pulsed ESR the technical requirements are very high, this technique was developed somewhat later as its CW counterpart and is less common, although pulsed ESR spectrometers are meanwhile available commercially.

In this section, first the physical fundamentals of the ESR technique will be presented, followed by a description of the various quantities one encounters in ESR, the information which can be gained from them and their influence on each other. Some details of the experimental procedures, including light induced and transient ESR, and the handling of ESR data will be given in chapter 4.

Whenever possible it will be attempted to use SI units throughout the whole text. However, as frequently in ESR literature no real distinction is made between magnetic field strength $\vec{H}$ and magnetic induction $\vec{B}$ and the different systems of units (SI and cgs) are sometimes intermixed, one or the other inconsistency cannot be excluded.

[1]The term *electron paramagnetic resonance* (EPR) is also frequently encountered and is mostly used as a synonym.

3.1.1 Fundamentals

The physical principle of ESR is best explained in terms of the free electron. An electron possesses a magnetic moment $\vec{\mu}$ due to its spin $\vec{S}$ (in units of $\hbar$):

$$\vec{\mu} = -g\mu_B\vec{S} = -\gamma\hbar\vec{S} \tag{3.1}$$

$$\text{where} \qquad \mu_B = \frac{e\hbar}{2m_e} \quad and \quad \gamma = \frac{g\mu_B}{\hbar}$$

In Eq. 3.1 g is the electronic g-value, μ_B the Bohr magneton, $\hbar = h/2\pi$ with the Planck constant h, e is the elementary charge and m_e the electron mass. The quantity γ is called *gyromagnetic ratio*. In the absence of an external magnetic field the two possible spin states with spin quantum numbers $m_s = +1/2$ and $m_s = -1/2$ will have the same energy and be equally populated. If an external magnetic field $\vec{B}_0 = B_0 \cdot \vec{e}_z$ is applied, the degeneracy of the spin states is lifted (the so-called *Zeeman splitting* see Fig. 3.1) and the energy difference between the two states becomes $\Delta E = g\mu_B B_0$.

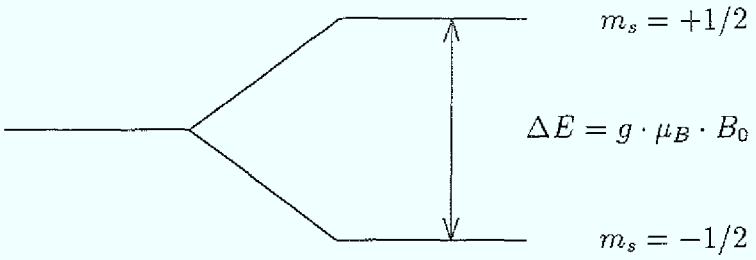

Figure 3.1: Zeeman splitting of the free electron spin levels in an external magnetic field.

In thermal equilibrium for a system of non-interacting spins the population of the higher energy level will be smaller by the Boltzmann factor $\exp(-\Delta E/k_B T)$ where k_B is the Boltzmann constant. Thus the system can resonantly absorb electromagnetic radiation from an external source of frequency ν if the basic resonance condition of ESR is fulfilled:

$$h\nu = \Delta E = g\mu_B B_0 \tag{3.2}$$

However, in an isolated system of spins, as the one shown in Fig. 3.1, the populations of the two energy levels would soon be equal to each other as in equilibrium the rates of stimulated emission and absorption of microwave radiation are the same. Hence a reservoir is needed with which the spin system can interact and to which it can transfer energy, thus maintaining a population difference even under resonance conditions. In a solid the reservoir is the surrounding lattice, and hence the process of transfering energy from the spin system to its surroundings is called *spin-lattice relaxation*. This will be explained in more detail below.

For a discussion of a macroscopic system like a solid it is more convenient to introduce the *magnetization* $\vec{M} = \sum_i \vec{\mu}_i$ as the sum of the individual magnetic moments $\vec{\mu}_i$. If an external magnetic field $\vec{B}_0 = B_0 \cdot \vec{e}_z$ is applied to such a system, each individual spin will start to precess around the direction of $\vec{B}_0$ with the Larmor frequency $\omega_0 = \gamma B_0$. The magnetization will align along the z-direction with a characteristic time T_1, the *longitudinal* or *spin-lattice relaxation time*. Similarly the net magnetization along $\vec{B}_0$ will decay with the time constant T_1 when the external field is switched off. The x-y-components of the individual magnetic moments rotating in the x-y plane perpendicular to the external field have no phase coherence and thus their thermal equilibrium values are zero.

However, a suitable external perturbation can impose such a phase coherence and one obtains a net component of the magnetization perpendicular to $\vec{B}_0$ rotating in the x-y-plane. In a magnetic resonance experiment the perturbation usually is an incident electromagnetic microwave $B_1(t)$ at right angles to the z-direction. As soon as the microwave radiation is turned off, the magnetization in the x-y-plane again approaches zero as the phase coherence is lost with a second time constant called the *transverse relaxation time* T_2. It is frequently also referred to as *spin-spin relaxation time* as the loss of phase coherence mainly reflects variations in the precession rates of the individual spins caused by their local interactions (Atherton, 1993). Strictly speaking one has to distinguish between the longitudinal and transverse relaxation on the one hand and spin-lattice and spin-spin relaxation on the other hand (Malten, 1996, pp. 17f). But as the involved relaxation processes and mechanisms will not be treated in great detail in this work, the corresponding terms will be used as synonyms.

A general description of the relaxation behaviour of a macroscopic spin system is given by the so-called *Bloch equations* (Bloch, 1946, see also section 3.1.3.1). Most of the textbooks on magnetic resonance treat this subject in great detail and it is therefore omitted here. For a very good introduction see for example Poole and Farach (1971), pp. 6ff.

An important difference between longitudinal and transverse relaxation is that the latter does not change the energy of the system[2]. Therefore the transverse components can change without the necessity to transfer energy to a reservoir (i.e. the lattice) and in many cases the transverse relaxation is the faster process ($T_2 < T_1$).

3.1.2 Spin Hamiltonian

Having discussed the fundamental principles of ESR, a description of the spin properties of a given electronic spin $\vec{S}$ in a solid is now necessary. This is usually done in terms of the so-called *spin Hamiltonian* $\mathcal{H}$ (Poole, Jr., 1982; Pake and Estle, 1973; Slichter, 1990)

$$\mathcal{H} = g_0 \mu_B \vec{B}_0 \vec{S} + \mu_B \vec{B}_0 [\Delta g] \vec{S} + \sum_i \vec{I}_i [\mathrm{A}_i] \vec{S} + \sum_j \vec{S}_j [\mathrm{D}_j] \vec{S} \tag{3.3}$$

wherein g_0 is the free electron g-value (≈ 2.0023), $\vec{I}_i$ the nuclear spin of the i*th* nucleus, $\vec{S}_j$ the electronic spin of the j*th* paramagnetic center in the system and the tensor quantities

[2]Recall that the energy E of a magnetic moment $\vec{\mu}$ in a field $\vec{B}_0$ is given by the scalar product $\vec{\mu} \cdot \vec{B}_0$, and hence $E = 0$ for $\vec{\mu} \perp \vec{B}_0$.

$[\Delta g]$, $[A_i]$ and $[D_j]$ are the interaction tensors of the spin-orbit coupling (often called the *g-tensor*), the hyperfine interaction and the spin-spin coupling, respectively. Terms that only contain the nuclear spins $\vec{I}_i$ have been left out.

3.1.2.1 Terms not involving $\vec{I}$

Concerning the form of the first and second term in Eq. 3.3 some remarks are necessary. Both could also be written as

$$\lambda \vec{L} \cdot \vec{S} + \mu_B \vec{B}_0 (\vec{L} + g_0 \vec{S})$$

wherein $\lambda \vec{L} \cdot \vec{S}$ describes the spin-orbit coupling between the magnetic moments arising from the electronic spin and the orbital motion of the electron in a bound state (λ denotes the spin-orbit coupling constant) and $\mu_B \vec{B}_0 (\vec{L} + g_0 \vec{S})$ is the Zeeman interaction.

Now, in a covalent semiconductor, where the electronic eigenstates are usually described in terms of s- or p-like wavefunctions, the orbital angular momentum $\vec{L}$ (whose eigenstates are degenerate) has a *zero* expectation value, if the crystal field interactions greatly exceed the Zeeman term (Poole, Jr. and Farach, 1987; Stutzmann and Biegelsen, 1988). This is known as the *quenching* of orbital momentum by the crystal field and would only leave the term $g_0 \mu_B \vec{B}_0 \vec{S}$ which in fact appears in Eq. 3.3. It is the Zeeman energy of a free electron in a magnetic field B_0 (see Fig 3.1) and makes up the largest contribution to $\mathcal{H}$. However, the interaction with the external magnetic field B_0 lifts the degeneracy of the eigenstates of $\vec{L}$ and thus partially removes the quenching. The result is a second order term which can be written as $\mu_B \vec{B}_0 [\Delta g] \vec{S}$ with the g-tensor $[\Delta g]$. The g-tensor with components g_{ij} of an unpaired spin in the molecular orbital ψ_d is given as (Ishii *et al.*, 1981)

$$g_{ij} = g_0 \delta_{ij} + 2\lambda \sum_{s(\neq d)} \frac{\sum_A \langle \psi_d | L_i^A | \psi_s \rangle \langle \psi_s^{(A)} | L_j^A | \psi_d^{(A)} \rangle}{E_d - E_s} \tag{3.4}$$

where the index s covers all other occupied or unoccupied orbitals ψ_s, A denotes all atoms within the molecular orbital ψ_d, L_i^A is the i-th component of the angular momentum operator centered on atom A and $\psi_s^{(A)}$ and $\psi_d^{(A)}$ represent the projections of the molecular orbitals ψ_s and ψ_d onto the atomic orbitals centered on atom A, respectively. E_d and E_s are the energies of the states ψ_d and ψ_s.

The g-tensor serves to distinguish and identify different electronic states and thus is an important quantity in ESR measurements. However, microscopic information about the underlying electronic wave functions is usually very hard to extract. Additionally in an amorphous or microcrystalline semiconductor its angular dependence is masked under a so-called *powder spectrum* (see also section 3.1.4). Therefore in this work the g-tensor is mainly observed as an "average" g-value characteristic for an individual resonance line without deducing any detailed information about the wave functions of the corresponding states.

The spin-spin interaction term $\sum_j \vec{S}_j[\mathrm{D}_j]\vec{S}$ describes the interaction between the spin $\vec{S}$ and all the other paramagnetic states in the system. As the interactions are of short range (Stutzmann and Biegelsen, 1988) one can again only consider the nearest neighbours. Furthermore, in dilute spin systems with spin densities well below 10^{19} cm^{-3} it can be neglected. However, if the spins locally come very close together (as e. g. in the case of unpaired spins at phosphorus donors in silicon, which are known to form clusters of two or more atoms (see Feher *et al.*, 1955, and section 3.1.2.2), the spin-spin interaction will become important.

3.1.2.2 Hyperfine Interaction

The hyperfine (hf) interaction term contains the interactions of the given electronic spin with all of the surrounding nuclei of the lattice. For practical purposes it is usually sufficient to restrict oneself to the nucleus ($\vec{I}$) closest to the electronic spin, e. g. the dopant nucleus for an unpaired electron located at its donor site, leaving only the term $\vec{I}[\mathrm{A}]\vec{S}$ left of the summation in Eq. 3.3. It can be divided into two contributions (Slichter, 1990; Stutzmann and Biegelsen, 1988): an *isotropic* part for states with non-zero probability at the nucleus, i. e. s- and s-like states, due to the Fermi contact interaction (Fermi, 1930) and an *anisotropic* part arising from dipole–dipole interaction between $\vec{I}$ and $\vec{S}$ for wavefunctions that vanish at $r = 0$, i. e. for $\psi(r=0) = \psi(0) \equiv 0$, $\psi(0)$ being the electronic wavefunction at the site of the nucleus. In a cubic lattice with four-fold coordination like crystalline silicon or the crystallites in μc-Si:H the anisotropic hyperfine interaction averages out to zero for symmetry reasons and therefore needs not be considered here.

For a further discussion we will follow a treatment given by Stutzmann (1987). It is assumed that the electronic wave functions we are interested in can be regarded as spherically symmetric s-like functions, a form which also serves as a first approximation for the envelope of the donor ground states in crystalline silicon. The residual isotropic interaction $[\mathrm{A}_{iso}]$, which is of the Fermi contact form, is given by (Atherton, 1993)

$$[A_{iso}] = A_{iso} \cdot [\delta_{ij}] = \frac{2\mu_0}{3} g \mu_B g_n \mu_n |\psi(0)|^2 \cdot [\delta_{ij}] \tag{3.5}$$

$$\text{with} \quad \mu_n = \frac{e\hbar}{2m_p}$$

In Eq. 3.5 g_n and μ_n are the nuclear g-value and the nuclear magneton, respectively, m_p is the proton mass, μ_0 the magnetic permeability of the vacuum and $[\delta_{ij}]$ denotes the unity tensor. The electronic g-value is now isotropic and appears as a scalar quantity.

With this result and neglecting the last term in Eq. 3.3 the spin Hamiltonian can now be re-written as

$$\mathcal{H} = g\mu_B \vec{B}_0 \vec{S} + A_{iso} \vec{I}\vec{S} \tag{3.6}$$

Using again $\vec{B}_0 = B_0 \cdot \vec{e}_z$ and introducing the operators $S_\pm = S_x \pm iS_y$ (similar for $I_\pm$)

for the cartesian components of $\vec{S}$ and $\vec{I}$ this yields

$$\mathcal{H} = g\mu_B B_0 S_z + A_{iso} I_z S_z + \frac{1}{2} A_{iso}(I_+ S_- + I_- S_+) \tag{3.7}$$

The corresponding energy levels are obtained as the eigenvalues of $\mathcal{H}$ and depend on the electronic and nuclear magnetic quantum numbers m_S and m_I. Calculating the ESR transition energies ΔE for an electronic spin with $S = 1/2$ by subtracting the energy levels corresponding to spin quantum numbers $m_S = +1/2$ and $m_S = -1/2$ finally yields

$$\Delta E(m_I) = g\mu_B B_0 + A_{iso} m_I + \frac{A_{iso}^2}{2g\mu_B B_0}[I(I+1) - m_I^2] \tag{3.8}$$

This equation states that as a result of the hyperfine splitting a single resonance occuring at an energy $g\mu_B B_0$ is split into $2I + 1$ lines occuring at energies given by Eq. 3.8.

To translate Eq. 3.8 to a magnetic field scale one uses the ESR resonance condition $h\nu = g\mu_B B_0$ and expresses A_{iso} in terms of the magnetic field splitting ΔHFS ($A_{iso} = g\mu_B \Delta HFS$). The result gives the magnetic field positions $B(m_I)$ at which the hf-lines occur:

$$B(m_I) = B_0 - m_I \Delta HFS - \frac{(\Delta HFS)^2}{2B_0}[(I(I+1) - m_I^2] \tag{3.9}$$

For hyperfine splittings $\Delta HFS < 100$ G (like for phosphorus in c-Si, see below) the first two terms are usually sufficient and in this case the two hf-lines would be symmetric with respect to the position of B_0.

At this point it is useful to examine the case of an n-type phosphorus-doped semiconductor in somewhat more detail, as this information will be needed later on. The spins located at their donor atoms of such a semiconductor will interact with the magnetic moment of the phosphorus nucleus (^{31}P, 100% natural abundance, nuclear spin I = 1/2) via the isotropic hf-interaction [A_{iso}] giving rise to a hyperfine splitting into two states with different energies. In crystalline silicon at low temperatures (T < 30 K) and low dopant concentrations ($N_D < 8 \cdot 10^{16}$ cm^{-3}) the majority of the electrons will be in the ground state of the donor atom (Lépine, 1970). The six-fold degenerate ground state of phosphorus splits into a singlet state A_1, a doublet state E and a triplet state T_2, the latter 5 states lying very close to each other and being separated from the singlet ground state A_1 by about 11 meV (Kohn, 1957; Lépine, 1970). Only the wave function of the A_1 state has a non-vanishing amplitude at the nucleus and therefore will give rise to the ESR observation of two lines (Lépine, 1970; Fletcher *et al.*, 1954b).

For higher temperatures, however, an increasing part of the electrons will be activated into excited states or even conduction band states with no hyperfine interaction. The hyperfine lines broaden as a result of exchange scattering between the donor electrons and the conduction band electrons. With increasing donor concentration the donors form clusters of two or more donor atoms leading to additional features in the resonance spectrum and

also the gradual disappearance of the hf line pair due to an electron located at a single impurity atom (Slichter, 1955; Feher and Kip, 1955; Maekawa and Kinoshita, 1965; Morigaki and Maekawa, 1972; Cullis and Marko, 1975). For even higher concentrations an increasing number of electrons occupy delocalized states in the conduction band or in an impurity band (Mooser, 1955; Stesmans and De Vos, 1986). The various possible ESR spectra in the different temperature regimes between 4.2 and 40 K in a sample of intermediate impurity concentration is illustrated for example in a recent work by Morooka *et al.* (1994).

With this knowledge it will be instructive to investigate possible hyperfine interaction of electrons with phosphorus doping atoms in μc-Si:H and compare the results with those known for single crystalline silicon. In particular, the localization of the dopant state electrons, which determines the strength of the hf interaction, and the energy position of the phosphorus states in the grains of μc-Si:H are of interest.

3.1.3 Magnetic Susceptibility

3.1.3.1 General

After the theoretical description of ESR in the preceding section by introducing the spin Hamiltonian $\mathcal{H}$, it has to be shown which quantities are accessible during an ESR experiment and how the desired microscopic information can be deduced from the measurements.

As already mentioned, a simple and intuitive way to investigate the dynamic behaviour of a spin system during a CW resonance experiment is by means of the *Bloch equations* (Bloch, 1946), a set of three differential equations describing the time dependence of the components of $\vec{M}$ along the three space coordinates in terms of T_1 and T_2. The complex magnetic susceptibility $\chi(\omega)$ is given by

$$\chi(\omega) = \chi'(\omega) - i\chi''(\omega) \tag{3.10}$$

where the real part $\chi'(\omega)$ produces a frequency change in the resonant cavity and the imaginary part $\chi''(\omega)$ leads to energy absorption (Poole and Farach, 1971; Ludwig and Woodbury, 1962). In this work ESR experiments were always done in the absorption mode of the spectrometer. Then, using the Bloch equations, one obtains for $\chi''(\omega)$ (see e. g. Atherton, 1993, p. 289)

$$\chi''(\omega) = \frac{1}{2}\chi_0\omega_0 \frac{1}{1 + (\omega - \omega_0)^2 {T_2}^2 + \gamma^2 {B_1}^2 T_1 T_2} \tag{3.11}$$

$$\text{with} \quad \chi_0 = \mu_0 \frac{M_0}{B_0}$$

wherein χ_0 denotes the static magnetic susceptibility in thermal equilibrium under the action of B_0. The last term in the denominator $\gamma^2 {B_1}^2 T_1 T_2$ is often called *saturation parameter* as it decreases the magnitude of the observed susceptibility. The physical reason for the phenomenon of saturation is that for large values of the magnetic field B_1, i. e. for high microwave power, or long spin-lattice relaxation time T_1 the populations of

the two Zeeman-split energy levels of the spin system will become more and more equal. In the limit of complete saturation there will be no population difference anymore, thus there is no net absorption of energy from the microwave field and no ESR signal can be detected. By varying the incident microwave power (B_1) and monitoring the decrease in signal intensity in an ESR experiment one can estimate the product T_1T_2. In dilute spin systems, where interaction between the individual spins is weak, T_2 is expected to be long but is limited by T_1. In that case $T_1 \approx \frac{1}{2}T_2$ (Stutzmann, 1983) and the spin-lattice relaxation time T_1 can be estimated, if the value of B_1, i. e. the magnetic field at the site of the sample, is known.

For a system of ideal non-interacting paramagnets with spin angular momentum S and spin density N_s the temperature dependent value of χ_0 in Eq. 3.11 is given by (Atherton, 1993)

$$\chi_0 = \frac{N_s \mu_0 {\mu_B}^2 g^2 S(S+1)}{3k_B T}. \tag{3.12}$$

In the absence of saturation ($\gamma^2 {B_1}^2 T_1 T_2 \ll 1$) the ESR signal intensity (determined as the area under an absorption curve) is proportional to $\int_0^\infty \chi''(\omega)d\omega$ (Slichter, 1990, p. 58). Hence, according to Eqs. 3.11 and 3.12, the ESR intensity is also proportional to χ_0 and to the spin density N_s, but inversely proportional to the temperature [3]. The latter relation is known as the *Curie law* for ideal paramagnets and is a result of the decreasing population difference between the respective spin levels with rising temperature. The former relation (Eq. 3.11) makes it possible to determine the spin density of a paramagnetic species by measuring its ESR signal.

In our idealized homogeneous system it is seen from Eq. 3.11 that the lineshape is a Lorentzian with linewidth $\Delta\omega_{1/2}$:

$$\Delta\omega_{1/2} = \frac{2}{T_2} \quad \text{or} \quad \Delta H_{1/2} = \frac{2}{\gamma T_2}. \tag{3.13}$$

The latter form, which gives the linewidth in magnetic field units, applies, if the frequency is kept constant and magnetic field scanning is employed as is usually done in an ESR experiment (section 4.1). In a real system, however, the observed ESR lines can often not be described by Eq. 3.11 as various mechanisms are present that alter the lineshape and broaden the resonance lines. This will be explained in more detail in section 3.1.4.

3.1.3.2 Susceptibility in Semiconductors

In semiconductors the temperature and doping dependence of the paramagnetic susceptibility can provide valuable information about the electronic spins responsible for a particular resonance line. This will be shown in the following by recalling briefly the basic relations for the magnetization in semiconductors.

[3] Keeping this proportionality in mind, in the following it will not be strictly distinguished between ESR signal (or signal intensity) and susceptibility but both terms will often be used as synonyms.

There are two simple cases of electronic paramagnetism referred to as *Curie-like* or *Pauli-like* behaviour. The static paramagnetic susceptibility of a system of ideal non-interacting paramagnetic centers, whose statistics are governed by the Maxwell-Boltzmann-distribution and whose total number N_s is constant in the temperature range under question, shows the typical 1/T- or Curie-like behaviour according to Eq. 3.12. For the case of electrons with spin $S = 1/2$ and $g \approx 2$ Eq. 3.12 simplifies to

$$\chi^{Curie} = \frac{N_s \mu_0 {\mu_B}^2}{k_B T} \tag{3.14}$$

According to Mooser (1955) the expression for the paramagnetic susceptibility of electrons located at their donor sites in an n-doped semiconductor is also given by Eq. 3.14, if $N_s = N_s(T)$ is the temperature dependent concentration of these electrons. Even if electrons are excited into the conduction (or an impurity-) band they are expected to behave Curie-like, as long as their concentration remains low and the temperature high enough for the electron gas to be non-degenerate.

On the other hand, a gas of non-interacting degenerate electrons will follow the Fermi-Dirac distribution. The resulting paramagnetic susceptibility was calculated by Pauli (1927) and is given as (see. e. g. Morrish, 1965)

$$\chi^{Pauli} = \frac{N_s \mu_0 {\mu_B}^2 g^2 S(S+1)}{3 k_B T} \cdot \frac{F'_{1/2}(E_F)}{F_{1/2}(E_F)} \tag{3.15}$$

where $F_{1/2}(E_F)$ and $F'_{1/2}(E_F)$ denote the Fermi function and its derivative, respectively, and E_F is the Fermi energy. For the case of sufficiently low temperatures such that the condition $k_B T \ll E_F$ is fulfilled, the susceptibility becomes temperature independent and has the value

$$\chi^{Pauli} = \frac{N_s \mu_0 {\mu_B}^2}{E_F} \tag{3.16}$$

Measurements of the temperature dependence of the susceptibility should therefore enable one to distinguish between the degenerate and the non-degenerate case. However, a distinction between localized and delocalized electrons is not possible from the temperature dependence of χ alone. In addition, the changing occupation of the corresponding states with temperature ($N_s = f(T)$), which should follow semiconductor statistics, will have to be taken into account.

3.1.4 Lineshape and Linewidth

The lineshapes and linewidths of an ESR spectrum contain a large amount of information about the spin system studied. Although this information is not easily accessible and often masked in a disordered system like μc-Si:H, the analysis of lineshape and linewidth is an important tool. Note that in ESR one mostly encounters the so-called peak-to-peak linewidth (ΔH_{pp}) which is defined as the distance between points of maximum slope of the absorption lines. In the first derivative this appears simply as the distance between

maximum and minimum of the curve, which explains its wide-spread use in ESR practice. The peak-to-peak linewidth differs from the linewidth at half maximum (FWHM or $\Delta H_{1/2}$) by a numerical factor that depends on the particular lineshape.

There are two types of resonance lineshapes in a solid which are referred to as *homogeneously* and *inhomogeneously* broadened.

Homogeneous broadening occurs if the ESR line arises from transitions between spin levels which are intrinsically broadened. Possible mechanisms for this kind of broadening are discussed for example by Poole and Farach (1971). In these cases the resonance line is characterized by T_2 and Eqs. 3.11 and 3.13 apply. As mentioned before (section 3.1.3.1) in dilute spin systems $T_1 \approx \frac{1}{2}T_2$ so that the spin packet widths (see below) are inversely proportional to T_1 according to Eq. 3.13. In cases when the spin-lattice relaxation times T_1 become sufficiently short they can thus determine the overall linewidth of a resonance transition. This will be important for electrons excited to conduction band states in microcrystalline silicon.

On the other hand one speaks of inhomogeneous broadening, if the overall resonance line consists of a number of narrower individual lines due to so-called *spin packets* which add up to yield the observed lineshape. A spin packet is a system of spins which precess with the same Larmor frequency ω_i around their individual magnetic field vectors $\vec{B}_i$. $\vec{B}_i$ is given by the superposition of the external field $\vec{B}_0$ and the local fields $\vec{B}_i^{loc}$ which are different for spins belonging to different spin packets. Sources of inhomogeneous broadening are magnetic field inhomogeneities, unresolved fine structure, unresolved hyperfine structure, crystal irregularities and the dipolar interaction between unlike spins. In general, especially in the context of disordered semiconductors like amorphous or microcrystalline silicon, the local environments of an individual spin may not be identical so that each spin exhibits a slightly different g-shift (see section 3.1.2) leading to a broad resonance line. Assuming a Gaussian distribution of the respective values for the resonant magnetic field, the resulting lineshape would be a *Voigt*-profile, the convolution of a Gaussian with a Lorentzian. Explizit forms can for example be found in the books by Poole, Jr. (1982) or Poole and Farach (1971).

For paramagnetic centers with a certain symmetry one could in principle determine the components of the g-tensor by changing the sample orientation which will in general change the ESR signal. An example of such an oriented paramagnetic state is the well-known dangling bond defect in crystalline environments which possesses axial symmetry with respect to the direction of the unsaturated sp^3-hybrid (Stutzmann and Biegelsen, 1988). Unfortunately, amorphous or microcrystalline silicon are isotropic materials in the sense that all possible orientations of a symmetric defect wave function are present and the ESR signal is their superposition. The resulting shape of the ESR absorption signal is a so-called *powder pattern.* (see e. g. Atherton, 1993; Slichter, 1990, for a detailed discussion). Although a powder pattern also contains information about the angular dependence of the ESR signal and thus about the various g-tensor components, it is often smeared out by the Gaussian broadening mechanism described above so that no such

information can be extracted from it.

In the electron spin resonance of conduction electrons in metals or semiconductors one frequently detects an asymmetric lineshape known as *Dysonian* after the theory developed by Dyson (Dyson, 1955). Its applicability was demonstrated experimentally by Feher and Kip (1955) in metals and by Kodera (1970) in phosphorus doped silicon. The physical origin of the Dysonian lineshape is the fact that an incident microwave only penetrates a conductive sample to a certain depth, the *skin depth*, and that during the measurement conduction electrons will diffuse in and out of the region defined by the skin depth. Its observability depends critically on the relaxation times T_1 and T_2, on the time T_d it takes for an electron to diffuse through the skin depth and the time T_t it takes for the electron to traverse the sample. A good summary can be found in Poole, Jr. (1982).

Finally one mechanism has to be mentioned which can effectively narrow a magnetic resonance line: the effect of motional and exchange narrowing (see f. ex. Anderson and Weiss, 1953; Anderson, 1954, and references to earlier works therein). If electronic spins are interacting with each other (e. g. by dipolar interaction), each spin will experience a slightly different magnetic field leading to a variation in Larmor frequencies and thus a line broadening. If the motion of the spins is rapid enough, however, the variations in local fields can be effectively averaged away resulting in a substantial narrowing of the resonance line. This phenomenon is called *motional narrowing*. Consider now a system where the individual spins $\vec{S}_i, \vec{S}_j$ are coupled to each other by exchange via the Heisenberg exchange Hamiltonian

$$\mathcal{H}_{ex} = \sum_{i,j} 2J\vec{S}_i\vec{S}_j \tag{3.17}$$

with the exchange integral J. Then a part of this interaction can be thought of as flipping neighbouring oppositely oriented spins at a rate $\omega_e = J/\hbar$. This is equivalent to an effective migration of spin orientation through the lattice (Pake and Estle, 1973) leading to a similar line narrowing as for actual motion of the spins. So the physical phenomena of such exchange narrowing and motional narrowing are very similar. The linewidth of the exchange narrowed line can be estimated as (Anderson and Weiss, 1953)

$$\Delta\omega \approx \frac{\overline{\Delta\omega_d{}^2}}{J/\hbar} \tag{3.18}$$

where $\overline{\Delta\omega_d{}^2}$ is the mean squared linewidth of the resonance line (without exchange narrowing) produced by dipolar interaction.

3.1.5 Pulsed ESR

Although performing pulsed ESR measurements was not part of this work, results of pulsed ESR on a-Si:H and μc-Si:H, which were partially carried out simultaneously to the presented CW-studies, will be cited. Therefore a brief comparison of both techniques seems

appropriate. A very good summary of the principles of pulsed ESR can be found in Malten (1996) and for further reading a number of textbooks are available (e. g. Keijzers *et al.*, 1989, and references therein).

Of basic importance is the spin-echo experiment used to study inhomogeneously broadened resonance lines consisting of narrower resonances due to spin packets (section 3.1.4). Recall that a spin packet is a system of spins which precess with the same Larmor frequency ω_i around their individual magnetic field vectors $\vec{B}_i$. In a pulse experiment a temporary external microwave field ('pulse') $\vec{B}_1$ perpendicular to B_0 leads to phase coherence of all spins and a net magnetization in the x-y-plane. After the end of the pulse the phase coherence is lost with the time constant T_2. After a time τ a second pulse of longer duration which flips the magnetizations by 180° can in principle cause the dephased spins to be in phase again after the same time interval τ and lead to the same magnetization in the x-y-plane again (spin echo). However, due to an irreversible interaction of the precessing spins with the surroundings during the experiment, the 'echo'-magnetization is smaller than the one after the first 90°-pulse. This echo decay is described by a third time constant called T_M or *phase-memory time.*

In the analysis of CW-ESR spectra of disordered systems microscopic information is often difficult to extract. Reasons for that are the large linewidths as well as baseline distortions due to slight deviations from the ideal resonator geometry or small contaminations of resonator and sample, which can never be totally excluded. Using the spin echo detected field sweep technique (Malten, 1996, p. 23) it is possible to record absorption spectra similar to the absorption curves obtained by CW-ESR. Here the big advantage of pulsed ESR is that it is sensitive to the different phase-memory times T_M of paramagnetic centers which often results in less disturbances of the spectrum even when detecting very broad lines. Furthermore, the resolution of pulsed ESR experiments is determined by the spin-packet width which can be several orders of magnitude smaller than the inhomogeneous linewidth appearing in CW-ESR. Finally, pulsed ESR provides ways to determine the various relaxation times and gain microscopic information not accessible by CW measurements.

Disadvantages of pulsed ESR techniques are their complexity and the high experimental requirements as well as the fact that it provides no direct information about spin densities, which often is the most important information in the study of material properties from a practical point of view. The best way to gain a maximum of insight is to combine both techniques, which will be attempted in this work by comparing CW measurements with pulsed ESR results if available.

3.2 Transport

As mentioned in the introduction, one of the key questions for a better understanding of microcrystalline silicon used in electronic devices is the mechanism of electronic transport. Some experimental facts and models used to explain them will be outlined below, mainly concerning transport phenomena at temperatures well above liquid helium temperature.

In the second part of this section transport phenomena at very low temperatures, well-known in crystalline silicon, are recalled since they will later (section 5.2) be compared with the low-temperature conductivity in μc-Si:H. Further information on defects and recombination processes important for the discussion of *photo*conductivity data will follow in sections 3.3 and 3.4.

3.2.1 Transport Models - General Features

For a better overview Fig. 3.2 shows the schematic temperature dependences of carrier density or conductivity for different kinds of n-type silicon in an Arrhenius-plot ($\log(n,\sigma)$-vs.-1/T).

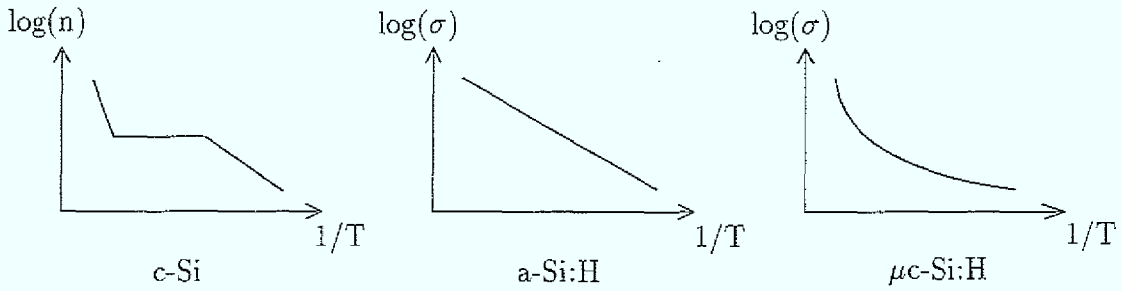

Figure 3.2: Arrhenius plot of the temperature dependence of carrier density in c-Si and conductivity in a-Si:H and μc-Si:H.

The figures represent the conduction band electron density n(T) in crystalline (c-Si), the conductivity in (low defect density) amorphous (a-Si:H) and the conductivity in microcrystalline (μc-Si:H) silicon, respectively.

In c-Si at very high temperatures one is in the intrinsic conductivity region where the thermal energy is sufficient to excite electrons directly from the valence into the conduction band with an activation energy equal to one half of the band gap. With decreasing temperature one enters a region where n(T) is constant and given by the donor concentration N_D, as all of the donors are ionized. Further decrease of T leaves the carriers less thermal energy to be excited from their impurity atoms and the probability grows for the electrons to be recaptured by the ionized donors. In that temperature domain the CB carrier density can again be described by a single activation energy, this time being equal to one half of the energy separation between conduction band edge and donor level. For even lower temperatures the transport mechanism completely changes, as will be described in section 3.2.2.

In high-quality amorphous silicon the conductivity is usually thermally activated, at least over a limited temperature range (Overhof and Thomas, 1989), and is described by

$$\sigma(T) = \sigma_0 \cdot \exp(-\frac{E_\sigma}{k_B T}) \tag{3.19}$$

$$\text{with} \qquad E_\sigma = E_{Tr} - E_F$$

Here the prefactor σ_0 is approximately temperature independent and the activation energy E_σ corresponds to the difference between transport channel (energy E_{Tr}) and Fermi level E_F.

In μc-Si:H the conductivity as a function of temperature does in general *not* show a behaviour characterized by a single activation energy E_σ (Stutzmann *et al.*, 1989; Dubois *et al.*, 1992; Finger *et al.*, 1993, 1994b; Hapke *et al.*, 1996). Such a non-singly activated behaviour appears as a curved line in the Arrhenius-plot of Fig. 3.2.

The conductivity in polycrystalline silicon is sometimes singly activated in a limited temperature range (see e. g. Seto, 1975). In general, however, it can also not be described by one activation energy (Seager and Castner, 1978; Hirose *et al.*, 1979; Taniguchi *et al.*, 1980) and its behaviour somewhat resembles that of microcrystalline silicon.

The description of transport in μc-Si:H is complicated by the presence of the several different phases and interfaces between them. Nevertheless, especially in material with a high crystalline volume fraction, it has mostly been found that the transport is dominated by crystallites and internal boundaries rather than by contributions from rests of the amorphous phase (Spear *et al.*, 1983; Willeke, 1992; Finger *et al.*, 1993; Hapke, 1995; Carius *et al.*, 1997b).

To explain the temperature and doping behaviour of the observed conductivities in μc-Si:H different suggestions have been made. Often the results are interpreted starting from a theory developed for polycrystalline silicon (Seto, 1975; Baccarani *et al.*, 1978; Orton and Powell, 1980) and referred to as *grain boundary trapping model*. In this model the main difference between mono- and polycrystalline semiconductors is the presence of grain boundaries at the interfaces of adjacent grains with a high density of defect states. These defect states can trap charge carriers and thus lead to an accumulation of charges at the grain boundary and the formation of a potential barrier. To explain the non-Arrhenius behaviour in the temperature-dependence of the conductivity in microcrystalline silicon, which does not follow from the above model, a distribution of different barrier heights is assumed leading to a distribution of different activation energies (Finger *et al.*, 1993, 1994b; Hapke, 1995; Backhausen *et al.*, 1997). In addition, for a correct description of the temperature behaviour tunneling through such potential barriers has to be taken into account as suggested by Hapke (1995).

As a distribution of different transport activation energies is also characteristic for *variable range hopping* (VRH) (see next section) through localized states at the Fermi level, this transport mechanism was also considered (Usui and Kikuchi, 1979). However, the model of VRH is not expected to be applicable at temperatures well above liquid helium temperature. In fact, for μc-Si:H samples similar to the material used in the present work it was shown to lead to unrealisticly high density-of-states values (Finger *et al.*, 1993).

Recently a percolation model was used to interpret conductivity and Hall effect data in highly doped (carrier density $n \geq 10^{20}$ cm^{-3}) microcrystalline silicon films (Overhof and

Otte, 1997; Carius *et al.*, 1997b,a). In this model the transport is suggested to proceed through *percolation paths*, i. e. closed paths through interconnected grains. Besides a reasonable description of the temperature dependences of conductivity as well as carrier density and mobility derived from Hall-effect measurements, such a geometrical model can, in particular, also explain the data in samples with different crystalline volume fractions and average crystallite sizes. The increase of conductivity with increasing crystalline volume fraction is due to the effect of a growing number of possible current paths and a decreasing effective length of these paths. The temperature dependence follows from the fact that with increasing temperature (and therefore increasing thermal energy of the charge carriers) more and more paths become available as the carriers can cross barriers of increasing height.

The lack of a single activation energy E_σ makes a simple deduction of the absolute value of the Fermi level position from conductivity data impossible. One can, however, shift the relative position of the Fermi level via doping and roughly estimate the energy range of the Fermi level shift by using Eq. 3.19 and taking the intrinsic sample as a reference. If E_F^i, E_F^n and E_F^p denote the Fermi levels of intrinsic, n- and p-type samples (with the highest doping levels), then the difference between intrinsic and doped samples can be written as

$$|E_F^i - E_F^{n,p}| = |\Delta E_F^{n,p}| = k_B T \cdot \ln(\frac{\sigma_{n,p}}{\sigma_i}) \tag{3.20}$$

With $k_B T = 25$ meV at room temperature and the respective conductivities $\sigma_i = 3.0 \cdot 10^{-6}$ S/cm and $\sigma_n^{max} \approx \sigma_p^{max} = 5 \cdot 10^{-1}$ S/cm for the samples investigated in the present study (section 2.1) this yields $|\Delta E_F^{n,p}| = 0.3$ eV. Thus the total Fermi level shift going from the highest n-type to the highest p-type doping level is about 0.6 eV in this simple approximation.

3.2.2 Transport in Crystalline Semiconductors at Low Temperatures

Transport in lightly n- or p-doped crystalline semiconductors at elevated temperatures mostly proceeds via delocalized electrons in the conduction or holes in the valence band, which have been thermally excited out of their respective impurity levels into the bands. For simplicity the following discussion will again be restricted to n-type semiconductors, in particular phosphorus-doped silicon, with an analoguous reasoning being valid for p-type material. At very low T one arrives at a point where most of the electrons do not move via the conduction band, but directly 'jump' from one donor to another. This kind of conductivity is called *hopping conduction*.

3.2.2.1 Nearest-Neighbour Hopping

If we introduce the quantities r_D which is the average distance to the nearest impurity site and a_0, the fall-off radius (or Bohr-radius in case of hydrogen-like impurities) of the

impurity wavefunction, then — for not too low temperatures and if $r_D \gg a_0$ — electrons hop from one occupied to an adjacent empty donor site. This is referred to as *nearest-neighbour hopping*. Clearly a necessary condition for such a conduction mechanism is the presence of both occupied (neutral) and unoccupied (ionized, i. e. positively charged) donors. At low temperatures this is only possible if there are impurities or defects in the material which can capture an electron from a neutral donor and thus ionize it. In a crystalline semiconductor this can be accomplished by adding a small amount of acceptors (like boron) and is referred to as *compensation*. However, other kinds of impurity or defect states can also act as electron traps and fulfill the same purpose. The necessity of compensation for hopping conductivity was already pointed out as early as 1956 by Mott (1956) and Conwell (1956).

The conductivity resulting from nearest-neighbour hopping depends both on temperature (with a characteristic activation energy ΔE_{hop}) and on the average distance r_D between donors (i. e. between the hopping sites), as the hopping probability is strongly increased with increasing overlap of the wavefunctions and thus decreasing inter-donor distance[4]. An analytical formula (see for example Böer, 1990, pp. 910f) for the hopping conductivity σ_{hop} can be written as

$$\sigma_{hop} = \sigma_{0,hop} \cdot \exp\left(-\frac{\Delta E_{hop}}{k_B T}\right) \tag{3.21}$$

$$\text{with} \quad \sigma_{0,hop} = \sigma_{00} \cdot \exp\left(-\frac{2r_c}{a_0}\right)$$

The quantity r_c differs somewhat from the average inter-donor distance $r_D = [(4\pi/3)N_D]^{-1/3}$, and from percolation calculations it can be estimated as (McInnes and Butcher, 1979)

$$r_c \approx (0.865 \pm 0.015) \cdot N_D^{-\frac{1}{3}} \tag{3.22}$$

The physical reason for the presence of an activation energy ΔE_{hop} is the fact that, to minimize the total energy at low T, all of the positively charged (unoccupied) donors will be close to a negatively charged acceptor. Therefore, to move an electron to such an ionized donor an energy of the order of the Coulomb energy $\frac{1}{4\pi\epsilon_r\epsilon_0} \cdot \frac{e^2}{r_D}$ is required. For low compensation ΔE_{hop} can then be approximated by (Efros *et al.*, 1972)

$$\Delta E_{hop} \approx 0.61 \frac{e^2}{4\pi\epsilon_r\epsilon_0} \left(\frac{4\pi}{3} N_D\right)^{\frac{1}{3}} \tag{3.23}$$

wherein ϵ_0 and ϵ_r are the vacuum permittivity and the static dielectric constant, respectively ($\epsilon_r = 11.9$ for silicon). For higher accuracy and especially for higher compensation Eq. 3.23 has to be modified by a term containing the compensation ratio $K = N_A/N_D$ with the acceptor concentration N_A (see e. g. Efros *et al.*, 1972; Mott and Davis, 1979).

For a given donor concentration N_D and with $N_D \gg N_A$ Eq. 3.21 predicts a straight line in an Arrhenius plot ($\log(\sigma)$-vs.-1/T) in the temperature range where it is valid. Experimentally this was observed in silicon for example by Atkins *et al.* (1960).

[4]Note, however, that the condition $r_D \gg a_0$ still has to be satisfied.

3.2.2.2 Variable-Range Hopping

At sufficiently low temperatures or if r_D becomes comparable with or less than a_0, hopping conduction takes place between states whose energies are very close to the Fermi level (Mott, 1968). In this case the average hopping distance increases with decreasing temperature and hence this kind of hopping mechanism is called *variable-range hopping* (VRH). Provided there is a non-vanishing and approximately constant density of states $N(E_F)$ at the Fermi level, the temperature dependence of the conductivity σ_{VRH} is given by (Mott, 1968; Shklovskii and Efros, 1984, p. 202)

$$\sigma_{VRH} = \sigma_{0,VRH} \cdot \exp\left[-\left(\frac{T_0}{T}\right)^{\frac{1}{4}}\right] \tag{3.24}$$

$$\text{with} \quad T_0 = \frac{C}{k_B N(E_F) a_0^3}$$

In Eq. 3.24 a_0 is again the localization length of the states near the Fermi level and C is a numerical coefficient.

Experimentally, variable range hopping in crystalline semiconductors was observed for example by Bourgoin *et al.* (1979) in phosphorus-ion implanted silicon for temperatures between 100 mK and 4.2 K or by Allen and Adkins (1972) in P-doped Ge for $T < 1$ K.

3.3 Charge States of Defects

To understand ESR and photoconductivity results a few remarks on defect states (this section) as well as excitation and recombination processes (section 3.4) are necessary.

Many localized defects in semiconductors can capture or release electrons or holes and thereby change their charge state. Consider the simple case of a defect which can be either positively charged D^+ (unoccupied), neutral D^0 (occupied by one electron) or negatively charged D^- (occupied by two electrons). Dangling bonds in amorphous silicon are an example for such a defect. They are located within the bandgap of the semiconductor, but their energy position depends on the respective charge state.

Starting from a neutral D^0 dangling bond occupied with a single unpaired electron, the addition of a second electron to the same orbital influences the total energy of the defect in two ways:

1. The two electrons repel each other due to the Coulomb interaction, splitting the energy levels of the D^0 and D^- states, respectively, by an amount of order

$$U_{coulomb} = \frac{e^2}{4\pi\epsilon\epsilon_0 r_0}$$

where r_0 is the effective separation of the two electrons and thus roughly the localization length of the defect wave function (Street, 1991).

2. The addition of the second electron may cause a change in the bonding leading to lattice relaxation at the defect which lowers the energy of the resulting D^- state by the relaxation energy U_{relax}.

Both effects combine to an *effective correlation energy* $U_{eff} = U_{coulomb} - U_{relax}$. A positive U_{eff} means that the energy of the un- or singly occupied defect (D^+,D^0) lies below the one of the doubly occupied state (D^-) by an amount U_{eff}. The result is that, at low temperatures, for a given Fermi level position E_F all states between $E_F - U_{eff}$ and E_F will be singly occupied, whereas states with energies below $E_F - U_{eff}$ can take up a second electron, as even then their energy remains below E_F. The situation is illustrated in Fig. 3.3 for a position of E_F in the upper half of the bandgap. One has to be aware that Fig. 3.3 is a simplified picture, as the shape of the energy distribution changes with occupation and a one-electron (D^0) is mixed with a two-electron (D^-) density-of-states. Still it describes a

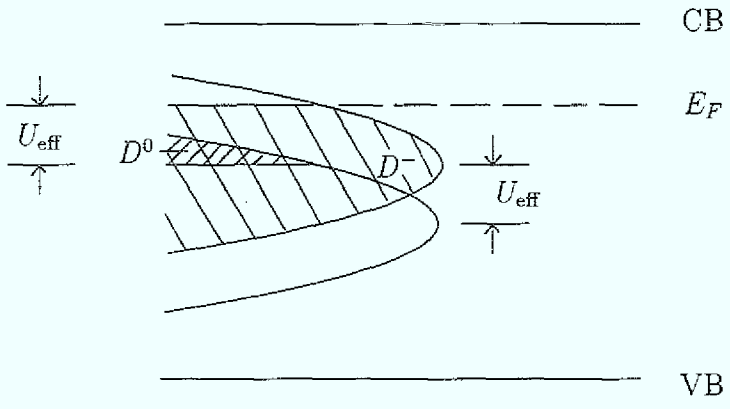

Figure 3.3: Occupation of defect states with positive correlation energy U_{eff}.

number of experimental results, including ESR (see below), very well. Note, however, that another model for the distribution and charge state of defects has been developed recently, which is referred to as *defect-pool model* but will not be treated here (for a recent work containing many references on this subject see Stiebig, 1997).

There is a lot of experimental evidence (one of them being ESR measurements) that dangling bond states in amorphous silicon possess a positive U_{eff}. As ESR is only sensitive to paramagnetic states with an unpaired electron spin, only the singly occupied D^0-defects are detectable. This means ESR measures the states within an energy range between E_F and $E_F - U_{eff}$ for $U_{eff} > 0$. In case of a negative effective correlation energy there would only be a negligible fraction of D^0-defects, and most of the defect states would be empty (D^+) or doubly occupied (D^-) (Street, 1991, pp. 101f). In such a case no ESR signal could be detected in contrast to experiment.

A consequence of Fig. 3.3 is that the defect density as determined by ESR becomes a function of the Fermi level position, as shifts in E_F lead to a re-charging of defects and thus to a change in the number of paramagnetic D^0-states.

3.4 Excitation and Recombination Processes

A few words have to be said about the process of excitation (in this case: optical) and the subsequent recombination of charge carrier pairs. No quantitative description will be given, but only some qualitative features will be lined out briefly.

Electron-hole pair creation can occur directly by exciting an electron from the valence into the conduction band (if the light energy is larger than the band gap energy) and also from states within the gap such as defect, tail or dopant states. The left-hand side of Fig. 3.4 illustrates the various possible processes (upward pointing arrows) assuming one kind of deep defects with $U_{eff} > 0$. Electrons and holes are denoted by filled and unfilled circles, respectively, but for simplicity only the processes for electrons are shown as they are analoguous for holes. After excitation the carriers thermalize, i. e. they successively loose energy by moving rapidly to the band edges and further on into shallow traps such as band tail states, if present.

From there carriers can recombine (downward arrows in Fig. 3.4) either radiatively, thereby emitting a photon, or non-radiatively by emitting one or more phonons. Radiative processes can for example be studied in photoluminescence experiments. In amorphous silicon the dominant radiative recombination mechanism is the transition between conduction and valence band tail states. The transition probability P_{rad} for radiative recombination between localized states depends exponentially on the overlap of electron and hole wave

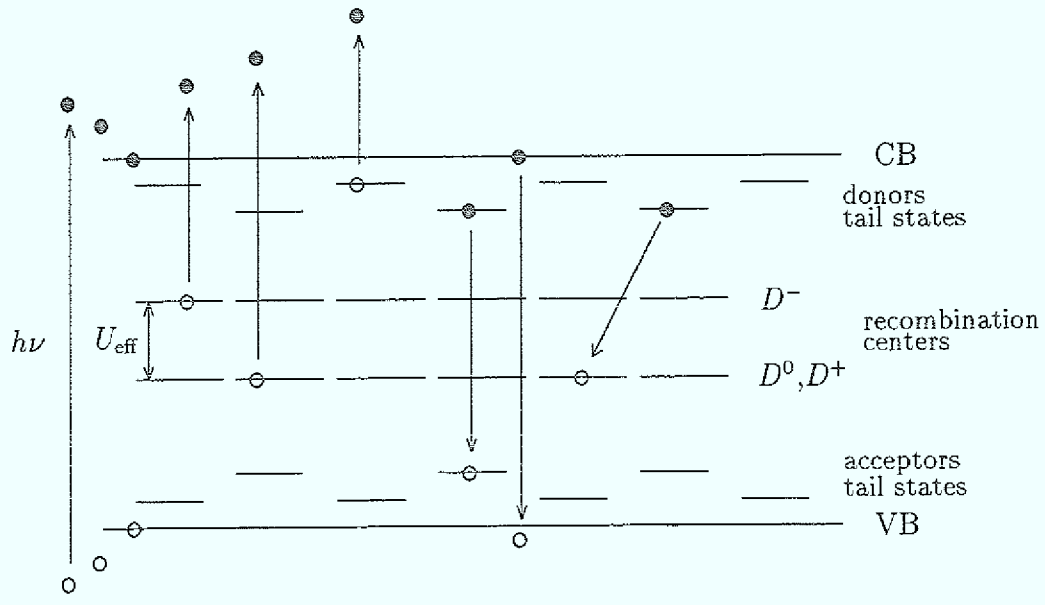

Figure 3.4: Illustration of excitation (upwards-pointing arrows) and recombination (downwards-pointing arrows) processes in a semiconductor with tail states and deep defects.

functions, i. e. on the distance between recombination partners, and can be expressed as

$$P_{rad} = P_0 \cdot \exp(-\frac{2r}{r_0}) \tag{3.25}$$

Here r_0 is the localization radius of the less localized wavefunction and P_0 the transition probability for complete overlap (Street, 1991, p. 278). Non-radiative recombination often takes place via so-called *recombination centers*, i. e. deep-lying defects which can effectively capture excess carriers. In that case the energy difference between initial and final state is too large to be taken up by a single phonon and thus involves the emission of multiple phonons. Then the recombination probability is strongly dependent on the transition energy of the recombination.

One further distinguishes between *geminate* and *non-geminate* recombination. Recombination is geminate if the optically created electron-hole pair does not dissociate and the same electron and hole recombine with one another. Non-geminate recombination involves electrons and holes which have not been excited by the same photon. Geminate recombination occurs preferably at low temperatures and low density of charge carrier pairs, when the thermal energy is insufficient to separate the pair and the overlap between neighbouring pairs is negligible.

Under steady-state conditions the density of light induced pairs N can be expressed in terms of the optical generation rate G and the mean carrier lifetime τ:

$$N = G \cdot \tau \qquad [G] = [\frac{1}{\mathrm{cm}^3 \cdot \mathrm{s}}] \tag{3.26}$$

Here G denotes the number of optically created charge carrier pairs per second and unit volume. Determination of the photoconductivity σ_{ph} additionally requires the knowledge of the carrier mobility μ. Then σ_{ph} can be expressed as

$$\sigma_{ph} = \eta N e \mu \overset{(3.26)}{=} \eta G \tau e \mu \tag{3.27}$$

where the factor η means the probability that a light induced charge carrier takes part in the conduction process. Frequently Eq. 3.27 is used in the form

$$\eta \mu \tau = \frac{\sigma_{ph}}{Ge} \tag{3.28}$$

The $\eta\mu\tau$–product can be understood as a measure of the photoconductivity per one absorbed photon.

Chapter 4

Experimental Details

Having presented some characteristics of the microcrystalline material and some useful background information, the practical aspects of ESR and (briefly) conductivity measurements will be described in the following.

4.1 ESR Measurements

For ESR in this work a commercial X-band spectrometer (BRUKER ESP 380E) with both CW and pulsed ESR capabilities was used. The microwave source is a reflex klystron operating at a frequency around 9.3 GHz and a maximum power output of about 200 mW. The exact frequency is a function of cavity loading (and hence depends on the specific sample). During an ESR experiment it is approximately constant and the resonance condition is reached by scanning the magnetic field B_0. The ESR signal of a sample inside the resonant cavity is obtained in the following way: Far away from sample resonance the cavity with the sample is critically coupled to the wave guide transmitting the power from the klystron source. This means that no power is reflected at the joint of waveguide and cavity. If the sample comes close to resonance it will absorb energy from the microwave field inside the cavity. As a result, the coupling changes and a certain fraction of the microwave power is reflected. A Schottky-barrier diode detects the reflected microwave power which is seen as the experimental ESR signal. As common in ESR practice, phase-sensitive detection is employed and the measured signal intensity is proportional to the first derivative of the absorbed (or reflected) power. The area under the absorption curve, which is proportional to the total number of spins of all the paramagnetic species contributing to the ESR signal, is then obtained by a double numerical integration (see appendix A).

A cylindrical transverse magnetic TM_{110} and a rectangular transverse electric TE_{301} cavity were available as microwave cavities for CW measurements. Both cavities have optical viewports for light induced ESR experiments. They are purged with small amounts of dry nitrogen during the measurement to avoid condensation of water at the cavity walls. Measurements were performed in the temperature range between 4.5 K and 300 K usually with 100 kHz modulation frequency and a modulation amplitude of 2–4 G. To

enhance broad resonances sometimes larger modulation amplitudes were preferred. Whenever this was the case it will be mentioned in the text. The maximum power output of the klystron microwave source of about 200 mW can be attenuated in the range 0–60 dB, 60 dB corresponding to approximately 0.2 μW. To avoid saturation (see section 3.1.3.1) at a temperature of 40 K the microwave power used was usually not higher than 7 μW, since at this power level saturation effects can be neglected. Details will be given together with the experimental results.

The samples are cooled in a He gas flow cryostat (Oxford ESR 900), where the sample is mounted approximately 1 cm above the gas outlet and the AuFe/Chromel-thermocouple used to measure the temperature. This leads to a slight difference between the temperature reading and the sample temperature (the 'real' sample temperature is expected to be slightly higher). The difference was checked regularly, independent of the thermocouple calibration, by comparing the temperature reading with the temperature expected from the line intensity of our standard sample (see below) relative to its room temperature value, which behaves Curie-like in the whole temperature range. A maximum deviation of 15 K in the intermediate temperature range (200 K) was found. For lower temperatures and near room temperature the difference is much less. Also the relative temperature deviation when measuring different samples at the same temperature reading is much smaller.

For a quantitative analysis of the ESR data (calculation of g-value and spin density or number of spins) calibration by a well-defined standard is necessary. A widely used standard sample is the organic compound 1,1-diphenyl-2-picrylhydrazil (DPPH). As for routine measurements the use of DPPH turned out to be too tedious (for example the substance is not stable under light exposure), a sputtered amorphous silicon sample with a fixed and stable number of spins was used as a secondary standard and calibrated versus DPPH [1]. The uncertainty of the resulting absolute number of spins ($1.6 \cdot 10^{15}$) in the secondary standard was estimated by Malten (1996) to be a factor of 2. Details on the calculation of spin densities for the various samples and some further experimental considerations are given in appendix A.

Through the optical viewport in both resonant cavities the samples can be exposed to light during the ESR experiments yielding what will be called the *light induced* ESR signal, abbreviated LESR, in contrast to the dark ESR signal or DESR. To avoid any confusion it is emphasized that the term LESR means the whole of the observed signal under light illumination rather than the difference between the spectra with and without illumination, as can sometimes be found in literature. For LESR the main light source was a 100 W halogen lamp used in conjunction with various band-pass and cut-off filters. It can be switched off with a mechanical shutter. For a standard experiment a heat-filter (transmission only for $h\nu \geq 1.75$ eV) was placed between resonator viewport and lamp to avoid unintentional heating of the sample by infrared light absorption.

The problem when illuminating powdered specimens is the heterogeneity of the material. Incident light will undergo various kinds of reflections, refractions and absorptions

[1] This work was done by C. Malten and is appreciated (see Malten, 1996, p. 12).

depending for example on the packing density of the powder. Thus the light induced excitation of electrons or holes will not be uniform throughout the sample. Furthermore the "sample thickness" given as the diameter of the ESR sample tubes (4 mm) exceeds by far the penetration depth of the incident light which is less than 5 μm for heat-filtered white light with $h\nu \geq 1.75$ eV. Thus the main part of the sample volume will not be directly illuminated at all. This makes an exact quantification of the light induced effects in powder samples impossible. As the measurements described here were mainly performed on powdered samples due to the much higher signal intensity, a better quantification should be the task of future work.

To monitor the transient behaviour of the LESR signal the magnetic field is kept constant (instead of the usual magnetic field sweep) at the maximum or minimum of a given resonance line. (As the observed ESR lines are the derivatives of the absorption signal this means in practice that one modulates the B-field around the points of maximum slope of an absorption curve). If the light source is switched on and off at times t_1 and t_2, respectively, it is possible to monitor the rise and decay of the light induced signal on a time scale. The experiment is illustrated in Fig. 4.1. Here a typical LESR rise-and-decay curve is shown together with the corresponding ESR spectra before turning on the illumination and at different times during the decay. Transient measurements yield important information about recombination processes and carrier lifetimes. By applying various illumination and dark sequences using different filters (for example a germanium-filter, which only transmits infrared light with an energy ≤ 0.67 eV) a large number of experiments is possible. Unfortunately, however, the low energy cut-off in the given experimental set-up is limited by the IR transmission of the ESR cryostat glass ware (i. e. 0.56 eV) letting no light below this energy reach the sample. This means that the system of Ge-filter and cryostat glass ware acts as a band-pass centered at approximately 0.60 eV with a bandwidth of 0.11 eV. Transient measurements will be presented in section 6.2.

4.2 Conductivity Measurements

Conductivity measurements were performed on samples deposited on roughened glass substrates in the same run as the powdered samples used for ESR experiments (see section 2.1). After deposition coplanar silver contacts (thickness 800 nm) were evaporated under high vaccuum with a width $l = 4$ mm, an electrode spacing $b = 0.5$ mm and sample thicknesses d of several microns. For low-conductivity samples ($\sigma < 10^{-5}$ S/cm) conductivity was measured under vacuum to avoid errors due to surface coverage. The roughness of the samples increases the length of the path the charge carriers have to travel from one contact to the other, but the uncertainty resulting from the roughened surface is estimated to be less than a factor of 2. Having determined the resistance R or, alternatively, the current I

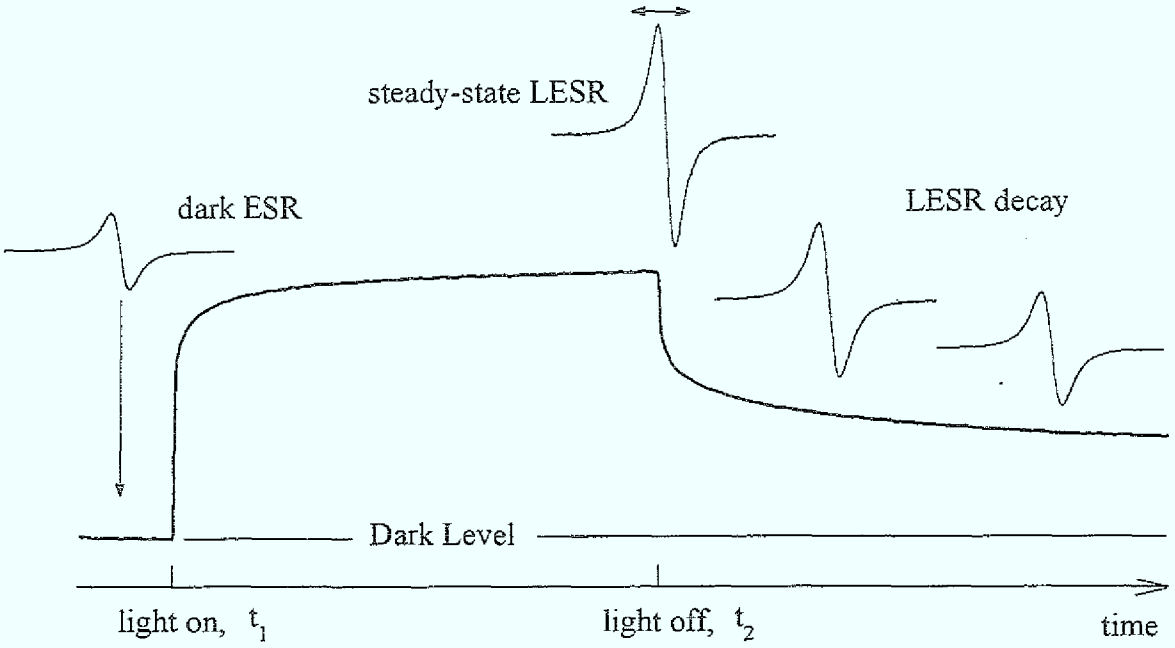

Figure 4.1: Illustration of LESR transient experiment. The transient curve starts at $t < t_1$ without illumination. At times t_1 and t_2 the light is turned on and off, respectively, leading to the decay of the LESR signal for $t > t_2$.

for an applied voltage U the conductivity σ is simply given by

$$\sigma = \frac{1}{R} \cdot \frac{b}{ld} = \frac{I}{U} \cdot \frac{b}{ld} \tag{4.1}$$

Temperature dependent measurements of both dark (σ_d) and photo conductivity (σ_{ph}) were possible in a similar temperature range as ESR experiments, i. e. between 4.2 K and room temperature using a He bath cryostat. Photoconductivity experiments were done by illuminating the sample with krypton laser light at a wavelength of 752 nm. At this wavelength the light has a penetration depth in μc-Si:H of about 10 μm thus ensuring a homogeneous illumination of the whole sample volume with typical sample thicknesses of several microns. The maximum power density of the laser light incident on the sample was 500 mW/cm^2 corresponding to a photon flux of $2 \cdot 10^{18}$ photons per second and cm^2. The intensity could be varied over 3 orders of magnitude via different grey-scale filters.

Chapter 5

Measurements in the Dark

In the preceding chapters it should have become clear that a lot of microscopic information can be gained from ESR experiments. Many conclusions can already be drawn from measurements under thermal equilibrium without any external influence on the occupation of electronic states. Therefore in the following chapter results from measurements without light illumination will be presented and interpreted with respect to their consequences on the microscopic picture one has of μc-Si:H. The subsequent chapter 6 proceeds one step further and is concerned with the effects of various light illumination conditions.

5.1 ESR Measurements

5.1.1 General Features

As a basis for the whole following discussion the general features appearing in ESR measurements on microcrystalline silicon will be described. The important differences between spectra of n-type on the one hand and p-type or intrinsic samples on the other hand are illustrated in Fig. 5.1, where ESR spectra of an intrinsic as well as one n- and one p-type sample of similar doping level are shown.

The spectra were recorded at a temperature of T = 40 K and are normalized to the same peak-to-peak intensities for better comparison, although the three samples had different spin densities. In addition to the original data numerical fits are included as the broken lines in Fig. 5.1. For details on the fitting procedure see the end of section 5.1.1.1.

5.1.1.1 Defect States

In all microcrystalline silicon samples two resonances at g = 2.0052 $\pm$ 0.0004 and g = 2.0043 $\pm$ 0.0002 can be identified. Both of them are ascribed to defect states. The former resonance at g = 2.0052 is attributed to neutral silicon dangling bond states (DB, $\bullet$Si$\equiv$Si) D^0 (Finger *et al.*, 1994b; Malten *et al.*, 1995; Ehara, 1997; Kondo *et al.*, 1998) similar to the ones found in amorphous silicon at a slightly different g-value of g = 2.0055 (Street, 1991). Strong evidence for the identification as dangling bond states with a g-value at

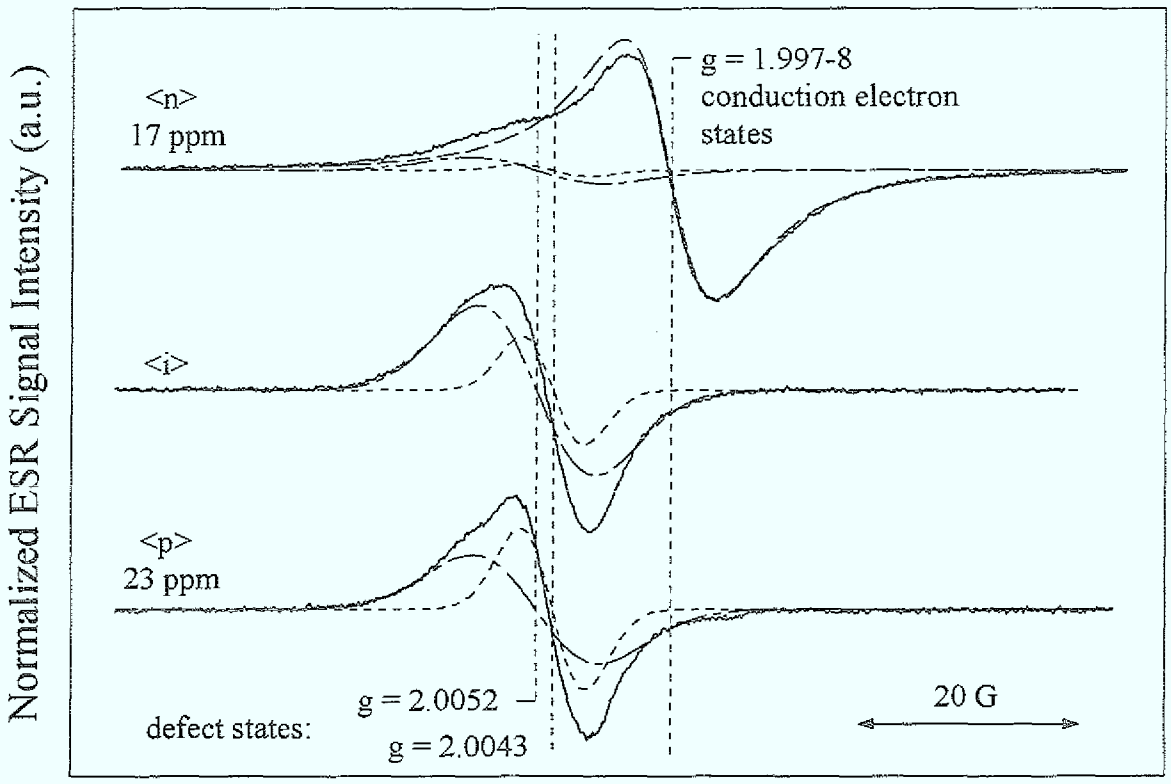

Figure 5.1: Normalized ESR spectra of intrinsic, n-type and p-type microcrystalline silicon recorded at 40 K. Numerical fits of the defect resonances (dotted and dash-dotted lines) and the CE resonance (long-dashed line) are included.

2.0052 comes from studies of electron irradiated material where an increase by a factor of 10 of the resonance at g = 2.0052 is obtained (Malten *et al.*, 1995).

This shift of the g-value in μc-Si:H with respect to the one observed in a-Si:H is in accordance with measurements on polycrystalline silicon (Hasegawa *et al.*, 1982; Ballutaud *et al.*, 1986; Hasegawa *et al.*, 1995). A signal at g = 2.0052$\pm$0.0003 has also been observed as a quenching signal in electrically detected magnetic resonance (EDMR) measurements and was assigned to the recombination of electrons with D^0-states (Will *et al.*, 1997; Lips *et al.*, 1998). Finally Depinna *et al.* (1983) found a quenching signal at g = 2.005 in optically detected magnetic resonance (ODMR) experiments and interpreted it as arising from amorphous intercrystallite regions or defects similar to those observed in radiation damaged crystalline silicon.

The resonance at g = 2.0043 cannot be unambiguously identified by means of its g-value having in mind the large number of possible paramagnetic defects in bulk silicon,

at grain boundaries and at Si/SiO_2 interfaces (see references in Finger *et al.*, 1998). One may notice the similarity with the well-known g-value of g = 2.0043 ascribed to conduction band tail electrons in amorphous silicon (Street, 1991). However, such an interpretation seems unlikely, as in the first place the fraction of amorphous tissue is expected to be very small in our highly crystalline material and secondly – as the main reason – because this resonance appears with comparable intensity as the DB-resonance even in p-type samples, where we would not expect any occupied conduction band tail states in the dark.

Instead there are some arguments pointing to an identification of the g = 2.0043 resonance as dangling bond-like states at grain boundaries containing oxygen or in SiO-layers within the material. The first hint is the fact that some microcrystalline films incorporate a considerable amount of oxygen already within a very short exposure time to air. This was concluded from SIMS (secondary ion mass spectroscopy) measurements (Mück, 1997). The amount of built-in oxygen depended on the sample storage time under atmospheric conditions and was in the range of 10^{19}–10^{21} cm^{-3}, which is appreciably higher than the measured defect densities. As even for He-atmosphere sealed powder samples air exposure for several hours cannot be avoided, it is possible that ESR samples also contain a similar amount of oxygen. Secondly we note similarities to measurements on porous silicon or amorphous SiO_x-layers. In porous silicon Young *et al.* (1997a) observed a resonance at g = 2.0045 ± 0.0003 and attributed it to dangling bond states in Si-rich SiO-films. Holzenkämpfer *et al.* (1979) reported similar g-values for irradiated SiO_x-films with $x \approx 0.5$. Finally Will (1996) and Lips *et al.* (1998) also observed an increase of a signal at g = 2.0044 in μc-Si:H powder samples that were exposed to air for several weeks and also interpreted it in connection with incorporated oxygen during the storage time.

To obtain spin densities and line parameters for the superimposed resonance lines a numerical fitting procedure had to be applied. As the resonance lines are considerably broadened by the disorder, no (asymmetric) powder spectrum (see section 3.1.4) is detected. Instead they can be well approximated by the first derivatives of Gaussian lines with 3 fitting parameters each (amplitude, peak center and peak-to-peak linewidth ΔH_{pp}). The latter is defined as the linewidth between points of maximum slope of the absorption curves and hence between the maximum and the minimum of the first derivative. Unrestricted fits on p-type and intrinsic samples all yielded similar g-values the averages of which were 2.0043 and 2.0052 with the indicated error margins. Thus when looking at intensities and linewidths, especially when applying the fitting procedures to n-type samples (where at higher doping levels fitting of the defect state resonances with 6 adjustable parameters becomes quite arbitrary due to the dominance of the CE line), the g-values were fixed at their respective positions at g = 2.0043 and g = 2.0052.

5.1.1.2 Conduction Electron States

In n-type samples (and even in some intrinsic samples which are, however, not treated extensively in this work) an additional resonance appears with g-values between 1.9972 and 1.9983 depending on the doping level (long-dashed line at g = 1.9979 for sample n17

in Fig. 5.1). This resonance has been attributed to conduction electrons in the crystalline grains and is referred to as conduction electron (CE) resonance. Such an identification seems plausible for a number of reasons. Firstly because of the g-value, which is very different from the g-values of defects and close to the g-value of conduction electrons in crystalline silicon (Portis *et al.*, 1953; Kodera, 1964; Young *et al.*, 1997b), where usually – at least at low temperatures – no clear distinction is made if these electrons are (1) in delocalized conduction band states or (2) in shallow traps or at their donor sites. Secondly the linewidth of the corresponding ESR resonance increases between 20 K and 300 K (see section 5.1.3.2) like in crystalline silicon (Portis *et al.*, 1953; Kodera, 1969). Thirdly the spin -lattice relaxation times T_1 as measured by pulsed ESR techniques (Malten *et al.*, 1997; Finger *et al.*, 1998) are about three orders of magnitude shorter than what is found for the defect states (at T = 20 K), similar to T_1 times reported for crystalline silicon (Feher and Fletcher, 1956; Feher and Gere, 1959; Maekawa and Kinoshita, 1964; Nagashima and Yamasaki, 1976).

As in case of the defect resonances a numerical fit of the CE line is included in Fig. 5.1 as the long-dashed line. Here the fit curve is the first derivative of a Lorentzian, but a few more words have to be said about the lineshape of the CE resonance. For the lowest doping levels the line shape of the CE resonance is asymmetric and can be nicely approximated by a Gaussian line with an exponential 'tail' to account for this asymmetry. This has also been found for nominally intrinsic samples, if a CE line can be detected (Finger *et al.*, 1998). For higher doping levels the line approaches a symmetrical and more and more Lorentzian lineshape.

The origin of the asymmetric lineshape for samples with little doping is still unclear. Taking into account the conductivities and the sample dimensions, a Dysonian lineshape effect (Dyson, 1955, see also section 3.1.4) can be excluded (for a discussion see Finger *et al.*, 1998). The lineshape is Dysonian for the conduction electron resonance in a solid sample of crystalline silicon with sufficiently high doping level and a sample thickness large compared to the skin depth (Dyson, 1955; Kodera, 1969). However, if powdered specimens with particle sizes of not more than several microns are used, the lineshape is essentially Lorentzian (Portis *et al.*, 1953; Kodera, 1964, 1966). To be able to compare resonance intensities without additional errors due to varying line shape functions, the Lorentzian lineshape is adopted for numerical fits of the CE line in all samples.

It has to be emphasized once again that the term 'conduction electrons' in this context is still used both for localized electrons (in shallow traps or at their donor states) and for delocalized conduction band electrons. It is in fact one of the aims of this work to clarify this distinction and make it possible to attribute the ESR signal under specific conditions unambiguously to distinct electronic states.

5.1.1.3 Hole States

An important problem shall be briefly discussed at this point: In view of the clearly observable conduction electron line in n-type samples invariably the question arises, why there is no similar feature visible in the spectra of p-type material which can be attributed to hole states.

The answer is readily given by a look at the situation in p-doped crystalline silicon, where also in general no resonances of hole states are found in ESR. Their missing in c-Si is associated with the degeneracy of the Si valence band at $\vec{k} = 0$ ($\vec{k}$:= wavevector), which consists of a fourfold and a twofold degenerate set of states with the respective values of 3/2 and 1/2 for the total angular momentum J (Kohn, 1957; Ludwig and Woodbury, 1962). Local random strains due to dislocations, imperfections and lattice vibrations lift this degeneracy and therefore split the valence band. If this splitting is of the order of the ESR transition energies $g_h \mu_B B_0$ (g_h := hole g-factor), all possible ESR transitions are allowed and the spin-lattice relaxation time becomes very short. In addition the splitting varies from site to site due to the local variations in internal strain leading to a distribution of ESR transition energies and therefore g-values. Both effects result in a strong line broadening and render any ESR resonance of hole states unobservable.

This problem can be overcome only by applying additional *external* strain as demonstrated experimentally by Feher *et al.* (1960) or by using extremely pure crystals where the internal strains present are substantially reduced (Neubrand, 1978).

In microcrystalline silicon locally and randomly varying internal strains will always be present due to the disordered nature of the material, and thus the absence of any hole resonance in CW-ESR is easily explained with the same arguments.

Note, however, that recent electron spin echo detected field sweep measurements (section 3.1.5) on the p-type samples used in the present study showed a broad resonance line at g = 2.1 ($\Delta H_{pp} \approx 500$ G), which might be ascribed to hole states (Malten *et al.*, 1997).

5.1.1.4 Doping Dependence

To get an overview right from the beginning stack plots of ESR spectra obtained at T = 40 K for the various p- and n-type doping levels are shown in Figs. 5.2 and 5.3, respectively. Fig. 5.2 additionally includes a spectrum of an intrinsic sample. The respective resonance positions of the defect and the CE states are indicated by the dashed vertical lines. It is emphasized that the spectra are again normalized, and therefore no conclusions concerning the absolute signal intensities can be drawn from Figs. 5.2 and 5.3.

In both figures the ordering of the samples with different doping levels follows the shift of the Fermi level, i. e. for p-type material (Fig. 5.2) the sample with a position of the Fermi level closest to the valence band edge is shown at the bottom. Going from bottom to top E_F moves towards the middle of the gap. For n-type samples (Fig. 5.3) the bottom spectrum corresponds to a position of E_F close to midgap and the Fermi level moves further on towards the conduction band edge going to higher doping. The respective direction of the Fermi level shift is indicated by the arrows on the right-hand side of each figure.

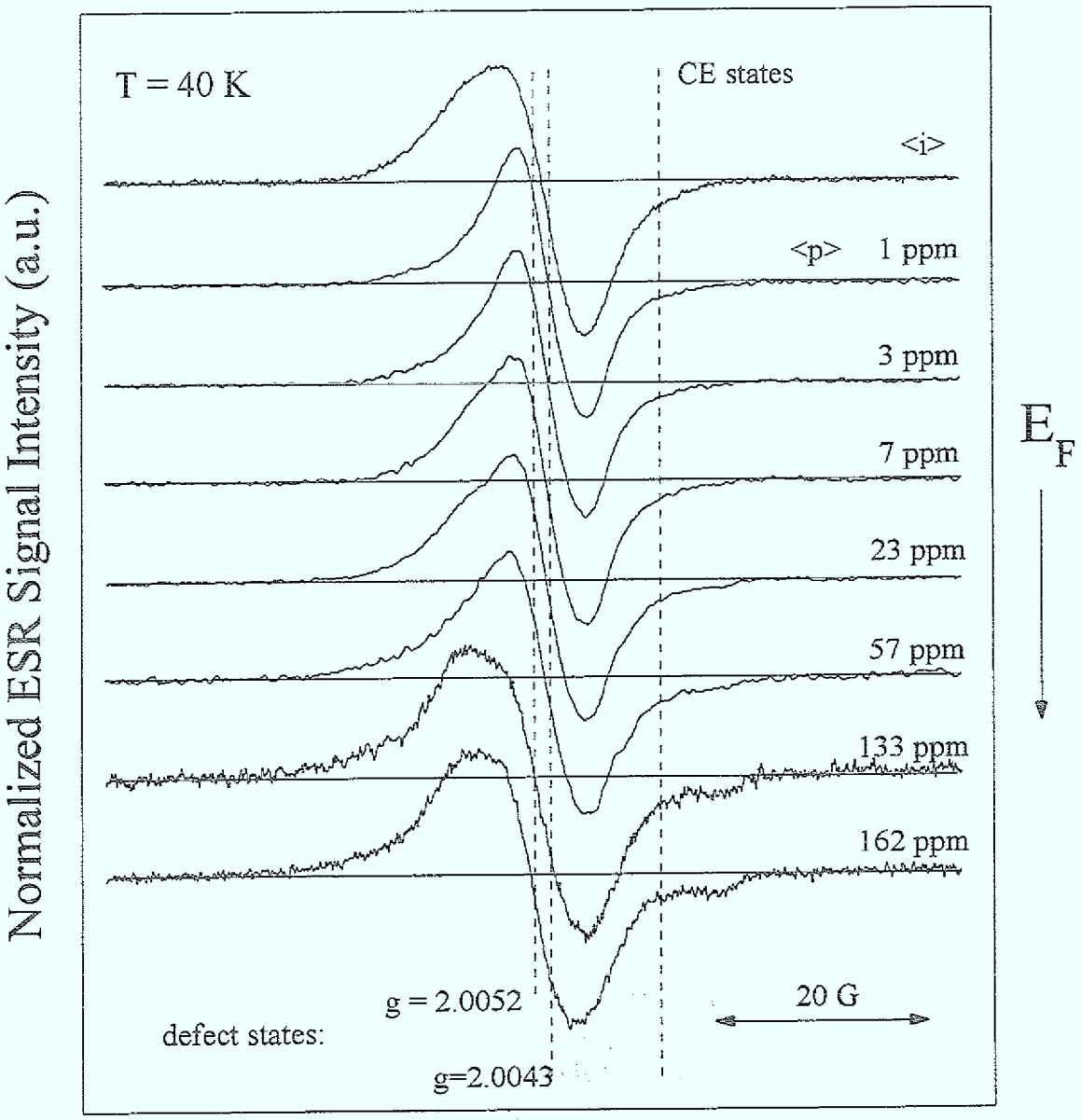

Figure 5.2: Normalized ESR spectra of p-type μc-Si:H with gas phase doping levels between 1 and 162 ppm recorded at 40 K in the dark. Also included is the spectrum of the intrinsic sample i95 (top). The arrow on the right-hand side indicates the direction of the doping-induced Fermi level shift.

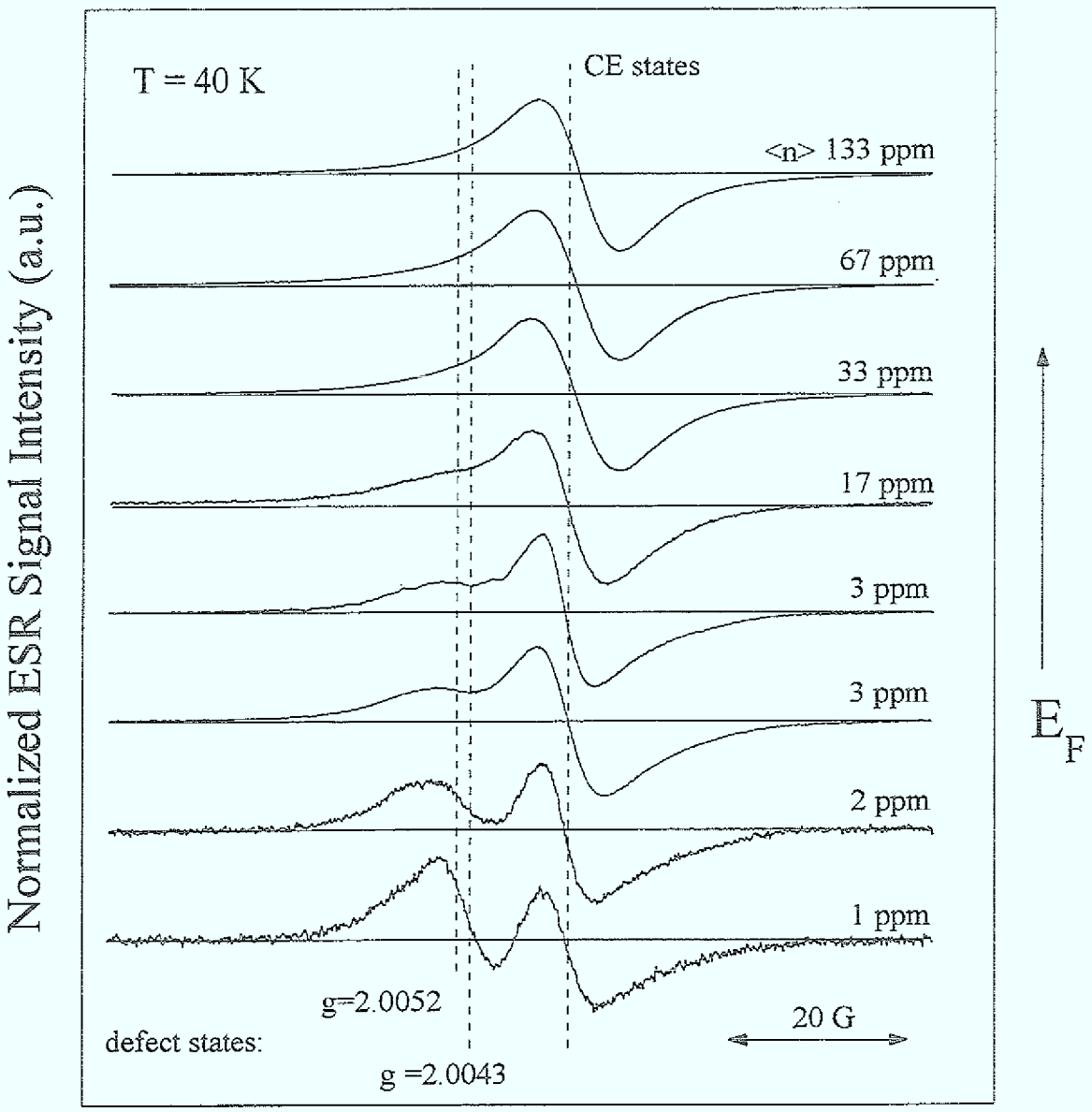

Figure 5.3: Normalized ESR spectra of n-type μc-Si:H with gas phase doping levels between 1 and 133 ppm recorded at 40 K in the dark. Like in Fig. 5.2 the arrow on the right-hand side indicates the direction of the doping-induced Fermi level shift.

Even without any detailed analysis it is evident from Fig. 5.2 that the relative fraction of the respective defect state resonances at g = 2.0043 and g = 2.0052 changes with doping level. This can be seen both from the change of the shape of the double peak structure and the change in the zero-crossing point of the derivative spectra which indicate a shift in the average g-value. With increasing p-type doping level the line at g = 2.0052 becomes more pronounced with respect to the second defect resonance. A more detailed analysis (including the intrinsic sample) will follow in section 5.1.2. There is an additional structure in the spectra of p-type samples close to the position of the CE line which develops with doping, but whose origin is unclear at the present time. As it increases with increasing *p-type* doping level, it cannot be due to conduction electron states. An identification is difficult and left for future work.

Some characteristic doping-related effects on the ESR spectra in n-type samples can also be nicely seen in Fig. 5.3. For the lowest doping levels the superposition of defect and CE resonances is easily visible meaning in these samples both resonance appear with similar intensities. With increasing doping level the CE line more and more dominates the spectra and the defect states cannot easily be distinguished any more for doping above 33 ppm.

The following sections 5.1.2 and 5.1.3 will treat defect and CE states separately as they are due to principally different kinds of electronic states within the material. In doing this we will come back to some of the features already mentioned above, and a second look at the stack-plots of Figs. 5.2 and 5.3 might at times be helpful.

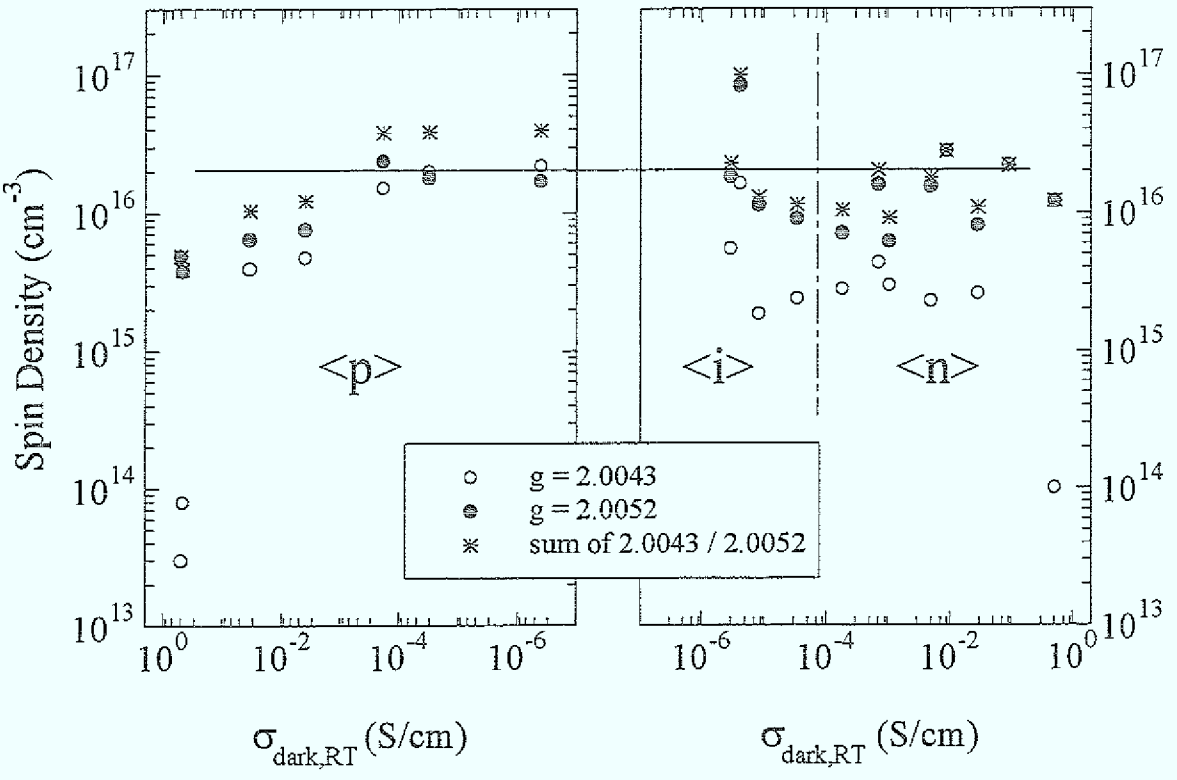

Figure 5.4: Spin densities of defect states for p- and n-type samples vs. σ_d^{RT}.

5.1.2 Defect States

5.1.2.1 Signal Intensity

a. Doping Dependence

Fig. 5.4 shows the spin densities of the two defect resonances at g = 2.0043 and g = 2.0052 as well as the sum of both (i. e. the overall defect spin density) plotted versus room temperature dark conductivity for p-doped (left-hand side) and n-doped (right-hand side) material. As σ_d^{RT} steadily increases with increasing gas phase doping ratio both for p- and for n-type samples (Fig. 2.1, p. 8) the plot represents the changes in spin density with variations of the doping level. Included are the intrinsic samples, separated by the broken line, on the n-side of the figure as nominally undoped material tends to be slightly n-type.

Two defect lines are well distinguished and can be nicely deconvoluted in p-type and intrinsic samples. For n-type material both the relative and the absolute defect line intensities are less reliable due to the asymmetric CE lineshape in lightly doped and the very high CE intensity in heavily doped samples. Therefore the uncertainty in the defect densities is larger by about a factor of 2 compared to p-doping.

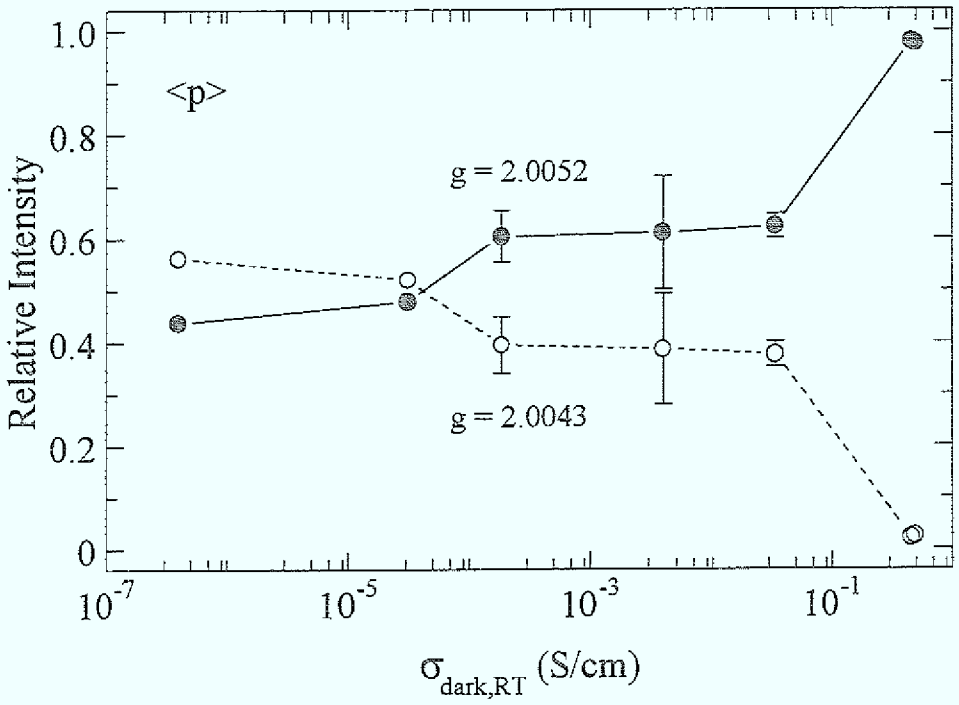

Figure 5.5: Relative intensities of defect states at g = 2.0043 and g = 2.0052 as a fraction of the overall defect state intensities in p-type samples versus σ_d^{RT}.

Fig. 5.4 shows some interesting features:
(1) The overall defect density – although slightly higher for lightly p-doped samples – is surprisingly constant around $N_s = 2 \cdot 10^{16}$ cm^{-3} ($4 \cdot 10^{16}$ cm^{-3} for light p-doping) over a wide doping and conductivity range.
(2) In case of p-doping the spin density is constant up to a conductivity of about $2 \cdot 10^{-4}$ S/cm (corresponding to 7 ppm) but decreases for higher doping by one order of magnitude down to $N_s = 4 \cdot 10^{15}$ cm^{-3}.
(3) The relative intensity of the resonances at g = 2.0043 appears to be systematically lower compared to g = 2.0052 on the side of n-doping. For p-doped samples, on the other hand, the relative fraction of both resonances with respect to each other changes considerably with doping. To illustrate this in p-type samples, the relative intensities of the lines at g = 2.0043 and g = 2.0052 are plotted as a fraction of the overall defect spin density versus σ_d^{RT} in Fig. 5.5. The intensities are of comparable magnitude for lightly p-doped samples but the resonance at g = 2.0052 dominates the signal more and more as one goes to higher doping levels.

For an interpretation of these results a comparison with amorphous silicon is instructive. In amorphous silicon a distinct defect peak with a width (FWHM) of 0.2 eV is

found near the center of the mobility gap of 1.75 eV (Stutzmann, 1987). This is exhibited by a decrease of the observed ESR spin densities, if one shifts the Fermi level away from a close-to-midgap position by doping: Paramagnetic neutral D^0 states become either negatively (D^-) or positively (D^+) charged and thus do not have an unpaired spin any more to be detectable in ESR. In a homogeneous material the fact that the defect spin density is constant over a wide doping range indicates a broad and flat energy distribution of defect states within the band gap.

With the following two assumptions the spin densities of the respective defect states given in Fig. 5.4 can be translated into a density-of-states (DOS) picture as a function of the energy position within the gap: (1) To estimate the energy position[1] we use Eq. 3.20 on page 26 taking the conductivity of the 95 MHz intrinsic sample ($\sigma = 3.0 \cdot 10^{-6}$ S/cm) as reference and (2) we assume the same effective correlation energy U_{eff} as for DB-states in a-Si:H of $\approx$0.3 eV (Stutzmann *et al.*, 1987) to calculate the DOS. Note that a value between 0.3 and 0.4 eV has recently also been found for the correlation energy of dangling bond defects in polycrystalline silicon (Jousse *et al.*, 1991). The existence of an appreciable U_{eff} will be justified shortly by the observation of Curie-like behaviour and later by the fact that ESR signals of donor states and defects are detected simultaneously. The DOS is then simply obtained by deviding the values for the spin densities by U_{eff}. The result of this procedure is shown in Fig. 5.6. The broken line indicates the midgap position ($E = 0$) which was taken to coincide with the energy position of the compensated sample p1. The positions of conduction and valence band edge have intentionally not been marked, since the exact location of the defect states and hence the band gap, which has to be used, are unknown.

Although the uncertainties are quite large, it is seen that the DB-resonance at g = 2.0052 is spread over an energy range of at least 0.6 eV and appears to have a much broader distribution than the defects with g = 2.0043.

One reason for that could be a larger effective correlation energy U_{eff}, but without additional data such an interpretation remains speculative.

Furthermore some care is needed concerning the dependence of the resonance at g = 2.0043 on the Fermi level position. Note first that the lines in Fig. 5.6 are only guides for the eye and in particular the spin density values for g = 2.0043 exhibit a large spread on the n-side. Assuming this resonance to be connected with incorporated oxygen, it cannot be ruled out that its intensity variation is mainly due to different amounts of built-in oxygen rather than a doping-induced Fermi level shift. Such a variation in oxygen content might for example be caused by small changes in the microstructure with doping which influence the in-diffusion of oxygen. Another possibility are variations in air exposure time during sample preparation, especially when considering the large scatter of the intensities at g = 2.0043 in n-type samples. To unambiguously clarify these questions, detailed

[1]Strictly speaking 'energy position' means the relative position of the Fermi level and the observable defect states lie within an energy range between $E_F - U_{eff}$ and E_F.

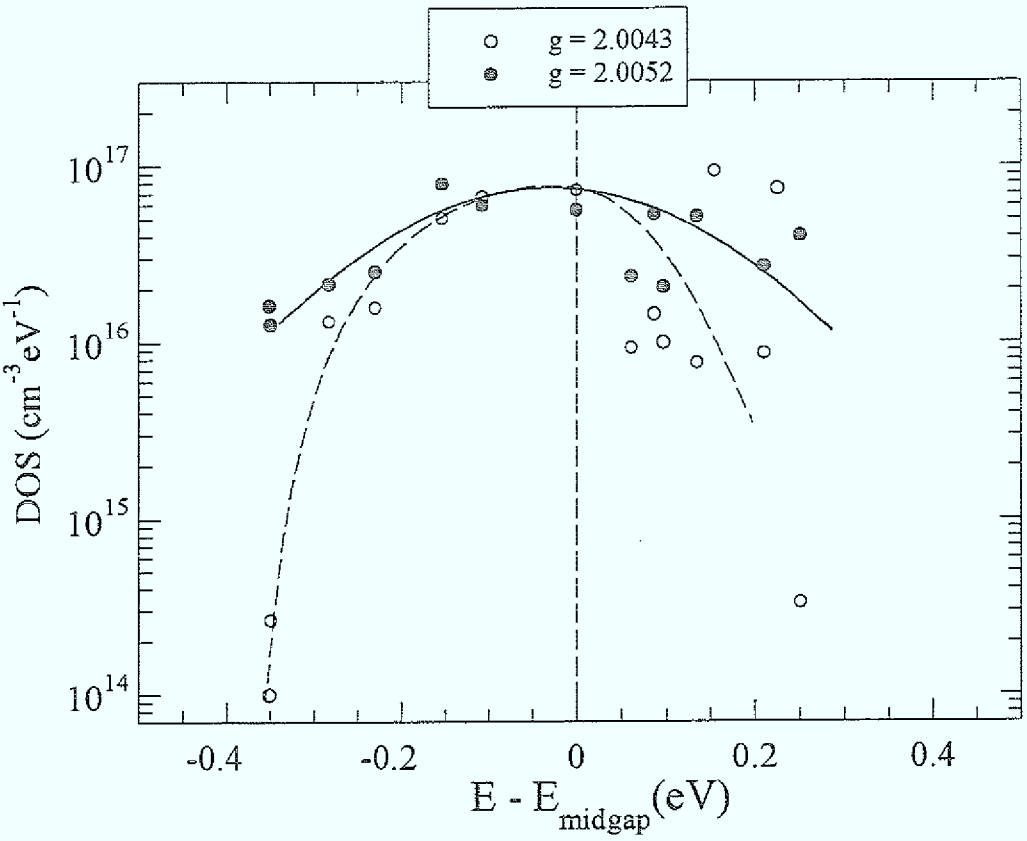

Figure 5.6: Estimated density of states distribution for defects in μc-Si:H as a function of their energy position relative to midgap ($E = 0$). The midgap position was defined as the energy of the compensated sample p1.

experiments on samples with controlled oxygen content would be necessary.

The apparent wide energy distribution of the defects, in particular the defects with g = 2.0052, is probably indicative of the presence of potential fluctuations. This implies that the band-offsets between adjacent regions vary in a random manner throughout the whole material. Such a situation will invariably lead to the existence of singly occupied (and thus paramagnetic) D^0-defect states even for the large Fermi level shifts (by doping) of 0.6 eV. Therefore defect states would be detectable by ESR over a wide doping range, even if the energy distribution of the individual defect within its specific environment was much narrower. Interestingly, in chapter 6 it will be seen that light induced ESR mesurements suggest a different picture for the energy distribution of the defects.

It is emphasized that Fig. 5.6 does not imply that the observed two kinds of defect states have to be located in the same structural environments. In fact, in an inhomogeneous material like microcrystalline silicon defects can be located at boundaries between

columnar grains or individual crystalline domains as well as in rests of the amorphous phase (present for example in the nucleation zone close to the substrate interface as seen in Fig. 2.2(b)). It is likely that a large number of defect states will be found at column boundaries or in amorphous regions rather than at the boundaries between the individual domains, since TEM measurements show that these are highly reconstructed (Houben, 1998, see also Fig. 2.2). The exact location of the defects can, however, not be deduced.

b. Temperature Dependence

The temperature dependence of the signal intensity of both defect state resonances between 40 K and 300 K obeys a Curie-law within the error margins of the experiment and the deconvolution procedure. This means that the integrated signal intensity falls off with 1/T and is equivalent to a constant spin density in this temperature range. The electrons are strongly localized at their defect sites and no changes in the charge state of the defects (number of D^0) occur in the temperature range investigated. Note that again this result is mainly deduced on the basis of measurements on p-type and intrinsic samples as in n-type samples the superposition of three overlapping resonances leads to significant errors in the evaluation of the respective intensities for each individual line.

The observation of a temperature independent spin density for localized dangling bond-like defect states, which can be occupied with zero, one or two electrons, points to a relatively large value for the effective correlation energy U_{eff} (see section 3.3, p. 29) comparable to what is found e. g. for the DB resonance in a-Si:H (Stutzmann, 1987) or polycrystalline silicon (Jousse *et al.*, 1991). The value of $U_{eff} = 0.3$ eV has already been used to calculate the DOS diagram plotted in Fig. 5.6.

5.1.2.2 Linewidth

The linewidths of both defect state resonances in intrinsic and p-type samples almost show no dependence on doping or temperature. In particular, the *temperature* independence suggests that the value of the linewidth is mostly determined by a disorder-induced distribution of g-values without any significant life time broadening of the individual spin packets. Due to the large disorder broadening no indications of the asymmetric powder pattern of dangling-bond like defects with cylindrical symmetry are observed. The result is the measured "average" g-value of a given defect and an almost symmetric resonance line, which can be well approximated by Gaussian functions as was done throughout this work.

5.1.2.3 Summary

- Two kinds of dangling-bond like defect states are identified in microcrystalline silicon which are located in different structural environments. A resonance with a g-value of 2.0052 is due to Si dangling bond states (•Si≡Si), while a line at g = 2.0043 probably originates from dangling bond defects in Si-O-layers due to incorporated oxygen. It

is likely that defects are preferably located along grain-column boundaries or in rests of the amorphous phase, but there is no proof for such an assumption.

- Defect states in μc-Si:H, in particular the resonance at g = 2.0052, are observed over a wide doping range. This is indicative of either a wide distribution in energy (0.6 eV for g = 2.0052) or considerable potential fluctuations throughout the material. The energy distribution is flatter for the DB resonance with g = 2.0052, as the intensity of the line at g = 2.0043 drops by 2 orders of magnitude for the highest p-type doping levels.

- The Curie-like temperature behaviour points to a relatively large effective correlation energy similar to a-Si:H or polycrystalline Si. Using U_{eff} = 0.3 eV the density of defect states within the energy gap of μc-Si:H can be estimated.

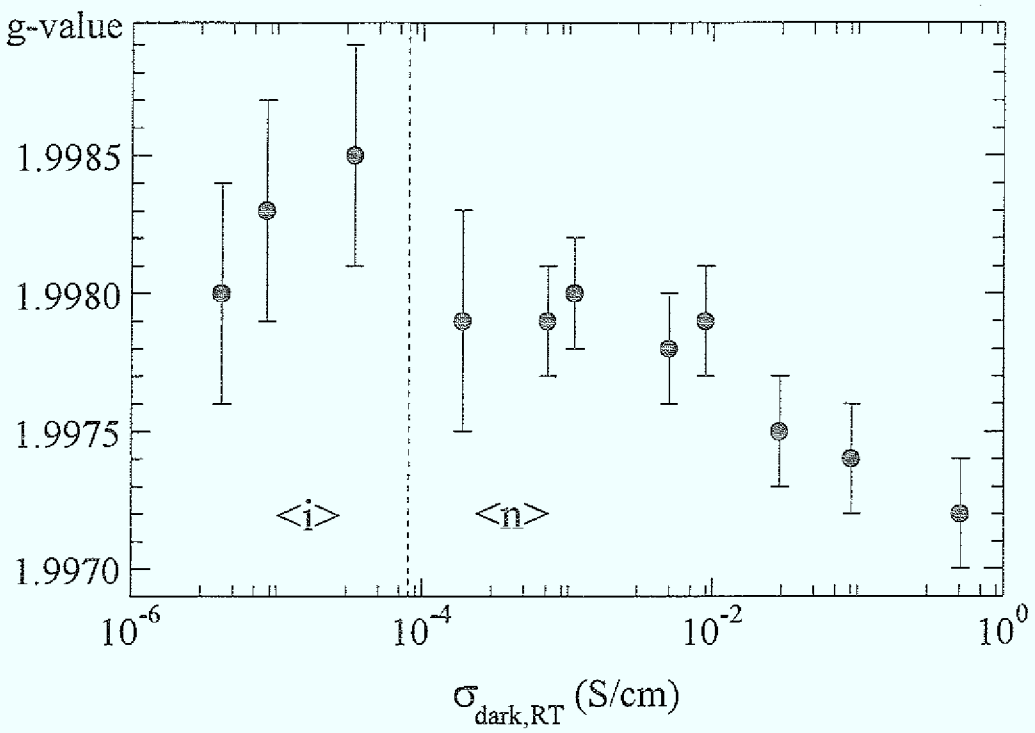

Figure 5.7: CE g-value at 40 K in n-type and intrinsic samples as a function of σ_d^{RT}.

5.1.3 Conduction Electron States

Having outlined the most important facts on the defect states in microcrystalline silicon as they show up in ESR, we will now focus on the third resonance of conduction electrons (CE).

5.1.3.1 g-value

a. Doping Dependence

In Fig. 5.7 the CE g-values (obtained at 40 K) of the microcrystalline silicon samples exhibiting a CE resonance in the dark are plotted versus room temperature dark conductivity. On the left-hand side three intrinsic samples (i13, i50, i115) are included in addition to the n-type samples on the right, where a CE line always was visible[2]. For the n-type samples the CE g-value is between 1.9980 and 1.9972. The lowest g-value of g = 1.9972 is obtained for sample n133 with the highest doping level, whereas the <i>- samples have g-values of 1.9980–1.9985.

[2]Note that the intrinsic samples were prepared at different plasma excitation frequencies and the resulting structural variations (Luysberg *et al.*, 1997) might have some influence on the CE g-values.

The experimental error, indicated by the error bars in Fig. 5.7, was determined as follows: As already mentioned, a Lorentzian simulates the observed CE lines very well in the samples with higher doping levels, whereas the agreement is poorer for lower doping (see section 5.1.1, p. 39). Furthermore in the more heavily doped samples the CE resonance is larger than the defect resonances by 1 or 2 orders of magnitude, so that the CE-lineshape appearing in the spectra is not much distorted by the presence of the defect resonances. Therefore the g-values of 1.9972–5 for samples n33, n67 and n133 can be regarded as accurate except for an experimental error in the magnitude of the resonant magnetic field, which accounts for an error in the g-value of about ± 0.0002. For the other samples the additional uncertainty due to the overlap with the defect resonances, the decreasing CE intensity and the fact that the CE line appears to be more asymmetric with decreasing doping level, leads to a larger error between approximately ± 0.0003 and ± 0.0004 depending on the doping level. If one uses an exponentially modified Gaussian lineshape to account for the asymmetry of the line, the g-values obtained are generally lower by 0.0002. Despite of these uncertainties it is obvious from Fig. 5.7 that the g-value of the CE resonance decreases with increasing doping level.

b. Temperature Dependence

In Fig. 5.8 the temperature dependence of the CE g-values is shown for the n-type samples. For better readability error bars are only included for some of the experimental points, but the vertical bars without data markers (in the left part of the figure) represent the error margins for the respective samples at $T < 100$ K. In addition to the doping dependence of Fig. 5.7, Fig. 5.8 exhibits a weak temperature dependence of the g-values, in particular for the samples with the highest doping levels. For these samples the g-values decrease slightly with rising temperature.

c. Comparison with Similar Material Systems

The CE g-value in μc-Si:H shows a decrease with doping and, in case of the more heavily doped samples, with temperature (Figs. 5.7 and 5.8). At $T = 40$ K it varies in the range $1.9972 < g < 1.9985$. First some similarities and differences with the g-values reported for crystalline silicon will be outlined.

For temperatures well below room temperature the reported g-values measured in phosphorus doped crystalline silicon with donor concentrations not larger than several times 10^{18} cm^{-3} are generally in the range $1.9985 < g < 1.9995$ (Kodera, 1964, 1966, 1969; Stesmans and De Vos, 1986; Feher, 1959; Young *et al.*, 1997b). As already discussed some care has to be taken, since the assignment of the lines and the distinction between localized donor electrons and delocalized CB electrons is sometimes unclear. The value of $g = 1.9995 \pm 0.0001$ has only recently been reported by Young *et al.* (1997b) and is an accurate measurement of the g-value of delocalized electrons in the conduction band. The same value was observed at $T = 3.5$ K, 125 K and 150 K independent of temperature or doping level. The slight decrease of the g-value with rising temperature and increasing doping level as seen in Figs. 5.7 and 5.8 is similar to the results of Kodera (1964, 1966,

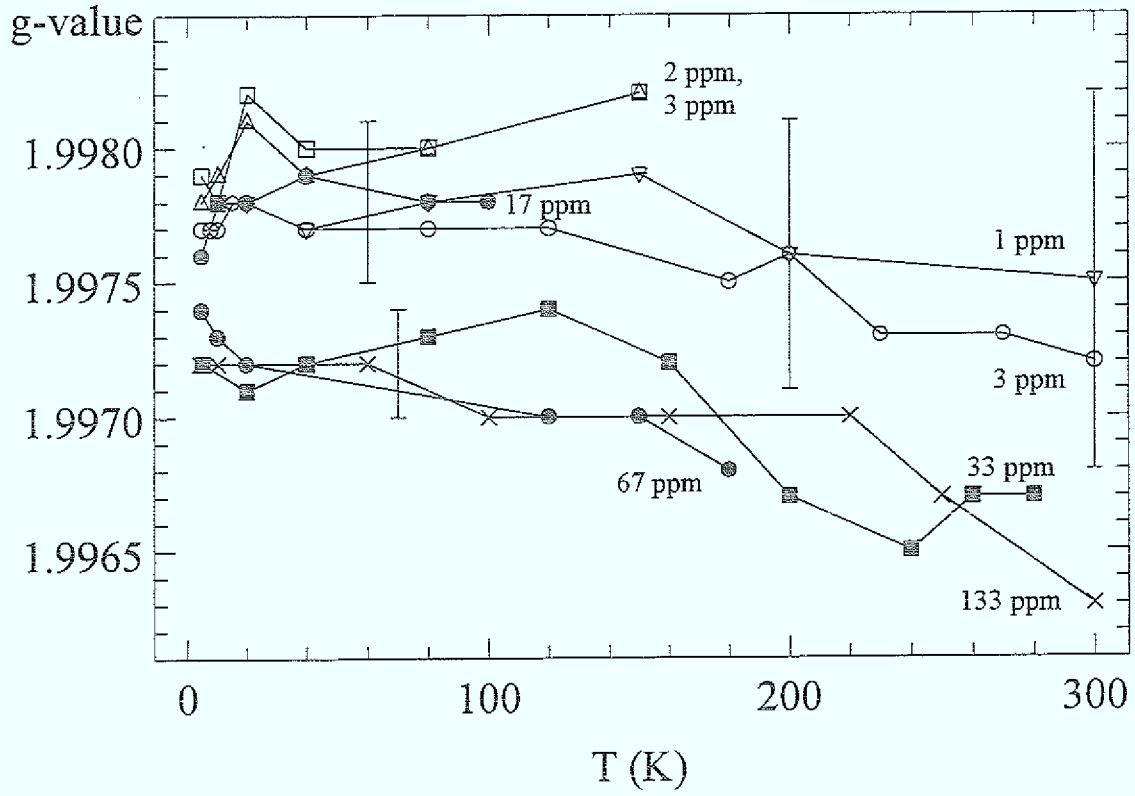

Figure 5.8: CE g-values in n-type samples as a function of temperature.

1969) and Stesmans and De Vos (1986), but no temperature dependence is observed in the data of Young *et al.* (1997b) on CB electrons.

Other similar material systems are polycrystalline silicon and porous silicon. In phosphorus-doped CVD amorphous silicon crystallized by annealing to 700–750°C g-values of conduction electrons between 1.997 and 1.999 were reported by Hasegawa *et al.* (1979). The linewidths are much larger than in c-Si and of similar magnitude as our data on μc-Si:H (see section 5.1.3.2). Young *et al.* (1997b) find the same g-value as in c-Si of g = 1.9995 both in n- and p-type porous silicon and attribute it to conduction band electrons in silicon microcrystals. Others (von Bardeleben *et al.*, 1993) observe ESR signals of optically excited free electrons in what they call quantum confined Si nanostructures with orientation-dependent g-values of $g_\perp = 1.9991$ and $g_{||} = 1.9986$.

Besides the present work ESR measurements on conduction electrons in microcrystalline silicon have also been reported in literature. The obtained g-values are 1.997 in phosphorus-doped (Hasegawa *et al.*, 1983a,b), 1.9983 in nitrogen-doped (Ehara, 1997)

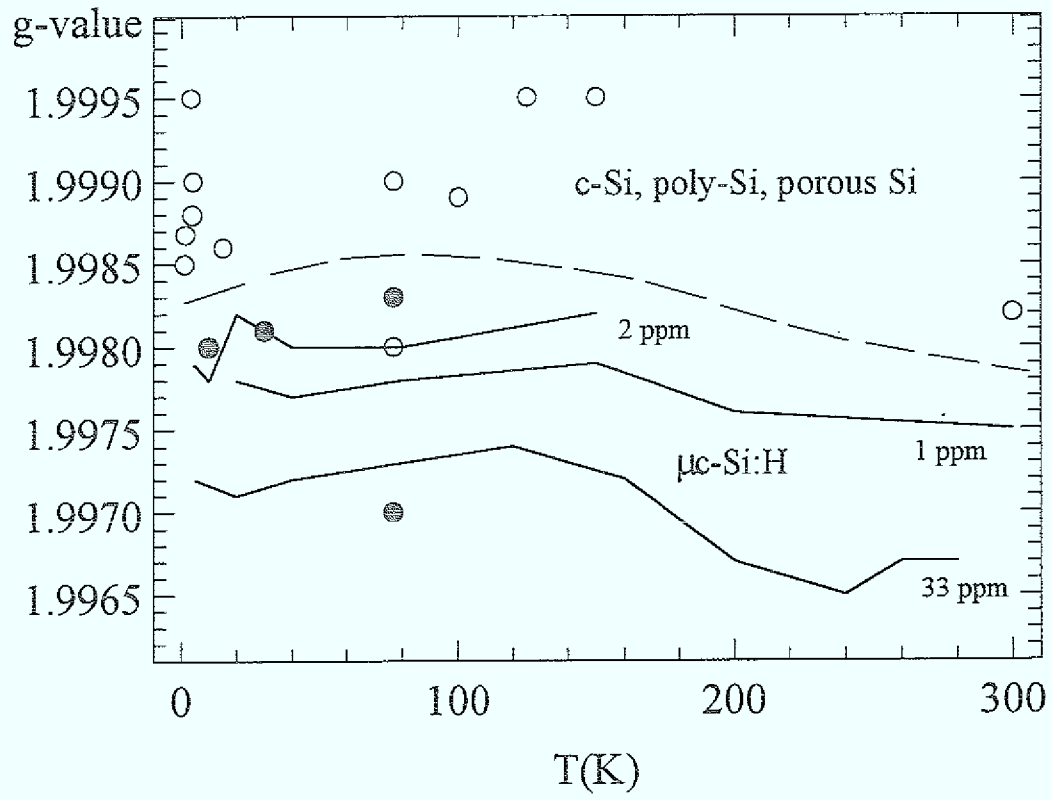

Figure 5.9: CE g-values of μc-Si:H samples n1, n2 and n33 of this work (solid lines) as compared to literature data on microcrystalline silicon (solid circles) and c-Si, poly-Si and porous Si (open circles) as a function of temperature. The dashed line is only included for illustrative purposes and indicates the difference between g-values in μc-Si:H and the other materials. The corresponding references are cited in the text.

and 1.9981 in intrinsic μc-Si:H samples annealed to 400°C (Lips *et al.*, 1998). Kondo *et al.* (1998) observe a signal at g = 1.998 in intrinsic microcrystalline silicon under light illumination and attribute this signal to a trapped electron in a shallow conduction band state of the Si crystallites.

For a better overview Fig. 5.9 illustrates the g-values observed in the various materials. The open symbols denote g-values cited for c-Si, poly-Si and porous Si, closed symbols are literature data of μc-Si:H. The solid lines represent the microcrystalline samples n1, n2 and n33 of this work and are taken from Fig. 5.8.

Evidently the g-values of the CE resonance in μc-Si:H are generally lower than what is reported for crystalline silicon. The largest deviation occurs from the g-value of electrons in the silicon conduction band as given by Young *et al.* (1997b).

d. Summary

- The CE g-values ($1.9972 < g < 1.9985$) observed in μc-Si:H decrease slightly both with temperature and doping level.
- The CE g-values of the μc-Si:H samples used in this work agree with literature data available for microcrystalline silicon. However, they are generally *lower* than in crystalline, polycrystalline and porous silicon.

5.1.3.2 Linewidth

It has been mentioned in section 5.1.2.2, p. 48 that the linewidths of both defect resonances do not exhibit any remarkable temperature or doping dependence. The situation for the conduction electron resonance is strikingly different.

In Fig. 5.10 the peak-to-peak linewidths ΔH_{pp} of three n-type samples with doping levels of 1,3 and 133 ppm are plotted as a function of temperature between 4.5 K and 300 K. These three samples have been picked out as they nicely demonstrate the dependence of the linewidth on both temperature and doping.

The errors in determining the linewidth are larger at high T as background contributions increasingly disturb the spectra, the baseline is not flat anymore and there is some arbitrariness in subtracting (or not subtracting) a background function prior to the numerical integration. Naturally the uncertainties are more significant in samples with lower doping levels and thus less CE intensity relative to the defect state resonances. For better readability error bars are only included at some of the points.

Three important results are obtained from Fig. 5.10: (a) the linewidth of all samples strongly increases with temperature between 40 K and 300 K, (b) the linewidth also increases with doping which is most obvious in the intermediate temperature range, and (c) in samples with higher doping levels (i. e. in sample n133, as shown in Fig. 5.10, and in samples n67 and n33) the linewidth goes through a minimum around T = 30 K and increases again for lower temperatures. The minimum is more pronounced the higher the doping level, but does not appear in material with lower phosphorus concentration. In these samples ΔH_{pp} flattens around T = 30 K, but appears to decrease further for lower T.

a. Temperature Dependence

It has been proposed earlier (Finger *et al.*, 1994b) that the broadening (and, in that work, disappearance) of the CE line is due to lifetime broadening of the resonance as a result of the decrease in spin-lattice relaxation time T_1. Malten *et al.* (1997) measured T_1 for sample n17 for 5 K < T < 80 K. Their results are reproduced in Fig. 5.11 including one point obtained for sample n1. To obtain values for the temperature dependent linewidth directly from T_1 we make use of the fact that for dilute spin systems[3] the spin-spin relaxation time

[3]With an atom density of $4.84 \cdot 10^{22}$ 1/cm^3 the spin system can still be regarded as dilute even for the highest CE spin densities of about $2 \cdot 10^{18}$ 1/cm^3.

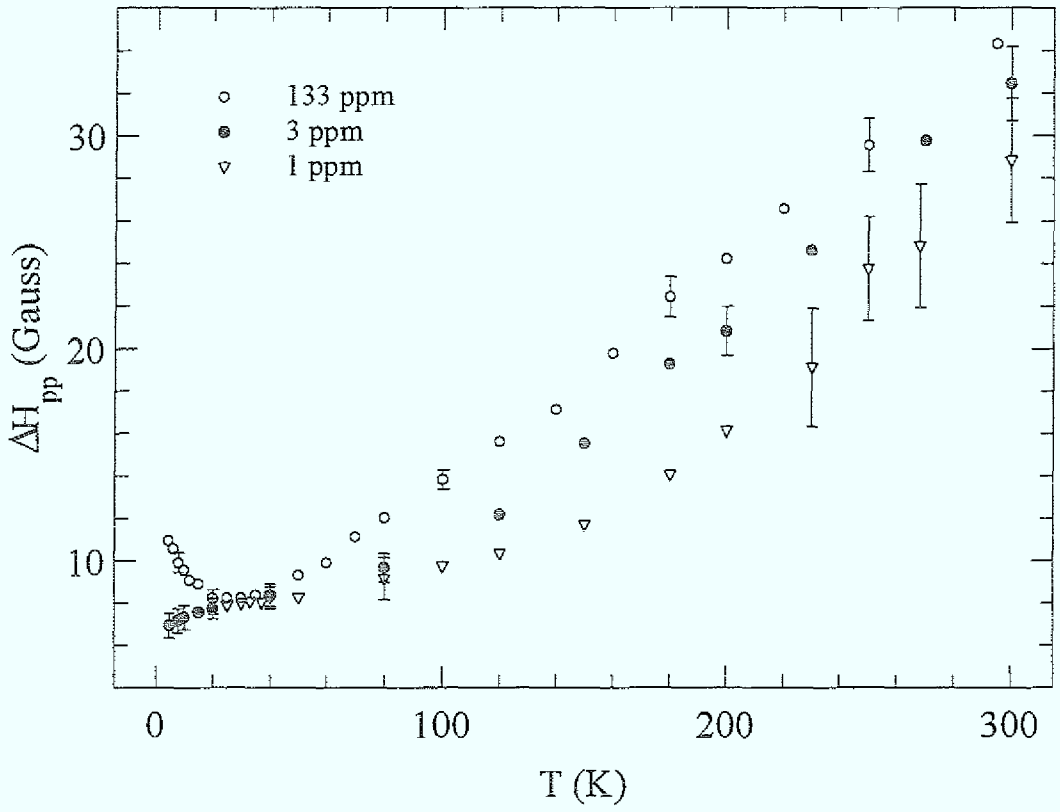

Figure 5.10: Temperature dependence of CE linewidth for samples n1, n3 and n133 between 4.5 and 300 K. For better readability error bars are only included for some of the points.

T_2 will be large but limited by T_1, which acts as an average lifetime of the spin states (Stutzmann, 1983). We can therefore approximate $T_1 = \frac{1}{2}T_2$ (see 3.1.3.1, p. 19 and 3.1.4, p. 21) and obtain from Eq. 3.13

$$\Delta H = \frac{2}{\gamma T_2} = \frac{1}{\gamma T_1} = 5.7 \cdot 10^{-8}\,\mathrm{Gs} \cdot \frac{1}{T_1} \tag{5.1}$$

As we only intend to make a crude estimation the difference between $\Delta H_{1/2}$ and ΔH_{pp} was neglected for simplicity. According to Eq. 5.1 a linewidth of 35 G, which is the value we obtain for sample n133 at room temperature, would require a spin-lattice relaxation time of $T_1 = 1.6 \cdot 10^{-9}$ s. This value seems reasonable in view of the steep decrease of T_1 with temperature and extrapolating the T_1-data of Fig. 5.11 to T = 300 K. Therefore it is concluded that the rapid line broadening of the CE line at temperatures well above the observed minimum can be attributed to lifetime broadening as a result of the decreasing spin-lattice relaxation time.

A steady increase in linewidth for temperatures between liquid helium and room temperature has also been found in the earliest ESR studies on conduction electrons

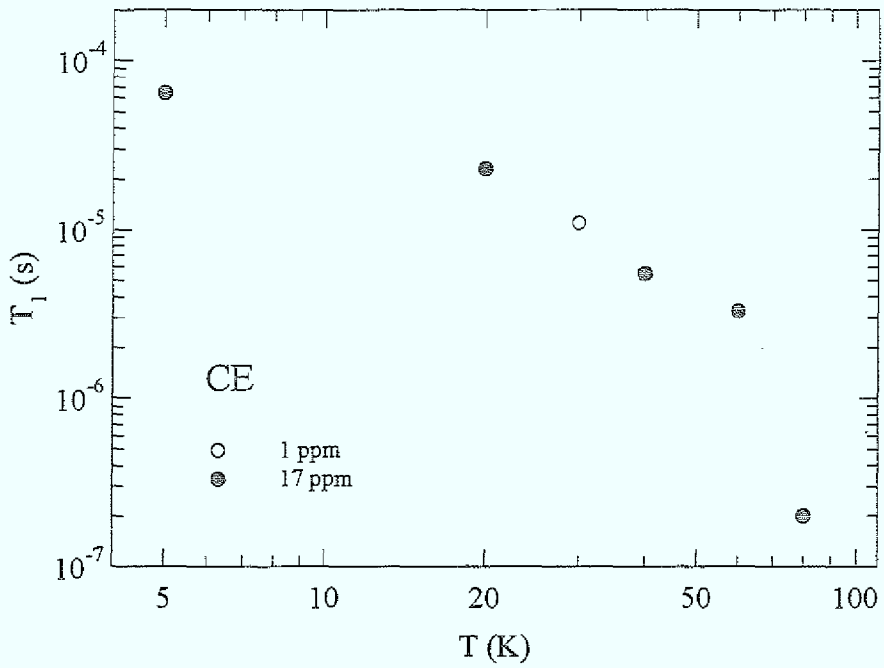

Figure 5.11: Temperature dependence of T_1 for the CE line for samples n1 (open circle) and n17 (closed circles). The data are taken from Malten *et al.* (1997).

in silicon by Portis *et al.* (1953) for a sample with a donor concentration of N_D = 1–2·10^{18} cm^{-3} and later by various other authors for $N_D = 3.5 \cdot 10^{18} - 1.6 \cdot 10^{19}$ cm^{-3} (Kodera, 1969) or $N_D = 5.9 \cdot 10^{18}$ cm^{-3} (Quirt and Marko, 1973). Furthermore, for phosphorus doped c-Si samples with lower doping levels (by several orders of magnitude) Lépine (1970) and Young *et al.* (1997b) report a similar rapid increase in linewidth above 150 K and 200 K, respectively.

At low temperatures the linewidth is not expected to be determined by T_1. This is checked easily as a T_1-value of $2 \cdot 10^{-5}$ s obtained from Fig. 5.11 for T = 20 K would lead to a linewidth of only 3 mG, too low by many orders of magnitude than what is observed in microcrystalline silicon. At low T the linewidth is probably mainly determined by the disordered nature of the microcrystalline material which results in a broad distribution of g-values (and thus resonance frequencies) leading to a large linewidth. In addition unresolved hyperfine interaction and rapid variations in the local hyperfine fields (see section 5.1.3.3) will play an important role. However, there also has to be a mechanism influencing ΔH_{pp} which strongly depends on the spin density of the conduction electrons. This is reflected by the different behaviour of samples with high and low doping levels, respectively, as shown in Fig. 5.10.

b. Minimum

The appearance of a minimum in the temperature dependence of the linewidth has also been reported for crystalline silicon in samples with donor concentrations N_D of less than $3.5 \cdot 10^{18}$ cm^{-3} (Ue and Maekawa, 1971; Quirt and Marko, 1973; Lancaster *et al.*, 1964; Stesmans and De Vos, 1986). This minimum is mostly[4] explained by motional or exchange narrowing of the resonances (section 3.1.4, p. 22), which becomes less effective with decreasing temperature. For the occurence of the minimum in our ΔH-vs.-T data on microcrystalline silicon the presence of motional or exchange averaging might also play a role. It is possible that in a certain temperature region above 30 K, where a large fraction of the electrons is still located at donor sites or in conduction band tail states[5], such narrowing effects lead to a somewhat smaller linewidth than would be obtained without them. As one goes to very low temperatures, the motional/exchange narrowing effect becomes weaker with decreasing temperature resulting in an overall increase in linewidth as the temperature is lowered and leading to the observed minimum.

In samples with lower CE spin densities the distance between interacting spins becomes too large to allow for effective exchange interaction, and hence no minimum occurs in lightly doped samples. This can be checked by calculating the average distance r_D between the electrons contributing to the CE line by the expression $r_D = (4\pi/3 \cdot N_s)^{-1/3}$ where $N_s = N_s(CE)$ is the observed CE spin density. This leads to values r_D of 65 Å, 52 Å and 48 Å for samples n33, n67 and n133, respectively. On the other hand, for sample n1 with a spin density which is about a factor of 100 smaller than in sample n133, r_D = 193 Å and is too large for exchange averaging to be expected.

c. Doping Dependence

The increase of linewidth with doping is most obvious in the intermediate temperature range, i. e. in the region where lifetime broadening via a strongly increasing spin-lattice relaxation time can be held responsible for the broadening of the CE line. Thus one reason for the larger linewidth in more heavily doped samples could be a shorter T_1 compared to samples with lower doping levels. As pulsed ESR data were not available for all samples, saturation experiments using the conventional continuous wave technique were performed to get a rough idea of the spin-lattice relaxation times. This was done for both p- and n-type samples at temperatures between 10 K and 40 K. Although a quantitative evaluation is difficult and unreliable, the saturation curves show that the CE signal tends to saturate the earlier (i. e. at lower microwave power) the lower the doping level. If this result is extrapolated to the intermediate temperature region it can explain the larger CE linewidth in more heavily doped material.

An increase in linewidth with doping has also been found in early studies on heavily doped microcrystalline silicon (Hasegawa *et al.*, 1983b) at liquid nitrogen temperature. However, in that work the lowest gas phase doping ratio was 1000 ppm

[4]Lancaster *et al.* (1964) give a different explanation for their data.

[5]This will become clear in the following sections.

($N_s(CE) = 3 \cdot 10^{19}$ cm^{-3}) and thus about a factor of 8 above our maximum doping.

d. Summary

- A strong increase in CE linewidth with temperature above T $\approx$ 30 K is attributed to lifetime broadening as a result of a decrease in spin-lattice relaxation time T_1, which is confirmed by pulsed ESR data.
- Around T = 30 K a minimum in ΔH_{pp} is found for high doping levels, which is possibly due to incomplete exchange narrowing at the lowest temperatures.
- In the intermediate temperature region (100 K < T < 300 K) ΔH_{pp} increases with doping as a result of the doping dependence of T_1 (spin-lattice relaxation is slower at lower doping levels).

5.1.3.3 Hyperfine Interaction

In a material where the paramagnetic electrons interact with their own or neighbouring nuclei one can hope to gain very specific and microscopic information about the material. This has been made use of extensively in the past in crystalline silicon (see also section 3.1.2), e. g. for the electrons located at phosphorus donor atoms, and more recently has also given valuable insights when applied to amorphous silicon (Biegelsen and Stutzmann, 1986; Stutzmann *et al.*, 1987; Stutzmann and Biegelsen, 1988).

An electron located at a phosphorus dopant atom in a P_4^0-configuration will in its ground state interact with the nucleus giving rise to a hyperfine splitting into two states with different energies. Therefore a single resonance line will split into a line doublet. In crystalline silicon this splitting has already been observed in the earliest measurements (Fletcher *et al.*, 1954b) and a hyperfine splitting (i. e. a separation of the respective resonance lines) of $\Delta HFS = 42$ G was found at liquid helium temperature. The observability of this hyperfine splitting strongly depends on the donor concentration and on the measurement temperature as briefly described in section 3.1.2 (see also Morooka *et al.*, 1994, for a recent work), whereas the value of the splitting does not change much (Cullis and Marko, 1975).

a. Observability

Before proceeding with hyperfine results in n-type microcrystalline silicon it is therefore advisable to get an idea about the conditions (temperature, dopant concentration) under which one might be able to observe hf interaction at all. Therefore an overview of literature data in crystalline silicon where hyperfine structure was observed is given in Table 5.1. For better illustration the data compiled there are plotted in Fig. 5.12, including the CE spin density range of our samples ($3.3 \cdot 10^{16}$cm^{-3} < $N_s(CE)$ < $2.4 \cdot 10^{18}$cm^{-3}) and the temperature range accessible (4.2 K < T < 300 K).

#	Reference	T (K)	P concentration N_D (cm^{-3})
1	Fletcher *et al.* (1954a)	4.2	$4 \cdot 10^{17}$
2	Fletcher *et al.* (1954b)	4.2	$1 \cdot 10^{17}$
3	Feher and Kip (1955)	1.2	$1 - 4 \cdot 10^{17}$
4	Feher and Gere (1959)	1.2	$1.5 \cdot 10^{16}$
5	Jérome and Winter (1964)	1.3	$8 \cdot 10^{16}$
6	Maekawa and Kinoshita (1965)	4.2	$< 7 \cdot 10^{17}$
7	Kodera (1969)	4.2	$2.9 \cdot 10^{17}$
8	Morigaki and Maekawa (1972)	4.2	$2.5 \cdot 10^{17}$
9	Cullis and Marko (1975)	< 10 < 35	$< 1 \cdot 10^{18}$ $< 1.2 \cdot 10^{17}$
10	Lépine (1970)	20 – 40	$7.5 \cdot 10^{14} - 8 \cdot 10^{16}$
11	Paalanen *et al.* (1986)	0.2	$\approx 3 \cdot 10^{18}$
12	Morooka *et al.* (1994)	< 19	$1.3 \cdot 10^{17}$

Table 5.1: Overview of measurement and doping conditions under which hyperfine interaction in P-doped crystalline silicon was observed.

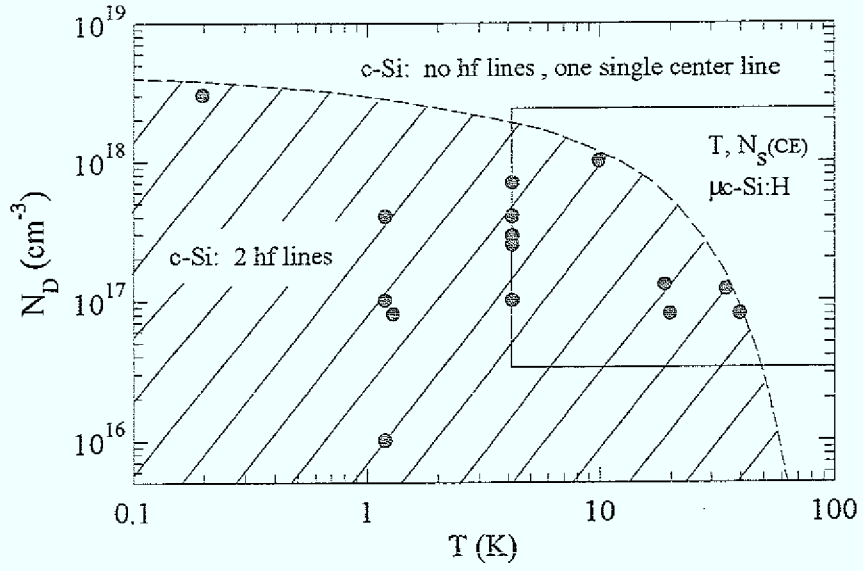

Figure 5.12: Overview of measurement and doping conditions under which hyperfine interaction in P-doped crystalline silicon was observed. The rectangular area on right-hand side marks the doping and temperature range accessible in the present study. The circles represent the data of Table 5.1 further illustrated by the shaded area which describes the region of low doping and low temperature where two hf lines are observed in crystalline silicon.

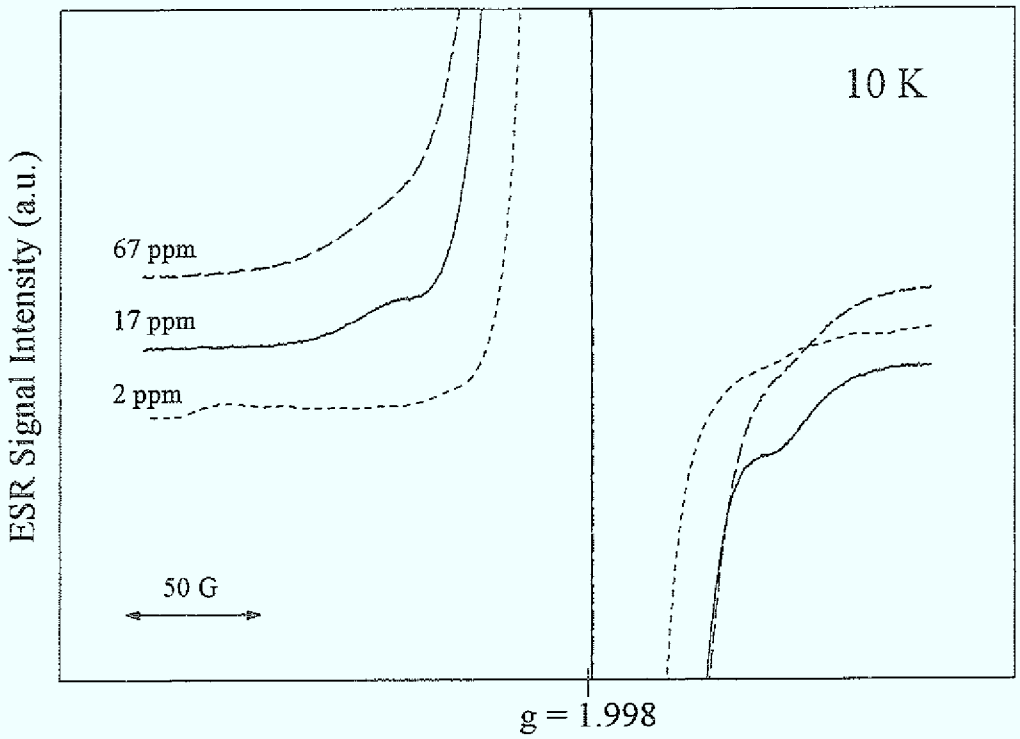

Figure 5.13: Spectra of samples n2, n17 and n67 obtained at T = 10 K, high receiver gain and large modulation amplitude. Hyperfine interaction of donor electrons with ^{31}P is clearly visible only for a doping level of 17 ppm.

In summary hf interaction is easiest observable in samples with *low* dopant concentration at *low* temperatures. Therefore (see Fig. 5.12) it should be expected that the hyperfine doublet of ^{31}P will be found in μc-Si:H at the lowest temperatures for low doping levels. Interestingly enough, this is not the case. However, hf interaction *can* be measured in phosphorus-doped microcrystalline material which will be shown in the following.

b. Hyperfine Splitting

Fig. 5.13 shows ESR spectra of three microcrystalline silicon samples with different doping levels obtained at a temperature of 10 K. Here a magnetic field modulation amplitude of 14 G was used, the scan width was 300 Gauss and the g-value of the broad line is approximately 1.998 on this scale[6]. To obtain maximum sensitivity for weak resonances a very high value for the receiver gain of the spectrometer was chosen so that the main central part of the line could not be recorded. Even with this procedure only sample n17 with intermediate doping exhibits clearly distinguishable broad shoulders in the wings of the

[6]The spectra are not normalized and thus the apparently large difference in linewidth only reflects the different CE signal intensities of the three samples.

central line which can be identified as the expected hyperfine doublet of ^{31}P. Traces of these shoulders are still observable in sample n67 ($N_s = 1.7 \cdot 10^{18}$ cm^{-3}), but surprisingly there is no indication of hyperfine interaction for the 2 ppm sample with $N_s = 7.7 \cdot 10^{16}$ cm^{-3}, well in the doping range where the ^{31}P hyperfine doublet is the prominent feature in crystalline silicon. Note that the flat shoulders in the 2 ppm spectrum are simply caused by signal noise and background contributions.

Certainly in the lightly doped samples observation of the hf doublet is complicated by the additional contributions of defect states (that cannot be totally saturated 'away' even at high power levels), which have a similar spin density as the CE line. Also the CE intensity is much smaller in those samples, so that one has to use much higher receiver gains. This results in very strong background contributions and a highly distorted baseline, which might render a distinction between a hyperfine signal of several percent intensity and the background impossible. However, in crystalline silicon at low temperatures and low doping levels the hf lines clearly dominate the spectrum, which is definitely not the case in our samples.

c. Localization Length

Possible reasons for this striking difference between μc-Si:H and c-Si will be discussed shortly, but first a closer look at the hyperfine interaction in sample n17 is necessary. To accomplish this, a spectrum similar to the one in Fig. 5.13 of sample n17 is plotted in Fig. 5.14, this time taken at T = 20 K where the hf shoulders appeared to be even easier to distinguish. The central derivative curve (dashed line) represents the Lorentzian-shaped ESR spectrum of the CE resonance, whereas the solid line corresponds to a magnification of the line by a factor of 100 and exhibits clearly the hyperfine structure already described in Fig. 5.13. The intensity of the hyperfine doublet at 20 K is only between 2% and 5% of the overall signal intensity, the spread being due to the uncertainty in data analysis. The hyperfine splitting (ΔHFS), i. e. the separation of both hf lines, can be estimated as shown in the figure. The result is $\Delta HFS = 110$ G, which is between the values of 42 G reported for crystalline Si and 245 G for amorphous silicon (Stutzmann, 1987). The same value is obtained for sample n17 with pulsed ESR employing electron spin echo detected field sweep (Malten *et al.*, 1997).

From $\Delta HFS = 110$ G one can estimate the effective Bohr radius of the phosphorus impurities in μc-Si:H following the procedure given by Stutzmann (1987) for amorphous silicon. In terms of the hyperfine splitting ΔHFS the isotropic hyperfine interaction A_{iso} can be expressed as $A_{iso} = g\mu_B \Delta HFS$. Using Eq. 3.5 on page 16 this yields

$$|\psi(0)|^2 \propto \Delta HFS \tag{5.2}$$

For the effective Bohr radius a_0 of the donor electron wave function the following relation holds:

$$a_0 \propto \left(|\psi(0)|^2\right)^{-\frac{1}{3}} \tag{5.3}$$

Therefore one can directly correlate the values of the hyperfine splittings in μc-Si:H and

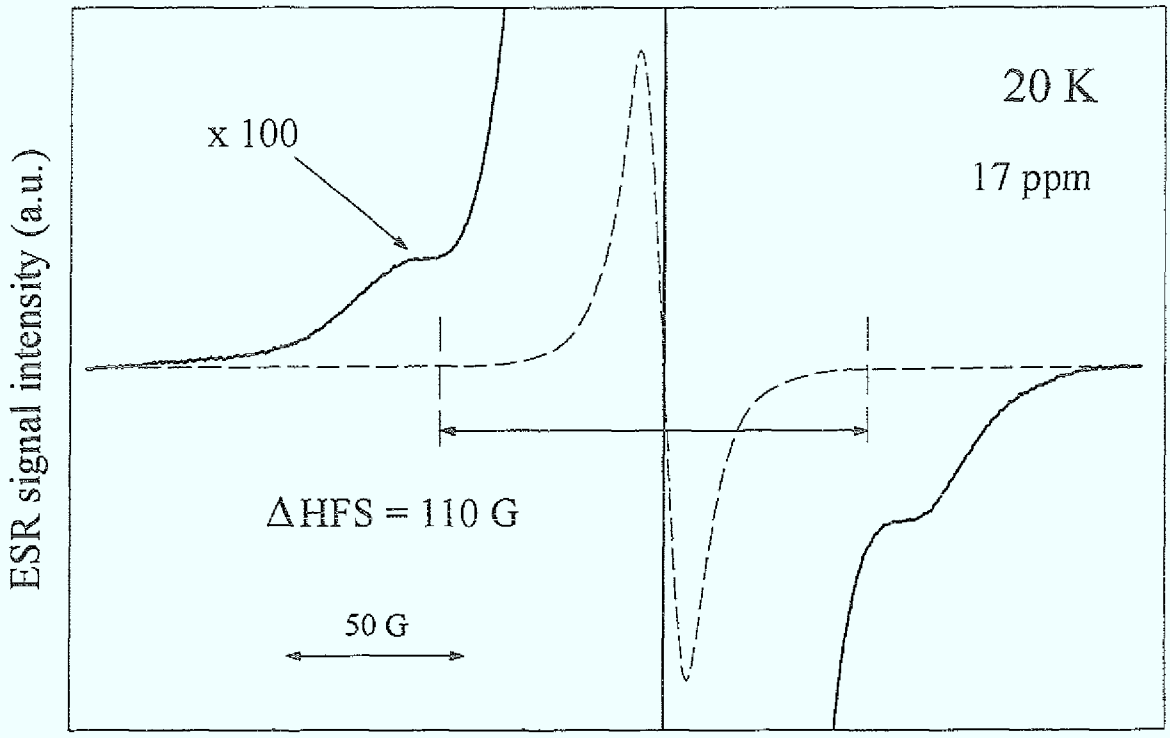

Figure 5.14: Hyperfine splitting in sample n17 exhibiting a value for ΔHFS of 110 G. The dashed curve is the Lorentzian-type CE line and the solid curve is the same line magnified by a factor of 100.

crystalline silicon (c-Si) with their effective Bohr radii:

$$\frac{|\psi(0)|^2(\text{c-Si})}{|\psi(0)|^2(\mu\text{c-Si:H})} = \frac{\Delta HFS(\text{c-Si})}{\Delta HFS(\mu\text{c-Si:H})} = \frac{42\text{G}}{110\text{G}} = \frac{a_0(\mu\text{c-Si:H})^3}{a_0(\text{c-Si})^3} \tag{5.4}$$

Using the value of $a_0 = 16.7$ Å in c-Si (Stutzmann *et al.*, 1987) we obtain $a_0 \approx 12$ Å for μc-Si:H. In amorphous silicon one finds $a_0 = 10$ Å. Thus the electrons bound in the assumably s-like donor ground state in microcrystalline silicon are stronger localized at the nucleus than in crystalline material, but the localization is weaker than in amorphous silicon.

Stutzmann *et al.* (1987) give in Fig. 15 a relation between localization length and defect binding energy (i. e. energy position below the conduction band) for various paramagnetic defects in amorphous and crystalline silicon and germanium. Applying this relation to μc-Si:H a value of $a_0 = 12$ Å would put the corresponding state 90 meV below the conduction band edge. An ionization energy of 70 meV is obtained from an empirical relation between the g-values of donor electrons and their respective binding

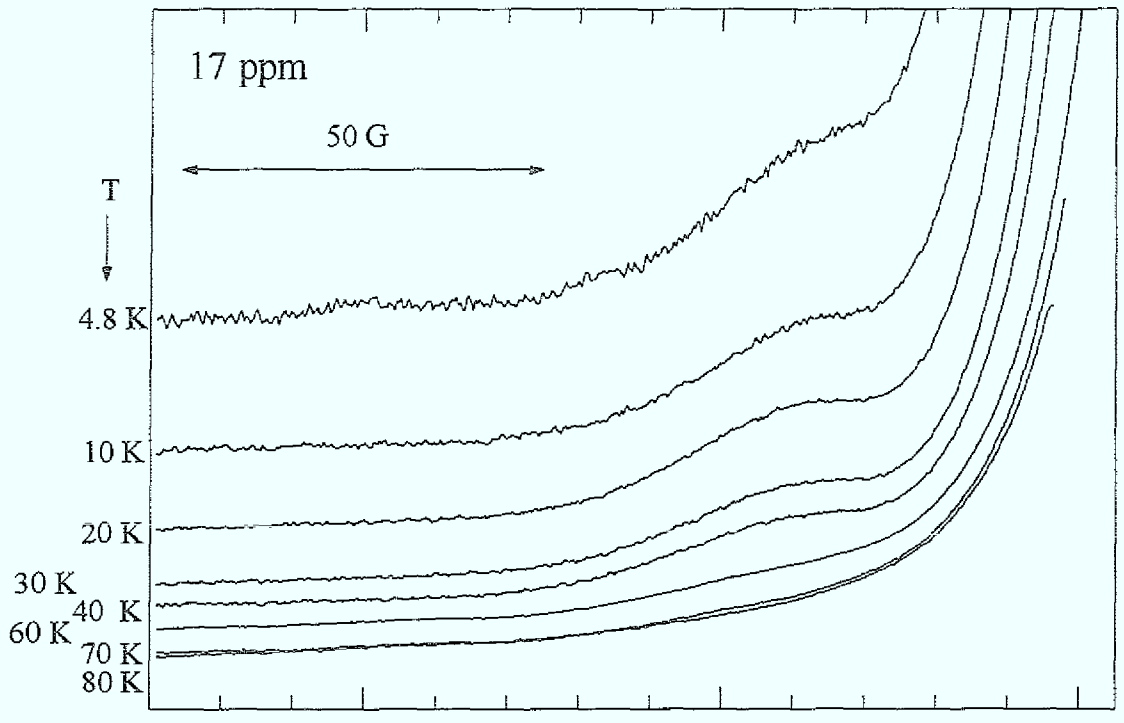

Figure 5.15: Temperature dependence of the ^{31}P hyperfine doublet in sample n17 between 4.8 K and 80 K. The respective temperatures are displayed on the left-hand side of the figure. For better comparison only the left-hand side of the hf doublet is shown in a magnified view.

energies given by Young *et al.* (1997b), Fig. 1, using g = 1.9979 for sample n17. However, it is questionable whether both relations are applicable to the present case. In crystalline silicon the binding energy of phosphorus donors is about 45 meV (Picus *et al.*, 1956).

d. Temperature Dependence

The hf splitting in sample n17 was observed at temperatures between 4.8 K and 70 K. For T > 70 K no traces of the shoulder due to hyperfine interaction were detectable in the spectra any more. This is illustrated in Fig. 5.15 where the shoulder on the low-field side of the CE resonance at various temperatures is shown in a magnified view for better comparison. The gradual disappearance of any observable hyperfine signal is clearly seen. An evaluation of the intensity of the hf-line pair relative to the intensity of the CE center line (which obeys the Curie law in this temperature region) shows a stronger decrease in hf signal intensity than 1/T. Unfortunately an exact quantitative analysis (such as to check for an activated behaviour with a certain activation energy which might be compared with the value of 90 meV deduced above) is prevented by the weakness of the hf lines compared to the center resonance line.

e. Reasons for Non-Observability of Hyperfine Interaction

So far two important observations have not been commented on: (1) No indications of hyperfine interaction appear in the samples with the lowest doping levels and (2) even in sample n17 — where they are observed — the hyperfine lines only account for less than 5% of the center line intensity even for the lowest temperatures available (4.5 K).

For higher doping levels the non-observability of hf interaction is in accordance with c-Si and was already mentioned in section 3.1.2.2, p. 17. In addition, when analysing low temperature conductivity data for samples with higher doping levels in section 5.2, it will be suggested that transport in μc-Si:H at low T proceeds via hopping between ionized and neutral donor sites. The hopping frequency for this process is of the order of 10^9 s^{-1} thus exceeding T_1 by many orders of magnitude. Such an electron will observe positive and negative values of the hyperfine field successively at a very high rate and the hyperfine interaction will be *effectively averaged to zero.*

Thus the main problem is the non-observation of hf interaction at low doping in contrast to what one expects from the comparison with crystalline silicon data. In the following the possible reasons for this discrepancy will be pointed out and their consequences for the nature and location of the CE states in μc-Si:H will be discussed. This is done under the assumption that the CE line seen in ESR is connected with the phosphorus incorporation into the microcrystalline material, which will be proven in the subsequent section.

In principle there are only two possible explanations why hf interaction does not appear to the same extent as in c-Si: either (i) the majority of the electrons which are seen as CE line in ESR is not located at their phosphorus donors at all or (ii) the electrons are in fact bound to the phosphorus atoms but for some reason no hyperfine interaction can be detected.

(i) In the former case one has to ask where the electrons are actually located if not at the donors. There are various possibilities:

- The major part of the donor electrons could be excited to the conduction band of the crystallites already at low temperatures. To investigate this possibility one can refer to calculations performed by Lépine (1970) for crystalline silicon, assuming the same or at least a similar energy level scheme in microcrystalline silicon. Lépine (1970) calculated the relative fraction of electrons excited into the conduction band for c-Si with similar doping levels at temperatures between 20 K and 300 K. He finds that for temperatures $T < 40$ K only less than 10 % of the donor electrons will have been activated into the CB which rules out the explanation given above.

- Electrons may occupy tail states in the conduction band tails of the silicon crystallites. It has been argued before (section 2.2) that band tailing is expected in a material like μc-Si:H. The energy range below the conduction band of such tail states overlaps with the binding energy of the phosphorus donor electrons (45 meV in c-Si). Thus electron transfer between these localized states is likely to occur. Energetically the occupation of tail states

might be even more favourable for electrons, as tail states also exist at energies smaller than the donor binding energy.

- As frequently observed in polycrystalline silicon (Hasegawa *et al.*, 1979) the excess electrons of incorporated phosphorus donors could be trapped by deep defects (g = 2.0043,2.0052) present in the material. In such a case donors can only provide carriers for the CB and thus become electrically active, if most of the defects are already occupied with electrons. This would mean, however, that the number of neutral (and thus paramagnetic) defects is substantially reduced, in particular at high donor concentrations, in contrast to the observed constant ESR defect density over a wide n-doping range (section 5.1.2). Furthermore, it will be shown in section 5.3 that the number of CE electrons is equal to the number of incorporated donors, which means that the donor electrons have for their major part *not* been trapped by deep defects but contribute to the CE resonance.

(ii) Under the assumption that the CE electrons *are* located at the phosphorus dopants, one could again think of several explanations why no hf interaction is detected:

- An easy explanation would be that hyperfine interaction is in fact present but cannot be detected as the two hyperfine lines are too close together to be separated in view of the rather broad center CE line in microcrystalline silicon. Such an assumption is readily proven impossible as the linewidths at low T are around 8 Gauss for the samples with low donor density and the hyperfine lines are at least 42 G apart, as a lower value (which would mean even less localized donor electrons than in c-Si) is not realistic.

- As was pointed out in section 3.1.2, p. 17, the six-fold degenerate ground state of phosphorus donors in c-Si splits into essentially one singlet state A_1 and 5 closely spaced 1^{st} excited states with an energy separation of 11 meV between A_1 and the excited states. Hyperfine interaction can only occur in the A_1 ground state with non-vanishing amplitude at the site of the nucleus. Thus, if the CE signal arised from electrons in the 1^{st} excited state of phophorus, no hf interaction could be observed. However, Lépine's calculations (Lépine, 1970) show that at temperatures T < 40 K more than 80% of the electrons are expected to be in the ground state A_1 and should thus give hyperfine interaction (which Lépine actually observed). Again this provides no explanation for the vanishing hf structure in microcrystalline silicon.

- In Lépine's study the highest phosphorus concentration was $N_D = 8 \cdot 10^{16}$ cm^{-3} thereby avoiding that donors come close enough to each other to allow for appreciable exchange interaction between donor electrons. The formation of such clusters, whose electronic spins are coupled strongly to each other by exchange, is a well-known fact in phosphorus-doped crystalline silicon and starts at donor concentrations above $6 \cdot 10^{16}$ cm^{-3} (Morigaki and Maekawa, 1972). As was pointed out in section 3.1.2 the cluster formation leads to additional features in between the two resonance lines of one isolated donor and a gradual disappearance of these two lines.
There is no obvious argument why such a clustering should not occur in μc-Si:H and can be regarded as one of the reasons, why — like in c-Si — the hf structure vanishes with

increasing donor concentration and thus increasing formation of clusters of two or more atoms. In particular, any additional hf lines due to the clustering will not be observable due to the disorder-induced line broadening in the microcrystalline material. However, to explain the non-observability of hf structure even in weakly doped samples one would have to assume effective cluster formation or at least dopant pairing already at these low doping levels. Although this is in contrast to crystalline silicon such a possibility cannot be ruled out and has to be kept in mind.

- Finally it is possible that – similar to high doping levels – hopping processes (section 5.3.2.2, p. 79) also take place at the lowest phosphorus concentrations, even though their contribution to the conductivity is too small to be observed. However, the hopping frequencies for such processes estimated from the average inter–donor distance (192 Å for the CE spin density of $3.3 \cdot 10^{16}$ cm^{-3} in sample n1) are quite low and hopping motion would not be rapid enough to lead to the same averaging effect of the hf interaction as in case of higher doping levels.

f. Summary

- In n-type μc-Si:H the hyperfine doublet of ^{31}P is either not observed at all or only present with a very low intensity as compared to the large single CE resonance line. This is true even in samples with dopant concentrations N_D at which the hf line pair is clearly the dominant feature in their crystalline counterpart with the same N_D.
- For the weak hf signal of the intermediately doped sample n17 a hyperfine splitting ΔHFS of 110 G is found which corresponds to a localization length of the donor electron wave function of 12 Å.
- Most likely explanations for the lack of significant hf interaction are occupancy of conduction band tail states instead of donor states, formation of clusters of two or more donor atoms and the effect of averaging out the hf interaction due to rapid hopping motion of electrons between adjacent donor sites. The latter process mainly applies to samples with higher doping levels.

5.1.3.4 Signal Intensity

a. Doping Dependence

It was shown that the ESR behaviour of the CE line significantly depends on the doping level. One ESR parameter which has not been considered so far is the signal intensity or in other words the spin density of the conduction electron signal as a function of doping. This relation will be established now.

Instead of examining the CE spin density $N_s = N_s(CE)$ as a function of doping level one can alternatively plot $N_s(CE)$ (see Fig. 2.1) as a function of σ_d^{RT}. Plotting $N_s(CE)$ versus σ_d^{RT} has the advantage of easily including those nominally undoped samples which also exhibit a CE resonance in the dark. In plotting and interpreting Fig. 5.4 we had

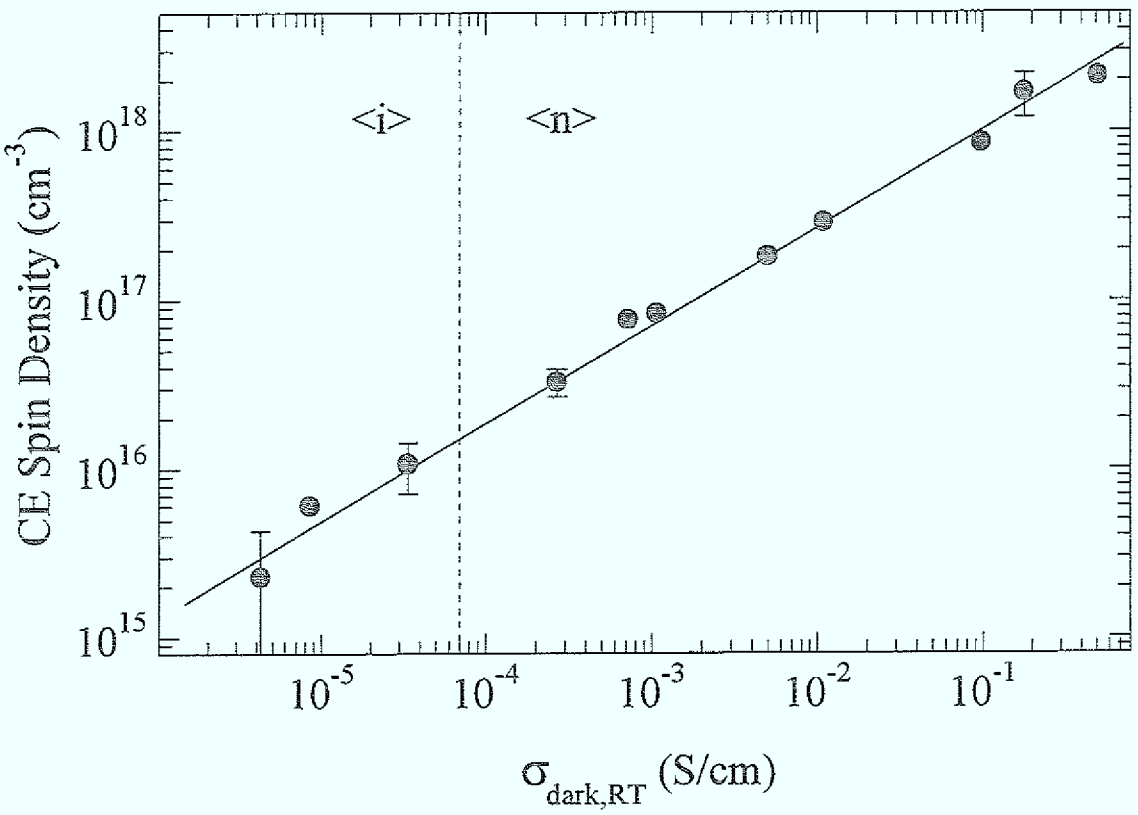

Figure 5.16: CE spin density at 40 K versus σ_d^{RT}. The dashed line separates undoped and n-type samples. The solid line is a guide to the eye.

quietly assumed that the spin density otained at T = 40 K is a reliable measure of N_s. This assumption was confirmed later by observing Curie-like behaviour of the defect states in the temperature range studied. It will be shown shortly that the CE line also obeys the Curie law within experimental errors. Therefore one can safely draw Fig. 5.16 which is a plot of the CE spin densities $N_s(CE)$ of intrinsic (left-hand side) and n-type (right-hand side) samples as a function of room temperature dark conductivity.

A remarkable relation between $N_s(CE)$ and σ_d^{RT} is observed over almost 3 orders of magnitude in $N_s(CE)$ and 5 orders of magnitude in σ_d^{RT}. Since on the other hand σ is related to the gas phase doping ratio acording to Fig. 2.1 (which will in turn influence the phosphorus concentration in the solid), this result also suggests a relation between ESR spin density and the concentration of incorporated phosphorus. In fact, it turns out that both quantities are equal as will be shown in sections 5.2 and 5.3 at the end of this chapter, where the ESR results are related to temperature dependent conductivity measurements.

The different conductivities and the relation between CE spin density and conductivity in nominally undoped samples (left-hand side of Fig. 2.1) can be explained in two ways.

One possibility is that either small amounts of residual phosphorus or other impurities, which can act as n-type dopants, were incorporated during deposition. Their concentration obviously depends on the specific preparation parameters like the plasma excitation frequency. Alternatively, variations in the material structure (which is a function of ν_{ex}) might lead to different occupation of CE states.

The next step is to investigate the temperature dependence of the CE signal intensity.

b. Temperature Dependence

As outlined in section 3.1.3.2,p. 19, the temperature dependence of the magnetic susceptibility (and hence the ESR signal intensity) will provide information about the temperature dependent occupation and the nature of the underlying electronic states. Therefore the intensity of the CE signal was monitored as a function of temperature for various n-type doping levels. The results for 4 differently doped samples (1, 33, 67 and 133 ppm) are summarized in Figs. 5.17 and 5.18.

Fig. 5.17 shows the CE signal intensity of sample n1 between 20 K and room temperature in a double logarithmic plot. For temperatures lower than 20 K saturation of the CE line leads to a decrease in signal intensity, and hence data from that temperature

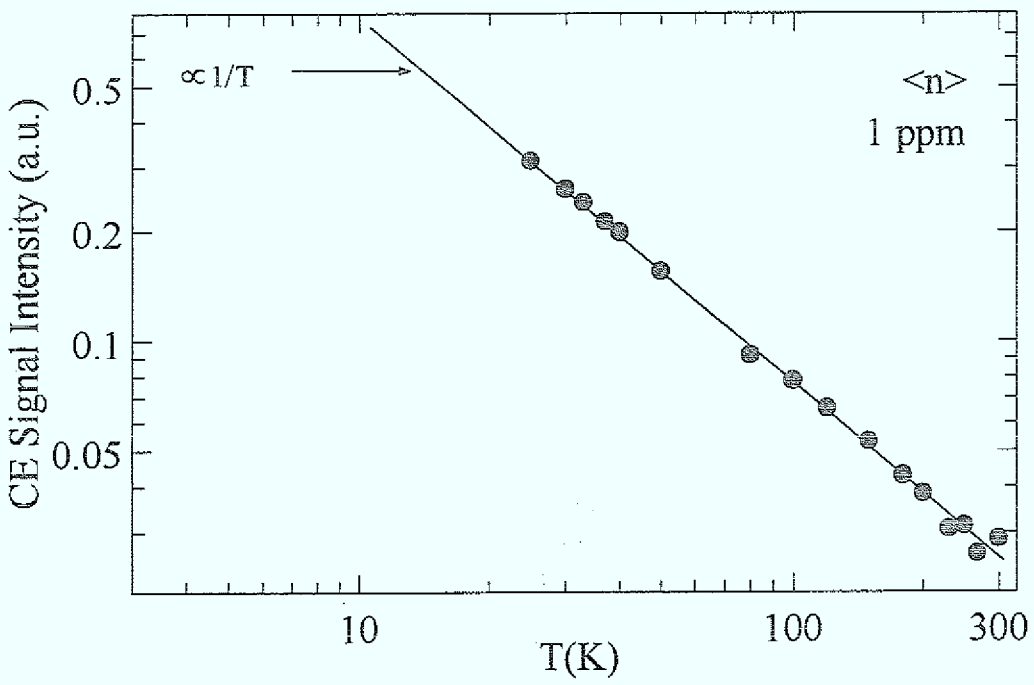

Figure 5.17: Temperature dependence of CE signal intensity for sample n1 between 20 and 300 K in a double logarithmic plot. The line indicates what is expected from the Curie law (intensity $\propto$ 1/T).

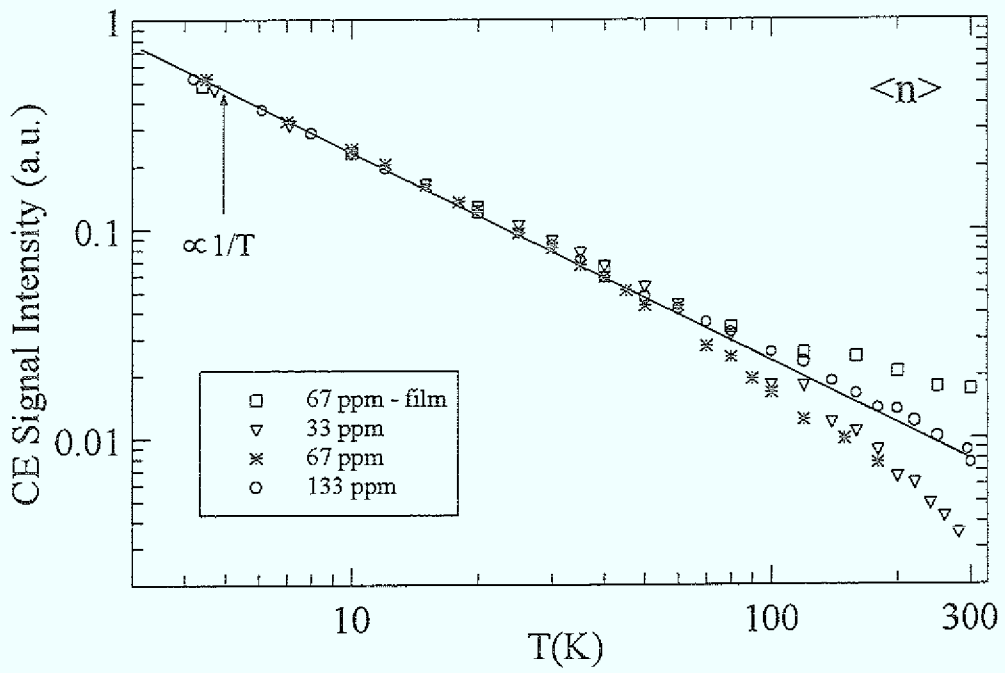

Figure 5.18: Temperature dependence of CE signal intensity for powder samples n33, n67 and n133 and a thin film of n67 between 4.5 K and 300 K. Intensity values for the powder samples have been corrected for changes in Q with varying temperature.

region are not included. The straight line of slope -1 indicates the behaviour expected for paramagnetic states obeying the Curie law (i. e. intensity $\propto 1/T$). The CE intensity nicely follows the 1/T-behaviour in the whole temperature range.

For the samples with higher doping levels observation of the CE line at higher T is complicated by the fact that with rising temperature the conductivity of the samples also strongly increases as will be shown in section 5.2. This leads to increasing dielectric losses inside the resonant cavity thus strongly reducing the so-called quality factor (Q) of the cavity. The disturbing effects of the sample on the cavity properties get more significant the higher the conductivity and the larger the mass of a sample. Thus for lower doping levels (lower σ) the effects are marginal. If the dielectric losses become too large, ESR measurements are no longer possible as was the case for sample n67, which could only be measured up to 180 K (see Fig. 5.18). Since the signal intensity is proportional to the cavity quality factor a decrease in Q also leads to a decrease in signal intensity. Thus it has to be taken into account for a quantitative analysis of signal intensities and in particular for the comparison of ESR signals obtained at various temperatures. This subject is described in more detail in appendix A.

Fig. 5.18 shows the signal intensities as a function of temperature for samples n33, n67 and n133 in a similar plot as in Fig. 5.17. The intensities were corrected for the change in

the quality factor. Since reduction of the amount of material inside the cavity reduces the dielectric losses, the T-dependence of a thin film of sample n67 (prepared in the same run on Corning glass) is included in Fig. 5.18.

Powder sample n133 (which has a relatively small mass of only 18 mg) exhibits the same Curie-like behaviour as sample n1. For the other two samples n33 and n67 the 1/T-behaviour is nicely obeyed at low T, whereas the signal intensity decreases somewhat faster than expected from the Curie-law at higher temperatures. On the other hand, the intensity of the thin film doped with 67 ppm even seems to increase in the high-T region. This increase could be due to the fact that at the highest T, as the CE line significantly broadens (Fig. 5.10, p. 55), the uncertainty in determining the area under the absorption curve becomes appreciable. As one has to subtract an unknown background (usually a linear function) to account for the non-horizontal baseline, the area could easily be over-estimated. On the other hand the losses in powder samples at high temperatures greatly complicate ESR measurements, and it is possible that more experimental corrections to the observed signal intensity (for n33 and n67) have to be made.

Thus it is concluded that the paramagnetic suceptibility of the electrons leading to the CE line obeys the Curie (1/T-) law between liquid helium and room temperature. This means that the total number (or spin density) of the CE line electrons does not change with T. However, at the present time additional effects at elevated temperatures cannot be totally ruled out on the basis of the data available. Such an effect would be, for example, the thermal excitation of electrons into states where they give less ESR response thus leading to a deviation from the 1/T-behaviour.

Before drawing conclusions a short comparison with the situation in crystalline silicon will be useful at this point. The principles of semiconductor paramagnetism have already been lined out in chapter 3.1.3.2.

To illustrate what has been observed in crystalline silicon for various temperature and doping ranges, Fig. 5.19 shows a schematic plot (note the logarithmic scale on both axes) of χ-vs.-T-curves which are expected in different cases. The dashed line of slope -1 represents the Curie-law (like for μc-Si:H), whereas the dashed horizontal line stands for a temperature independent susceptibility as expected for Pauli-electrons at low T and high electron concentration (i. e. in the region of marked degeneracy). The temperature range of the plot is arbitrary for this schematic picture.

The electrons located at the donor atoms in weakly phosphorus doped n-type crystalline silicon can be regarded as a system of Curie paramagnets (Mooser, 1955; Ue and Maekawa, 1971). Experimentally this was reported for the P-hyperfine doublet at lower temperatures (Cullis and Marko, 1975; Maekawa and Kinoshita, 1965).

Also in the earliest spin resonance measurements of n-type Si crystals (Portis *et al.*, 1953) with a doping concentration N_D of $1\text{–}2\cdot10^{18}$ cm^{-3} a single line was found which showed Curie-like behaviour for temperatures between 80 K and 300 K. A deviation from the Curie law at low T was observed and interpreted as the change from temperature dependent Curie- to temperature *in*dependent Pauli-paramagnetism (i. e. the transition

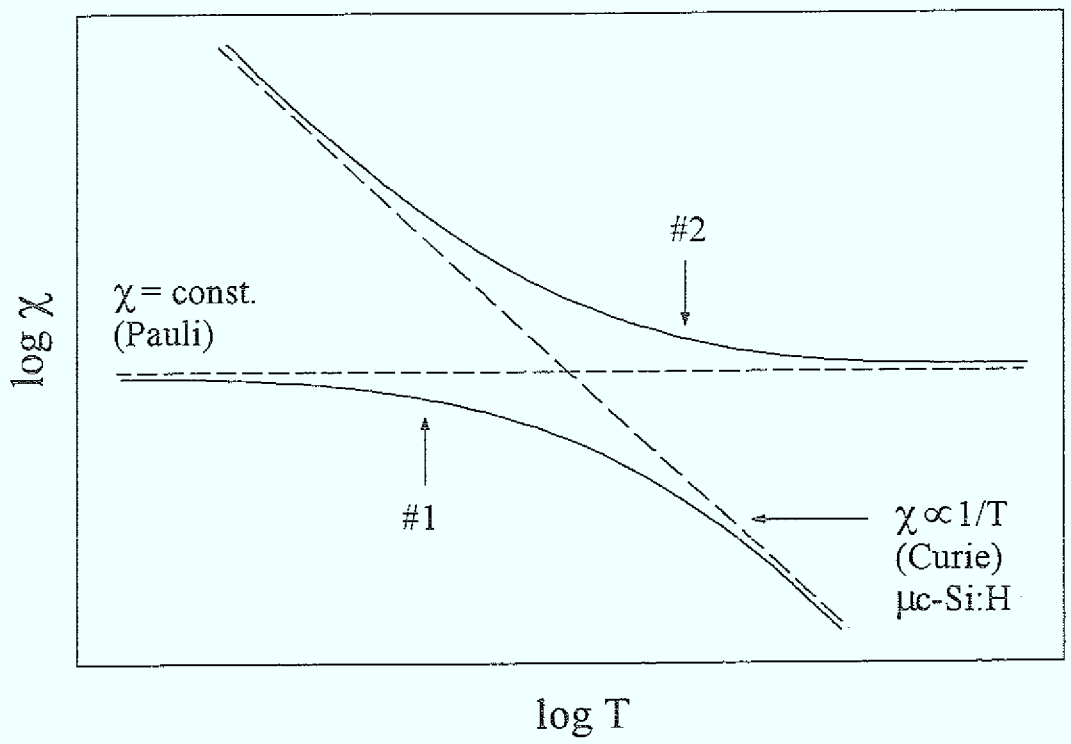

Figure 5.19: Schematic plot χ(T)-curves illustrating different situations in crystalline silicon. Dashed lines represent Curie- and Pauli law. The meaning of the solid lines is explained in the text.

from a non-degenerate to a degenerate semiconductor), which is illustrated by the solid curve #1 in Fig. 5.19.

To account for the two general types of magnetic behaviour (Curie- and Pauli- like) some authors describe their experimental susceptibility data in terms of a two-component model, consisting of electrons following a Curie- or Curie-Weiss-law[7] on the one hand and electrons with a Pauli spin-susceptibility on the other hand. This was done by Ue and Maekawa (1971) ($N_D = 1.5 \cdot 10^{18} - 1.1 \cdot 10^{20}$ cm^{-3}) and Cullis and Marko (1975) ($N_D = 5 \cdot 10^{16} - 1.6 \cdot 10^{18}$ cm^{-3}). In these works the concentrations of the two different types of electrons are obtained as results of numerical fits to the underlying model and are independent of temperature. The resultant susceptibility as the sum of the two components is shown as the solid line #2 in Fig. 5.19 under the additional assumption that the degenerate part of the electrons remains degenerate over the whole temperature range shown.

Even though the dopant concentrations in the works cited above are well in the range of

[7]A generalization of the Curie-law ($\chi \propto 1/T$) is the so-called Curie-Weiss-law $\chi \propto 1/(T-\theta)$ with the Curie-Weiss temperature θ. It is of great importance for example when studying ferromagnetic phenomena.

the observed CE spin densities in μc-Si:H, we observe (within experimental uncertainties) *no* deviation from the Curie-law between between 4.5 and 300 K. Assuming the CE signal as originating from electrons in a free electron gas and taking the observed spin densities as a measure of the electron concentration n, one could calculate the so-called *degeneracy temperature* T_{deg} below which the electron gas becomes degenerate. At a given electron concentration n and with an effective mass m^* of the electrons, which is taken as the density-of-states effective mass $m^* = 1.08m_e$ for low temperatures[8], T_{deg} is given by

$$T_{deg} = (3/\pi)^{\frac{2}{3}} \frac{h^2}{8k_B m^*} \cdot n^{\frac{2}{3}} \tag{5.5}$$

Using $n = 2.4 \cdot 10^{18}$ cm^{-3} (sample n133) a degeneracy temperature of about 70 K results. However, between 70 K and 4.5 K Curie-like behaviour is found. This means the electrons seen in ESR at these temperatures cannot be treated as a free electron gas, and thus it is very unlikely that the major part of them is located in the conduction band. This has already been concluded for lower doping in section 5.1.3.3 from Lépine's calculations (Lépine, 1970). Certainly it cannot be excluded that a small fraction of them does in fact constitute a free electron gas, possibly in the CB, having a much lower T_{deg} (due to the much lower n). To check this asumption means going to lower temperatures, which was not possible with our experimental set-up.

c. Summary

- The CE spin density $N_s(CE)$ is closely related to doping level and room temperature dark conductivity.
- With increasing temperature the CE signal intensities decrease as 1/T, i. e. according to the Curie-law, in the whole temperature range between 4.2 and 300 K almost irrespective of doping level. Still for the highest temperatures and doping levels slight deviations from a 1/T-behaviour occur, and additional temperature activated effects reducing the observable number of spins cannot be excluded.
- Electrons are non-degenerate for all temperatures and doping levels.

[8]The effective mass is temperature dependent and varies from $1.07m_e$ to $1.18m_e$ between 0 K and 300 K (Böer, 1990).

5.2 Conductivity Measurements

To obtain information about the transport mechanism in microcrystalline silicon and for a detailed comparison with the ESR data the conductivity of various samples was measured as a function of temperature. It will turn out that the conductivity data in conjunction with the ESR results of the preceding sections allow to draw important conclusions concerning the relationship between electronic states seen in ESR and the charge carriers responsible for the current transport in the material. Due to the missing of a CE resonance in the spectra of p-type samples the emphasis was on n-doped material, but some p-type samples are nevertheless included.

Fig. 5.20 shows the dark conductivities of several n- and p-type samples in an Arrhenius-plot ($\log(\sigma)$ as a function of 1000/T) for temperatures between 4 K (for samples with higher doping levels) and room temperature. The conductivity of 1-ppm samples both with n- and p-type doping became too low to be measured down to liquid helium temperatures. As has been mentioned before, the conductivity exhibits no singly activated behaviour according

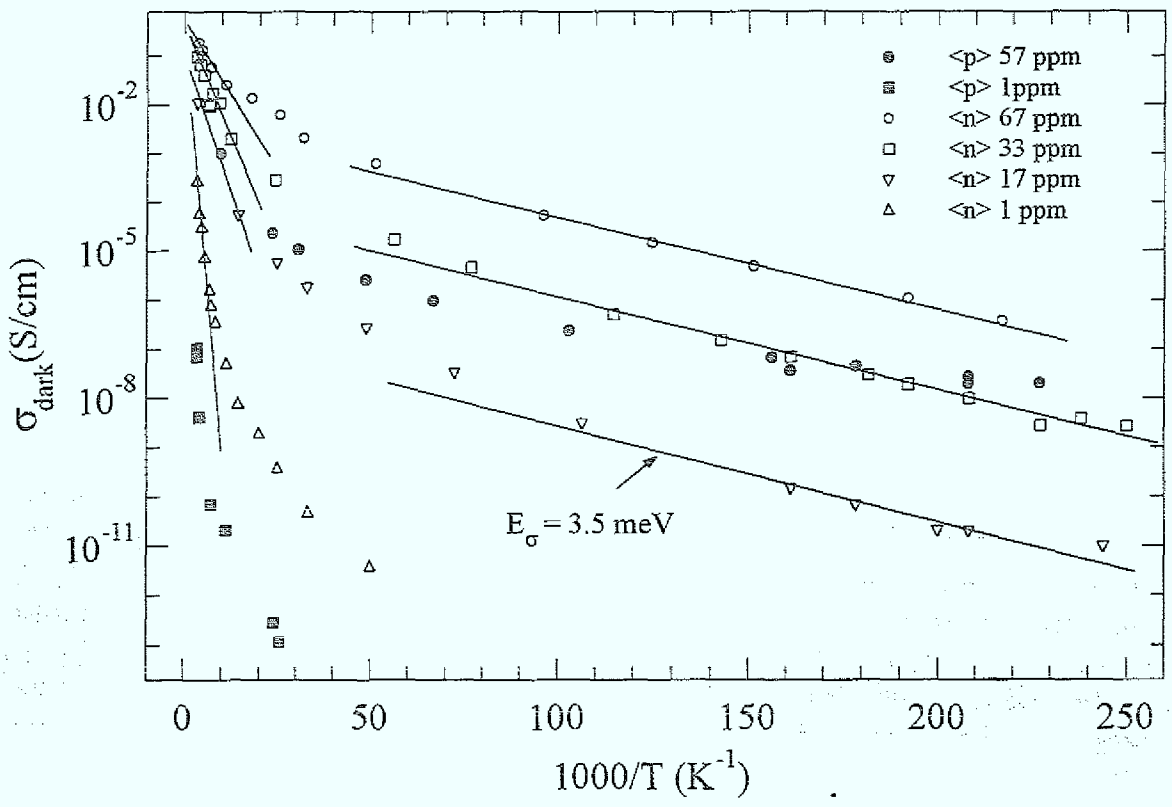

Figure 5.20: Dark conductivity of n-(open symbols) and p-type (closed symbols) μc-Si:H for 4 K < T < 300 K. E_σ is the low-temperature activation energy described in the text.

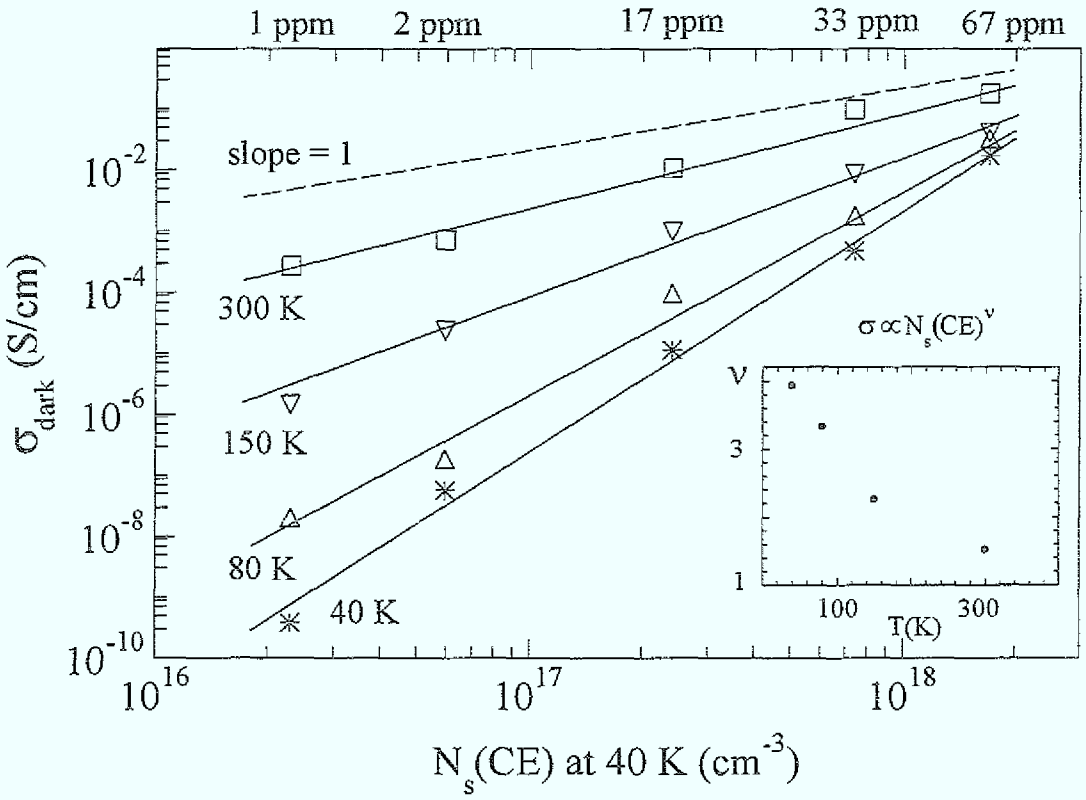

Figure 5.21: Dark conductivity at various temperatures as a function of CE spin density at 40 K. The dashed line of slope 1 corresponds to $\sigma \propto N_s$. The inset shows a plot of ν vs. T for $\sigma \propto N_s^{\nu}$.

to Eq. 3.19, p. 24, if one looks at the whole temperature range investigated. This fact is well-known in microcrystalline silicon and was already discussed in section 3.2.1.

In the region of very low temperatures (4 K < T < 15 K), however, the log(σ)-vs.-1/T-curves can be nicely approximated by straight lines indicating one single transport activation energy. These lines in the low-temperature region are included in Fig. 5.20. The activation energy E_σ = 3.5 meV deduced from the slopes of the lines is essentially the same irrespective of doping for all n-type samples, whereas in sample p57 the value is lower (1.6 meV). For higher temperatures the range of E_σ-values shifts to much higher energies. To get a rough idea, straight lines drawn through the high temperature points yield activation energies of 115 meV, 35 meV, 33 meV and 24 meV for samples n1, n17, n33 and n67, respectively.

Having temperature-dependent conductivity data available one can extend the plot of Fig. 5.16 with temperature as additional parameter. This was done in Fig. 5.21 where the conductivity at various temperatures is plotted vs. the CE spin density obtained at 40 K. The upper horizontal scale indicates the respective gas phase doping ratios corresponding

to the spin densities on the lower (primary) axis. For all temperatures the σ-vs.-N_s-curves are approximately straight lines in the double-logarithmic plot of Fig. 5.21 indicating a relation $\sigma \propto N_s(CE)^\nu$ with an exponent ν. This exponent corresponds to the slope of the lines at the respective temperatures. It decreases with T approaching $\nu = 1$ at high temperatures which would be equivalent to $\sigma \propto N_s(CE)$ and is indicated by the dashed line ('slope = 1') in Fig. 5.21. The gradual approach to $\nu = 1$ with rising T is further illustrated in the inset where the exponent ν (or slope of the lines) is shown as a function of temperature.

Obviously with rising temperature more and more of the electrons seen as CE signal in ESR can directly take part in transport (even in samples with only little doping). At high temperatures all CE electrons would contribute to the conductivity irrespective of doping level. One can think of electrons being located at their donor sites or in other localized states and getting thermally excited into the conduction band. There they can move freely and carry the electrical current, but due to the microcrystalline structure their mobility is only around 1 $cm^2V^{-1}s^{-1}$ (Backhausen *et al.*, 1997; Carius *et al.*, 1997a) and hence much lower than in crystalline silicon.

The next section will give a detailed account of the conductivity behaviour of microcrystalline silicon. In particular, the relationship between ESR and transport data will be established, the CE line in the various distinct (localized and delocalized) states will be identified (depending on temperature and doping level), and thus the circle of the experimental data on the CE line presented in section 5 and the conclusions drawn from them will be closed.

5.3 The Relationship between ESR and Transport

5.3.1 Electron Densities

In the previous sections results on the ESR spin densities (in particular of the CE resonance) have been presented and related to conductivity data. It is very instructive to add data on electron or donor densities obtained from simple considerations or other experiments and investigate if and how they fit together or deviate from each other. To this end the following quantities are compiled for the n-type samples in Table 5.2 together with the values of σ_d^{RT}:

1. The density of phosphorus atoms as expected from the doping ratio in the gas phase N_g using a build-in ratio of P to Si of 0.5. The value of 0.5 is deduced from a comparison with SIMS measurements as will be shown shortly. With the atomic density of silicon of $N_{Si} = 4.84 \cdot 10^{22}$ cm^{-3} N_g is simply given by $N_g = 0.5 \times$ (gas phase doping ratio in ppm) $\times 10^{-6} \times 4.84 \cdot 10^{22}$ cm^{-3}.

2. The spin density $N_s = N_s(CE)$ of the conduction electron resonance at T = 40 K as shown in Fig. 5.16 (and Fig. 5.21).

3. The ratio $\frac{N_g}{N_s}$ of these two quantities.

4. The electron density N_σ obtained from the room temperature dark conductivity by applying the formula $\sigma = N_\sigma e \mu$ with $\mu \approx 1$ cm^{2}V^{-1}s^{-1}, a typical value for μc-Si:H (Backhausen *et al.*, 1997) at room temperature.

5. If available, the phosphorus density obtained by measurements with high resolution secondary ion mass spectroscopy (SIMS) (N_{SIMS})[9].

6. For one sample the electron density N_H deduced from Hall-effect measurements (Harder, 1998). Note that Hall measurements in lightly doped samples are difficult and have only very recently been performed on the material presented in this work.

The use of a build-in ratio P to Si of 0.5 is justified by a comparison of N_g with N_{SIMS} (columns 1 and 6). It is seen that, on the average, the dopant density calculated from the gas phase doping ratio and corrected with a build-in ratio P to Si of 0.5 agrees with the phosphorus density obtained in SIMS measurements. This important result is in agreement with earlier reports (Carius *et al.*, 1997a) and allows to calculate the phosphorus concentration in P-doped μc-Si:H directly from the gas phase doping ratio using the simple formula given under point 1.

[9]Note that with a quadrupole mass spectrometer the sensitivity limit for the measurement of P-concentrations exceeds several times 10^{18} 1/cm^3 due to the presence of silicon hydrides of nearly the same mass as the phosphorus ions. By using a high resolution mass spectrometer the mass defect between ^{31}P and the different Si hydrides can be made use of, and thus a discrimination between the respective ions becomes possible.

#	$N_g(\mathrm{cm}^{-3})$	$N_s(\mathrm{cm}^{-3})$	N_g/N_s	$\sigma_d^{RT}(\mathrm{S/cm})$	$N_\sigma(\mathrm{cm}^{-3})$	$N_{SIMS}(\mathrm{cm}^{-3})$	$N_H(\mathrm{cm}^{-3})$
n1	$2.4 \cdot 10^{16}$	$3.3 \cdot 10^{16}$	0.73	$2.7 \cdot 10^{-4}$	$1.7 \cdot 10^{15}$	—	—
n2	$4.1 \cdot 10^{16}$	$7.7 \cdot 10^{16}$	0.53	$7.2 \cdot 10^{-4}$	$4.5 \cdot 10^{15}$	—	—
n3a	$8.0 \cdot 10^{16}$	$8.4 \cdot 10^{16}$	0.95	$1.1 \cdot 10^{-3}$	$6.9 \cdot 10^{15}$	—	—
n3b	$8.0 \cdot 10^{16}$	$1.8 \cdot 10^{17}$	0.44	$5.0 \cdot 10^{-3}$	$3.1 \cdot 10^{16}$	$1.3 \cdot 10^{17}$	—
n17	$4.0 \cdot 10^{17}$	$2.9 \cdot 10^{17}$	1.4	$1.1 \cdot 10^{-2}$	$6.9 \cdot 10^{16}$	—	$3.0 \cdot 10^{17}$
n33	$8.0 \cdot 10^{17}$	$8.6 \cdot 10^{17}$	0.93	$9.8 \cdot 10^{-2}$	$6.2 \cdot 10^{17}$	—	—
n67	$1.6 \cdot 10^{18}$	$2.1 \cdot 10^{18}$	0.76	$1.8 \cdot 10^{-1}$	$1.1 \cdot 10^{18}$	$1.7 \cdot 10^{18}$	—
n133	$3.2 \cdot 10^{18}$	$2.4 \cdot 10^{18}$	1.3	$5.1 \cdot 10^{-1}$	$3.2 \cdot 10^{18}$	$1.8 \cdot 10^{18}$	—

Table 5.2: Electron and donor densities in n-type samples. The quantities are defined in the text.

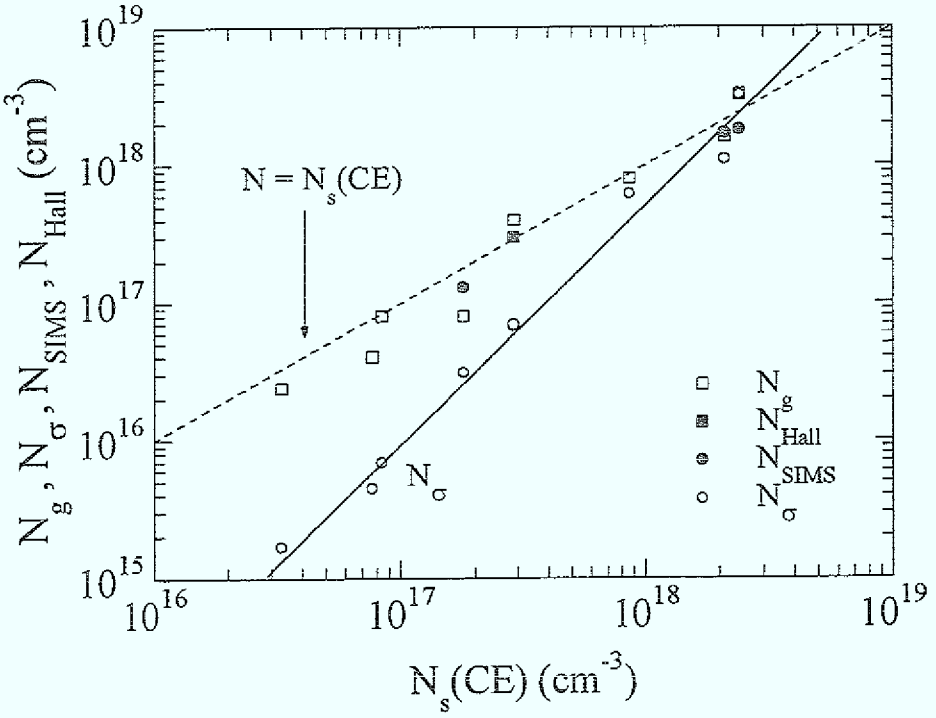

Figure 5.22: Electron and donor densities in n-type samples as given in Table 5.2. Data are plotted vs. the CE spin density $N_s(CE)$ at 40 K. The other quantities are defined in the text. The solid line is a guide to the eye and the dotted line denotes the case when $N = N_s(CE)$.

To illustrate the data of Table 5.2 the different dopant and electron density values are plotted vs. the CE spin density $N_s(CE)$ in Fig. 5.22 where the case when $N = N_s(CE)$ is indicated by the dotted line. The results of Table 5.2 and Fig. 5.22 give valuable insights for the understanding of phosphorus-doped material and allow to establish the

relationship between ESR data (conduction electron line) and conductivity. Furthermore one can describe the conductivity in terms of the models outlined in section 3.2.

The most remarkable result of Fig. 5.22 is that the CE spin density $N_s(CE)$ is essentially equal to the donor density calculated from the gas phase doping ratio, to the phosphorus concentration deduced from SIMS data, to the carrier density obtained by Hall-effect measurements and finally, for high doping levels, it also agrees with the electron density calculated from the room temperature dark conductivity. This can be interpreted as follows:

During the deposition the phosphorus out of the reaction plasma is build into the microcrystalline solid with a build-in ratio of 0.5. Every donor atom is incorporated in a four-fold coordination (as is essential for the doping process) so that every P-atom can at sufficiently high temperatures and doping concentrations provide one electron to take part in the conduction process. This behaviour is reflected on the one hand by the agreement of N_σ with N_s, N_g and N_{SIMS} for the highest doping levels in Fig. 5.22 and from $N_s = N_H$ for intermediate doping. On the other hand it can be deduced for the lowest doping levels from the gradual approach of the relation $\sigma \propto N_s$ in Fig. 5.21 if the temperature becomes high enough. The disagreement between N_σ and $N_s(CE)$ for low doping is mainly a result of the reduced mobility (< 1 cm^{2}V^{-1}s^{-1}) for these samples as confirmed by recent Hall effect measurements. It follows that the doping efficiency, defined as the ratio between the number or concentration of active dopants to the number of incorporated dopants, is unity like in crystalline silicon and in contrast to amorphous silicon, where it is much lower and strongly depends on the dopant gas concentration in the reaction gas mixture (Stutzmann *et al.*, 1987).

From the agreement between dopant and carrier densities deduced from the different methods with the ESR spin densities N_s of the CE resonance it is obvious that both electric transport and electron spin resonance are governed by the excess electrons introduced via the doping process. The ESR spin density of the conduction electron line is equal to the phosphorus donor density over 2 orders of magnitude.

5.3.2 The Conduction Mechanism

For convenience the conduction process as deduced from the available data will be described first for the high temperature region (20 K < T < 300 K) and after that for the region of very low temperatures (where the conductivity exhibits a singly activated temperature behaviour).

5.3.2.1 High Temperature Region

It was already (quietly) concluded that at temperatures around room temperature the carrier transport proceeds in the conduction band, into which the electrons were excited from shallow donor states (or tail states). This assumption is just a consequence of the nice agreement between the various phosphorus densities and the electron density N_σ

calculated from $\sigma = N_\sigma e\mu$ for high donor concentrations. In addition, it justifies the use of $\mu \approx 1$ cm^{2}V^{-1}s^{-1} for the electron mobility in the samples with higher doping (whereas for lower doping levels the mobility is smaller, see above). At room temperature all of the donors are ionized, the thermal energy is high enough to have a sufficient number of percolation paths (see 3.2.1) and transport takes place by quasi-free electrons in the CB moving along these paths, crossing lower barriers and avoiding high ones. The conductivity decrease with a lowering of T is ascribed both to the decreasing number of electrons excited to the CB and to the increased length of percolation paths for the carriers. This interpretation is adopted from previous publications (Backhausen *et al.*, 1997; Carius *et al.*, 1997b). A distribution of activation energies (24 – 35 meV for samples n17, n33 and n67) in this intermediate temperature range between room temperature and 20 K is a result of a distribution in barrier heights between crystalline regions and the thermal excitation out of tail states with varying energy positions below the conduction band. Still the activation energies are comparable with the ionization energy of phosphorus donor electrons in crystalline silicon of 45 meV.

With decreasing doping level, N_σ deviates more and more from $N_s(CE)$. One of the reasons for that is the decrease in carrier mobility going to lower doping levels as found in recent Hall-effect measurements (Carius, 1998; Harder, 1998). Furthermore some of the donor electrons will probably have been trapped by deep defects. With defect densities around $2 \cdot 10^{16}$ cm^{-3}– similar to the donor densities in the samples with the lowest doping levels – this effect can reduce the number of available charge carriers significantly in case of low doping.

For all temperatures the conductivity (at a given temperature) is related to the CE spin density by a power law $\sigma \propto {N_s}^\nu$ with an exponent ν (see inset in Fig. 5.21). The value of ν is about 1.5 for room temperature and decreases further with rising temperature approaching $\nu = 1$.

5.3.2.2 Low Temperature Region

To interpret the conductivity data at low temperatures the brief outline of transport theory in c-Si given in section 3.2.2 is recalled. In crystalline silicon at low T transport proceeds through hopping processes. Keeping in mind the picture of microcrystalline silicon as an interconnected percolation network and the high crystalline volume fraction of the material, similarities between hopping motion in microcrystalline and crystalline silicon can be expected.

One distinguishes between two types of hopping motion: nearest-neighbour and variable-range hopping. The temperature dependence of the former is described by a hopping activation energy ΔE_{hop}. Since an activation energy (of 3.5 meV) is observed for T < 15 K in μc-Si:H an applicability to our case seems appropriate. It has to be kept in mind that for such a mechanism to be possible partial ionization of donor atoms by electron trapping in acceptor or defect states is a necessary condition. To check this, the theoretical values for ΔE_{hop} (as given by Eq. 3.23) were calculated for samples n17, n33 and n67 using the observed CE spin density as donor concentration N_D and $a_0 = 12$ Å

as Bohr radius of the donor wave function deduced from the hyperfine results in section 5.1.3.3. The respective values are 15.2 meV, 11.3 meV and 7.9 meV. They have the same order of magnitude as the experimental activation energy of $E_\sigma = 3.5$ meV, but ΔE_{hop} decreases with decreasing donor density as expected from Eq. 3.23 in contrast to experiment. The discrepancy indicates that the simple model would have to be modified for a quantitative evaluation, which will not be attempted here. However, experimental works on doped crystalline silicon (see e. g. Atkins *et al.*, 1960) yield activation energies around 5 meV very close to the value found in μc-Si:H. For further references containing similar E_σ-values for p- and n-doped silicon the reader is referred to a review article by Chroboczek (1987). Furthermore, if one calculates the conductivities

$$\sigma_{hop} = \sigma_{00} \cdot \exp\left(-\frac{2r_c}{a_0}\right) \cdot \exp\left(-\frac{\Delta E_{hop}}{k_B T}\right) \tag{5.6}$$

$$\text{taking} \quad N_D = N_s,\ a_0 = 12\ \text{Å},\ \Delta E_{hop} = 3.5\,\text{meV}$$

and assuming the same σ_{00} for all three samples, they agree well with the measured conductivities as obtained from Fig. 5.20 with $\sigma_{00} \approx 200 - 300$ S/cm. In conclusion, the well-established model of nearest-neighbour hopping is adopted from crystalline transport theory, since it agrees well with the low-temperature conductivity data in microcrystalline silicon.

The other possible mechanism for hopping motion is variable-range hopping (section 3.2.2.2) between states close to the Fermi level. However, such a mechanism has already been excluded by Finger *et al.* (1993) as an explanation of conductivity data in compensated μc-Si:H, since it was found to lead to unrealisticly high density-of-states values for samples with the highest conductivities. Furthermore a necessary condition for VRH-hopping is $r_D \leq a_0$ for the average inter-donor distance r_D (Mott and Davis, 1979, p. 33). For the material used in the present study this condition is violated, since even in sample n67 $r_D = 52\,\text{Å} > a_0 = 12\,\text{Å}$. Additionally in crystalline silicon VRH was only reported for temperatures below 4.2 K (Bourgoin *et al.*, 1979), a temperature range not accessible in this work. Thus variable-range hopping can be ruled out as the dominant low-temperature transport process in μc-Si:H for T > 4.2 K.

Summary. In summary, the low-temperature conductivity in our samples is described as follows: In highly doped samples the spacing between adjacent donors is small enough to allow for electron hopping from occupied to neighbouring ionized donor states similar to nearest-neighbour hopping well-known in crystalline silicon. The activation energy deduced from the theoretical formulae is similar to the observed values, although the theoretical dependence of the activation energy on donor concentration is not reproduced in experiment. Transport by variable-range hopping, on the other hand, can be excluded mainly because the inter-donor distances are too large as compared to the localization lengths of the donor electron wave functions.

Although in samples with lower dopant concentrations the activation energy should be considerably smaller and lead to higher conductivities, this term in Eq. 5.6 is over-compensated by the factor $\exp(-\frac{2r_c}{a_0})$ due to the strong increase of inter-donor separation. Therefore the conductivity in lightly doped material drops below the detection limit at low temperatures.

5.3.3 Electronic States in ESR and Transport

With the results of the preceding sections the contributions of the respective electronic states to both transport and electron spin resonance have been identified and distinguished from each other for the different temperatures and doping levels. The picture one obtains is briefly summarized now.

The conduction electron resonance in ESR is due to the additional electrons introduced by the incorporation of phosphorus dopants into the n-type material. These electrons occupy different states depending on temperature and doping level. Starting at low T (< 20 K), the donor electrons are mostly localized at their donor sites or in conduction band tail states inside the crystallites. The absence of hyperfine interaction is explained by the arguments presented in section 5.1.3.3. In addition a certain fraction of them might be trapped by deep defects. The CE spin density measured by ESR is *equal* to the concentration of incorporated donors. Conduction in this temperature region proceeds via hopping motion of electrons between neutral and positively charged (ionized) donors.

At higher temperatures (> 20 K) an increasing number of electrons is excited into delocalized conduction band states, but at any temperature the carriers are non-degenerate for the doping range investigated. The electrons in the CB still give an ESR signal, but the transition to delocalized states is accompanied by appreciable line broadening and a slight decrease in g-value. The ESR signal intensity decreases according to the Curie law in the whole temperature range. However, slight deviations for some of the samples might indicate a partial excitation into states with weaker ESR response.

Transport is not governed by hopping anymore, but can be interpreted as a percolation process through an interconnected network where potential barriers of varying height have to be crossed or by-passed. This is reflected by a distribution of activation energies for temperatures larger than 20 K. For the highest doping levels, however, the involved activation energies E_σ are between 24 and 35 meV and thus comparable to the binding energy of phosphorus donor electrons in crystalline silicon (45 meV). At room temperature and high doping levels all electrons are excited into the conduction band, and the conductivity can be calculated simply by $\sigma = N_D e \mu$ with $\mu \approx 1\text{cm}^2\text{V}^{-1}\text{s}^{-1}$ and the donor (or CE spin) density N_D. For lower doping levels the mobilities are smaller due to a reduction of the number of available percolation paths or an increase in path lengths.

Chapter 6

Measurements under Light Illumination

So far the material was studied in the dark under equilibrium conditions without any external perturbation (except for the perturbation by measuring ESR, of course). Having in mind an application of microcrystalline silicon in optoelectronic devices like solar cells or colour sensors, its behaviour upon light illumination is naturally of interest. It allows to study excitation and recombination processes, occupation and energy position of electronic states and the transient behaviour of the system upon time-dependent perturbations (the simplest case of which is switching the illumination on and off).

This chapter will start with steady state measurements under constant light illumination conditions. Like in the preceding chapter ESR data (abbreviated LESR for 'light induced ESR') are presented first, followed by photoconductivity (σ_{ph}) results. Emphasis is again put on the doping dependence and the relation to data obtained in the dark (chapter 5).

A lot of additional information can be gained by studying the transient behaviour (section 6.2) of the respective resonance signals under various dark and illumination sequences and this time also varying the wavelength of the incident photons. The most striking features are obtained by comparing the effect of light with an energy larger than the bandgap of both crystalline and amorphous silicon ($h\nu > 1.75$ eV) and infrared (IR) light obtained by letting the light pass through a germanium filter ($h\nu < 0.67$ eV). In amorphous silicon IR light is known to cause a quenching of the LESR signal by exciting carriers out of traps and into the bands from where they can easily recombine. As will be seen, the situation in microcrystalline silicon is very different and considerably more complicated. The interpretation of these measurements has consequences for the microscopic picture and the band structure of μc-Si:H.

6.1 Steady State Measurements

6.1.1 ESR

Again the big advantage of ESR is its ability to distinguish between different kinds of states and to investigate the non-equilibrium and transient behaviour of these states separately. As described in section 3.4, light-induced electron excitation (which, of course, always leads to the simultaneous creation of a positively charged hole) from the valence to the conduction band or by photoionization from states within the energy gap changes the number of free carriers or causes variations in the charge state of localized defects ($D^- \leftrightarrow D^0 \leftrightarrow D^+$). Both effects can in principle be detected by ESR. Note again that, like in c-Si, resonances of hole states are not observable by the CW-ESR techniques employed (section 5.1.1.3).

6.1.1.1 Results

To obtain a situation when the system is in a steady state after switching on the light source (halogen lamp, 100 W, with heat filter $h\nu > 1.75$ eV[1]) a waiting time of 5–10 minutes was usually sufficient. After this time the signal intensity is approximately constant and an equilibrium between excitation and recombination is established. As no quantitative conclusions will be drawn from this kind of experiments, it was not attempted to determine light intensity or photon flux. However, all LESR spectra shown in the following were obtained under the same illumination conditions (except for samples p133 and p162, see below). Still one has to keep in mind the unavoidable uncertainties resulting from the use of powder samples (section 4.1, p. 33).

Figs. 6.1 and 6.2 compare the ESR signals in the dark (thick lines) and under light illumination (thin lines) for p- and n-type samples, respectively. Spectra were recorded at 40 K in the TM_{110}-cavity. In Fig. 6.1 the spectrum of an intrinsic sample is included. Very noisy spectra have been smoothed by simple numerical averaging over several adjacent data points.

In case of n-type material only samples with doping levels ≤ 17 ppm showed a detectable difference between light-induced and dark signal and hence samples n33, n67 and n133 are not included in Fig. 6.2. For p-type material LESR response is found for all doping levels. Note that LESR of samples p133 and p162 was measured under different illumination conditions in the TE_{301}-cavity, and thus their intensities are not directly comparable to other samples.

The qualitative features visible in Figs. 6.1 and 6.2 for defect and CE resonances are summarized as follows:

General Remarks. The LESR spectra consist of resonances with similar g-values as in the dark measurements since no additional lines appear in the spectra. To analyse the respective intensities, the g-values of the closely spaced defect state resonances had to

[1]For convenience, the expression "white light" or "band-gap light" for this kind of illumination will be frequently used in the following.

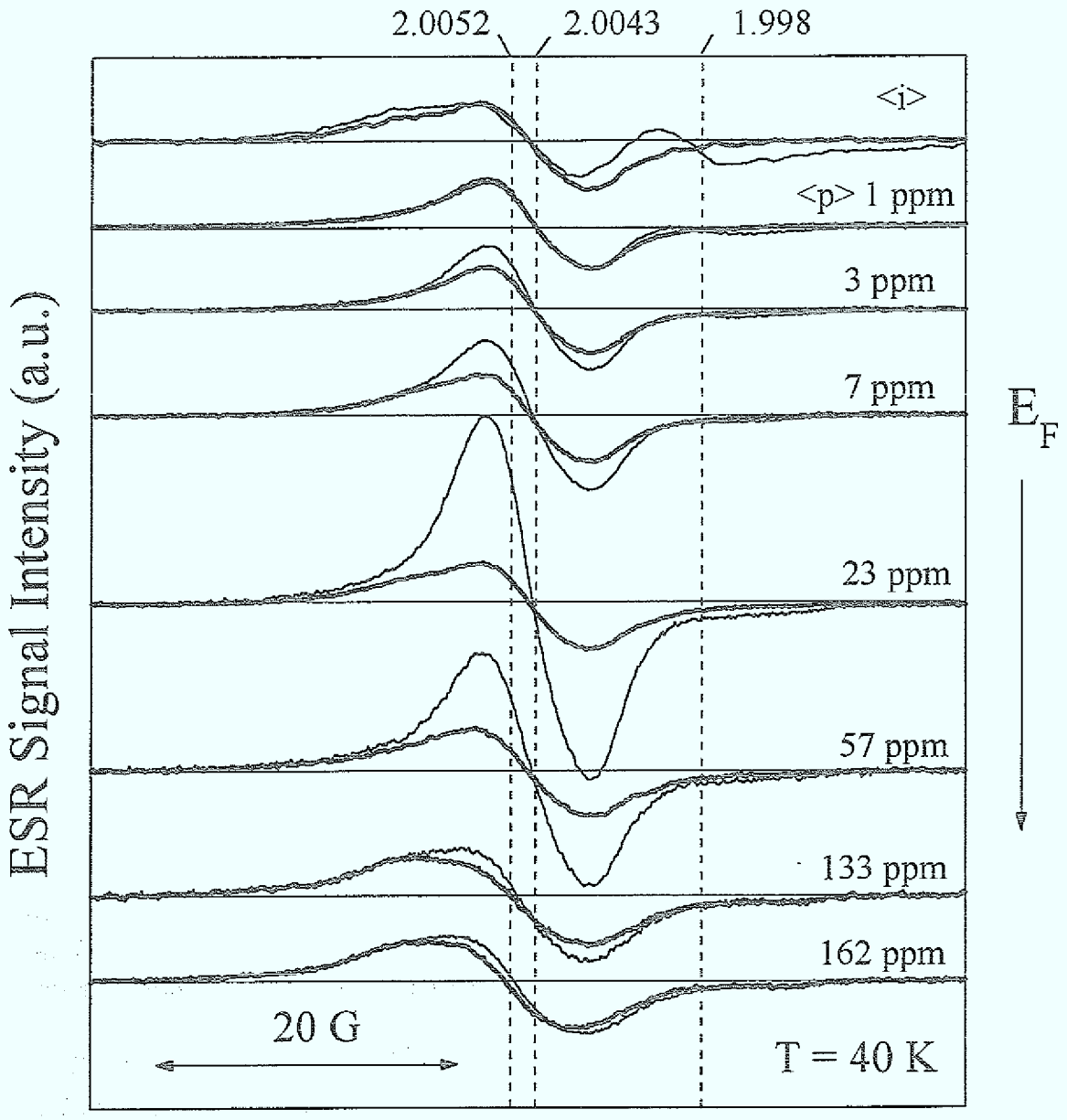

Figure 6.1: LESR (thin lines) and dark ESR (thick lines) spectra of p-type and intrinsic μc-Si:H obtained at T = 40 K. Spectra are normalized to the same peak-to-peak intensities of the *dark* signals. Dashed lines indicate the respective resonance positions for defect and CE states. Note the different illumination conditions for samples p133 and p162 (TE_{301}-cavity).

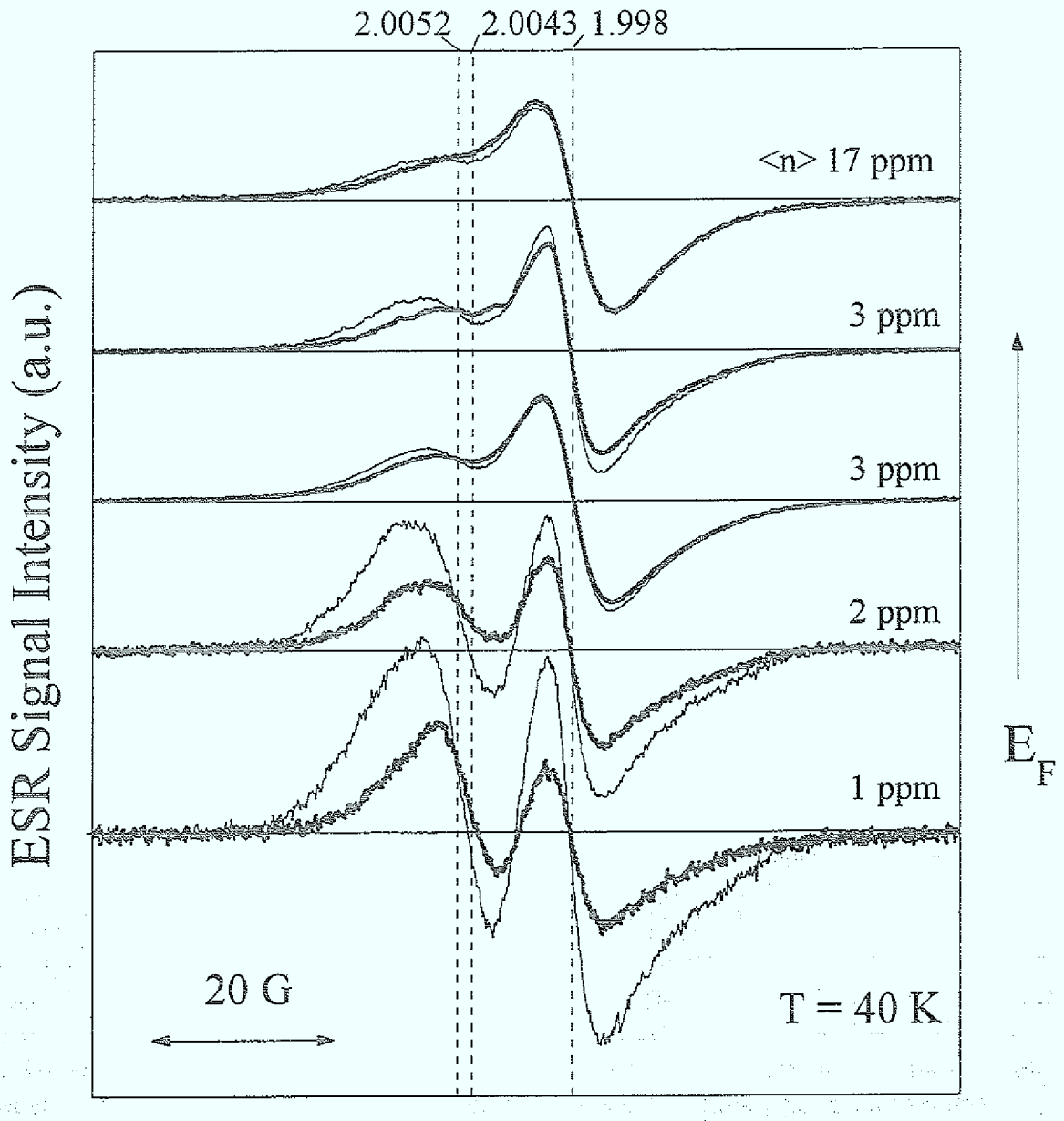

Figure 6.2: LESR (thin lines) and dark ESR (thick lines) spectra of n-type μc-Si:H obtained at T = 40 K. Like in Fig. 6.1 spectra are normalized to the same peak-to-peak intensities of the *dark* signals and dashed lines indicate the respective resonance positions.

be kept constant. Otherwise the ambiguity entering the data analysis due to the usage of 9 (!) free fitting parameters (peak-amplitude, -position and -width for three lines) leads to unreliable results. Therefore small shifts in the g-values would not be detectable in samples where three overlapping resonances are present. In fact, for sample n17 (where only *one* line is enhanced under light illumination) the g-value shifts from 2.0052 to 2.0057 as seen below (Fig. 6.4). Enhancement of defect and CE signals is observed both in p- and n-type material, but the respective intensities strongly vary with doping.

Defect States. For p-doping the relative signal increase of the defect resonances as compared to the dark ESR (in short DESR) intensity increases with increasing doping level. It even seems to pass through a maximum (sample p23) and to decrease again at higher doping (sample p57). On the basis of the data available it cannot be decided, whether the occurence of this maximum is caused by the material properties or simply by the uncertainty inherent to LESR measurements on powdered samples as discussed in section 4.1. *Which* resonances are enhanced under white light will be discussed shortly.

In n-type samples the situation is different. Here the relative defect signal enhancement becomes less with increasing doping between 1 ppm and 17 ppm.

Conduction Electron States. In contrast to the defect states the CE line shows the same doping dependence in p- and n-type samples. Both the relative and the absolute enhancement of the LESR conduction electron response get successively less with an increase of p- or n-type doping level.

For one sample (n2) LESR was also measured using laser light for excitation (λ = 752 nm $\triangleq$ 1.65 eV, maximum power density 250 mW/cm^2). The intensities I were varied over 3 orders of magnitude by grey-scale filters. The results for two different temperatures (10 K and 40 K) are shown in Fig. 6.3 where the difference signal (LESR–DESR) is plotted as a function of incident laser light intensity in units of I_0.

At the highest excitation intensity the signal saturates, but for lower values of I the light induced ESR signal (LESR–DESR) is a function of intensity (or, in other words, generation rate) obeying the relation (LESR–DESR-signal) $\propto I^{0.2}$. Interestingly the same relation is found for the LESR signal in amorphous silicon (Street and Biegelsen, 1982). From this result one concludes directly that even a T = 10 K the recombination process of light induced carriers in μc-Si:H is *non-geminate*, i. e. involves electron-hole pairs which have not been created by the same photon. For geminate pairs (when their density is sufficiently small) the recombination lifetime does not depend on the number of generated pairs, as the same electron and hole as initially created recombine with one another irrespective of the presence of other pairs. Therefore their lifetime τ is constant and is not a function of the incident light intensity I (or generation rate G). However, according to Fig. 6.3 the light induced spin density ΔN_s is proportional to $G^{0.2}$ which means using Eq. 3.26 (p. 31)

$$\Delta N_s = G \cdot \tau \propto G^{0.2} \Longrightarrow \tau \propto G^{-0.8}$$

Hence τ is a function of the generation rate G indicating non-geminate recombination.

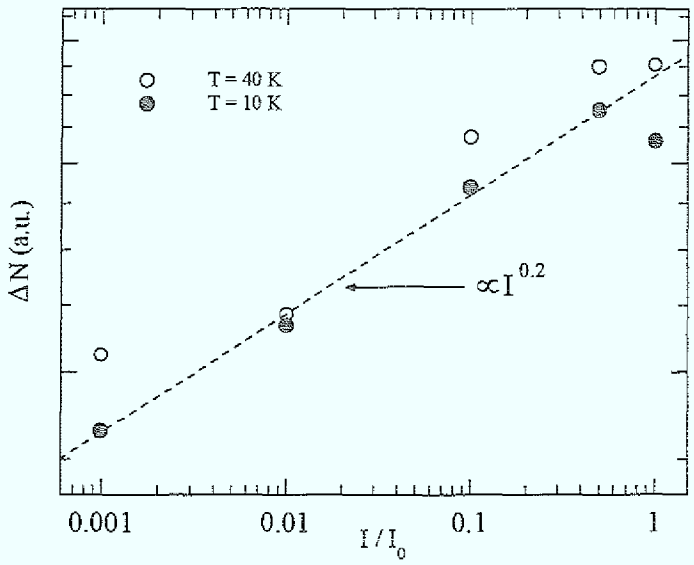

Figure 6.3: Dependence of light induced spin density ΔN on laser light intensity I for T =10 K and 40 K for sample n2. Note the logarithmic scale. The dashed line represents the relation $\Delta N \propto I^{0.2}$.

To make a distinction between the two types of defect resonances it is convenient to subtract the dark from the light-induced spectra. The resulting difference represents only the signal changes by light illumination. This was done in Figs. 6.4(a) and 6.4(b). An important result of Fig. 6.4 is that in p- and n-type samples only *one* kind of defect resonance is enhanced under illumination: in p-type samples it is the line at g = 2.0043 whereas in n-type material it is g =2.0052. Comparing this result with the dark ESR measurements we note a remarkable difference in p-type material: whereas in the dark, with increasing dopant concentration, the line at g = 2.0052 more and more dominates the spectra (Fig. 5.5, p. 45), it is the resonance with g = 2.0043 which is essentially enhanced under illumination.

6.1.1.2 Comparison with Amorphous Silicon

In section 3.4 some basic mechanisms how recombination can take place have been outlined. There is a number of characteristic features influencing the recombination processes, like the presence of band tails and deep defects, which are similar in amorphous and microcrystalline silicon. Therefore a discussion of the LESR data on the basis of a comparison with amorphous silicon is appropriate and will help to identify effects that are specific for μc-Si:H.

Before going into details one important difference between a-Si:H and μc-Si:H has to be emphasized: In amorphous silicon the mobility gap is about 1.75 eV whereas crystalline

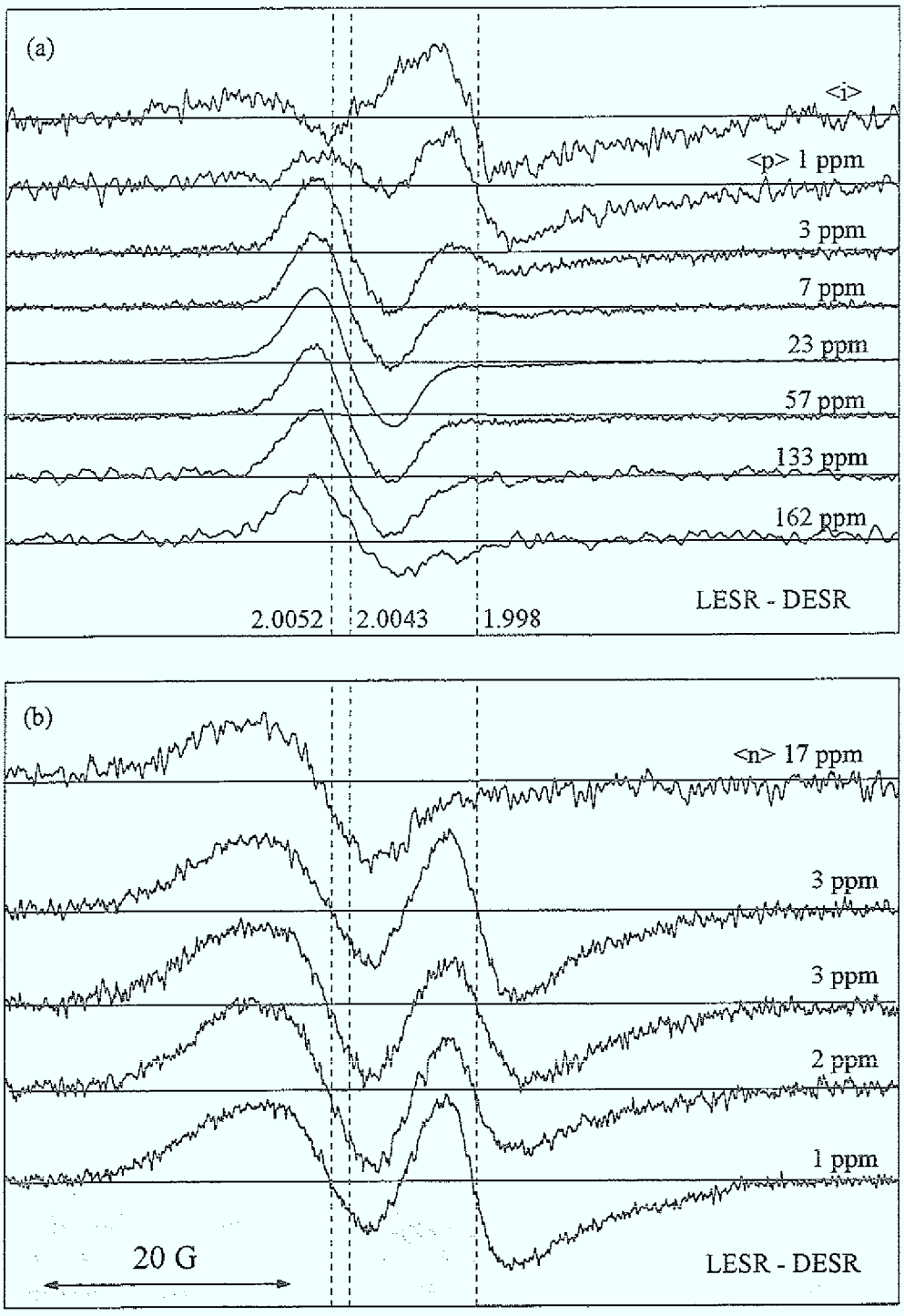

Figure 6.4: Normalized LESR minus dark ESR spectra of p-type and intrinsic (a) and n-type (b) μc-Si:H samples. The vertical dashed lines are at g-values 2.0052, 2.0043 and 1.998 (from the left).

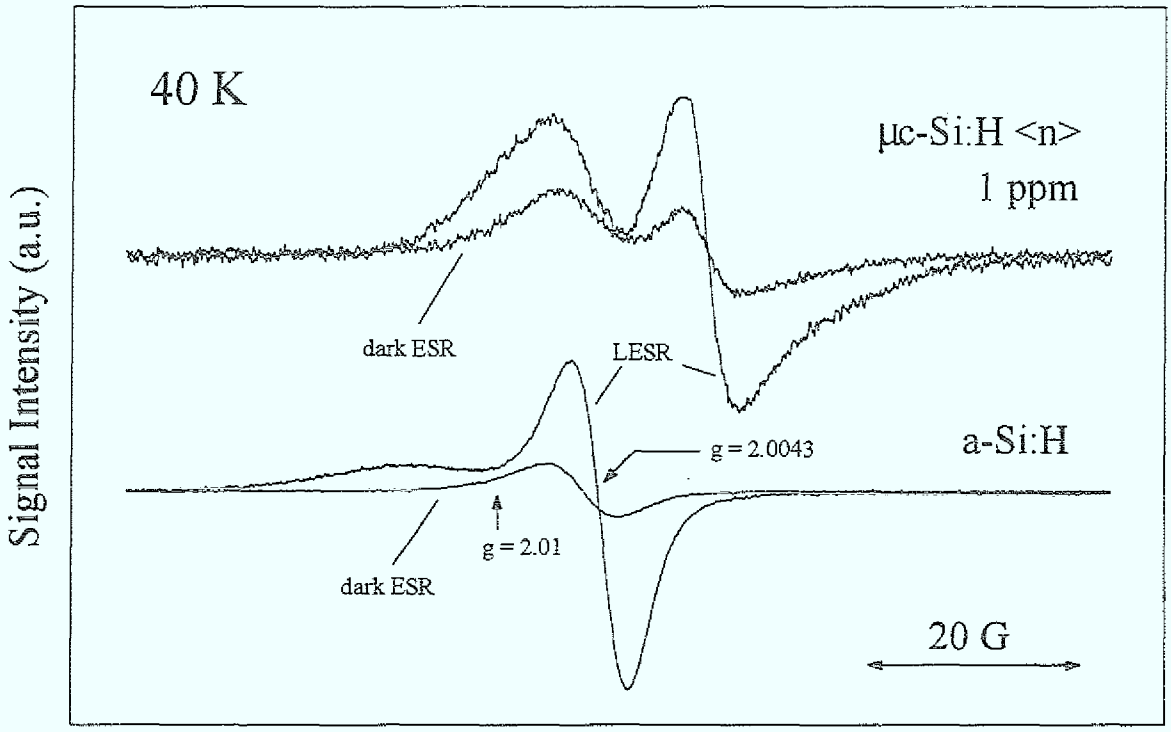

Figure 6.5: Comparison of LESR and dark ESR spectra of μc-Si:H (sample n1) and intrinsic a-Si:H obtained at T = 40 K. For better comparison this time spectra are normalized to similar peak-to-peak intensities of the *light induced* signals.

silicon possesses a bandgap of 1.1 eV. For the crystalline regions in μc-Si:H it is reasonable to assume at least a similar bandgap. In such regions with low bandgap IR light with an energy of $h\nu < 0.67$ eV (as used in this work) can excite electrons even out of deep defect levels (D^-,D^0) into the CB. In a-Si:H this would only be possible if the defects were located appreciably above midgap so that an energy of only 0.67 eV is sufficient for an excitation into the conduction band. This is reflected by the observation that μc-Si:H exhibits a considerable LESR signal upon illumination with IR light, whereas in a-Si:H application of IR light invariably leads to a quenching of the LESR signal. This will be further elaborated on in section 6.2.

Fig. 6.5 shows dark and light induced ESR spectra of sample n1 (where enhancement of both defect and CE lines is found) and an intrinsic amorphous silicon sample.

LESR in a-Si:H has been extensively studied in the past. For details see e. g. Street and Biegelsen (1980a,b), Carius (1986) or the review article by Street and Biegelsen (1984).

Light illumination with band-gap light ($h\nu > 1.75$ eV) excites electrons from the valence band (VB) into the conduction band (CB). After excitation the carriers thermalize

first very rapidly ($\approx 10^{-13}$ s) to the band edges and subsequently further on into localized states in the CB- and VB-tail.

In **intrinsic** a-Si:H it is the ESR signal of electrons in the conduction band tail (at g = 2.0043) and the rather broad line of holes in the valence band tail (g = 2.01) which mainly makes up the LESR signal visible in Fig. 6.5 (lower curves).

In ESR spectra of microcrystalline silicon there are no indications of valence band tail states like in a-Si:H. The CE line, on the other hand, is expected to be a superposition of electrons excited to the conduction band and electrons trapped in CB tail states taking into account the results of chapter 5.

Doped amorphous silicon behaves differently than intrinsic material. The situation is illustrated in Fig. 6.6. Shown is the general case of a semiconductor with both conduction and valence band tails as well as (for simplicity) one kind of deep defects. The energy levels of the respective charge states of the defects (D^- and D^0/D^+) are separated by an effective correlation energy U_{eff}. The shaded areas indicate occupied states as determined by the position of the dark Fermi level E_F. Figs. 6.6 (a) and (b) illustrate the simplest excitation and recombination processes in p- and n-type material, respectively. After optical excitation the carriers thermalize to the band edges and some of them are trapped in CB- and VB-tail states.

In **p-type** material (Fig. 6.6(a)), where electrons are *minority* carriers, initially (i. e. in the dark) there is a large number of unoccupied, positively charged D^+-defect states. These have a large capture cross section for electrons and hence effectively act as recombination centers for the minority carriers, meaning that the major part of the photoexcited electrons in the CB tail is captured by defects making the transition $D^+ + e^- \longrightarrow D^0$ (e^- := electron) as indicated in Fig. 6.6(a). This results both in a very short lifetime τ_{min} of the minority electrons and an increase in the number of D^0-states.

Hence in p-type a-Si:H light illumination enhances the dangling bond (g = 2.0055) and the VB-tail resonance (g = 2.01), whereas no resonance of CB-tail electrons appears due to their reduced lifetime.

In microcrystalline silicon it was seen from Fig. 6.1 that a decrease of the LESR CE resonance with rising doping level (downward shift of E_F) is accompanied by an increase of the defect signal at g = 2.0043. This observation is nicely explained in the simple model of Fig. 6.6 with the arguments presented above. The fact that for high doping levels only the defect line at g = 2.0043 increases can be qualitatively understood by the large number of positively charged $D^+_{2.0043}$-states, while many of the $D_{2.0052}$-defects remain neutral for all doping levels. This follows from Figs. 5.4 to 5.6 (section 5.1.2, pp. 44, 45, 47), where the measured spin density of the defects at g = 2.0043 decreases appreciably with rising p-type doping level (pointing to a conversion from D^0 into D^+ as a result of the Fermi level shift towards the valence band).

Additionally it might be possible that $D^+_{2.0043}$-defects have a larger capture cross section for electrons than $D^+_{2.0052}$, but this remains speculative as both quantities are unknown.

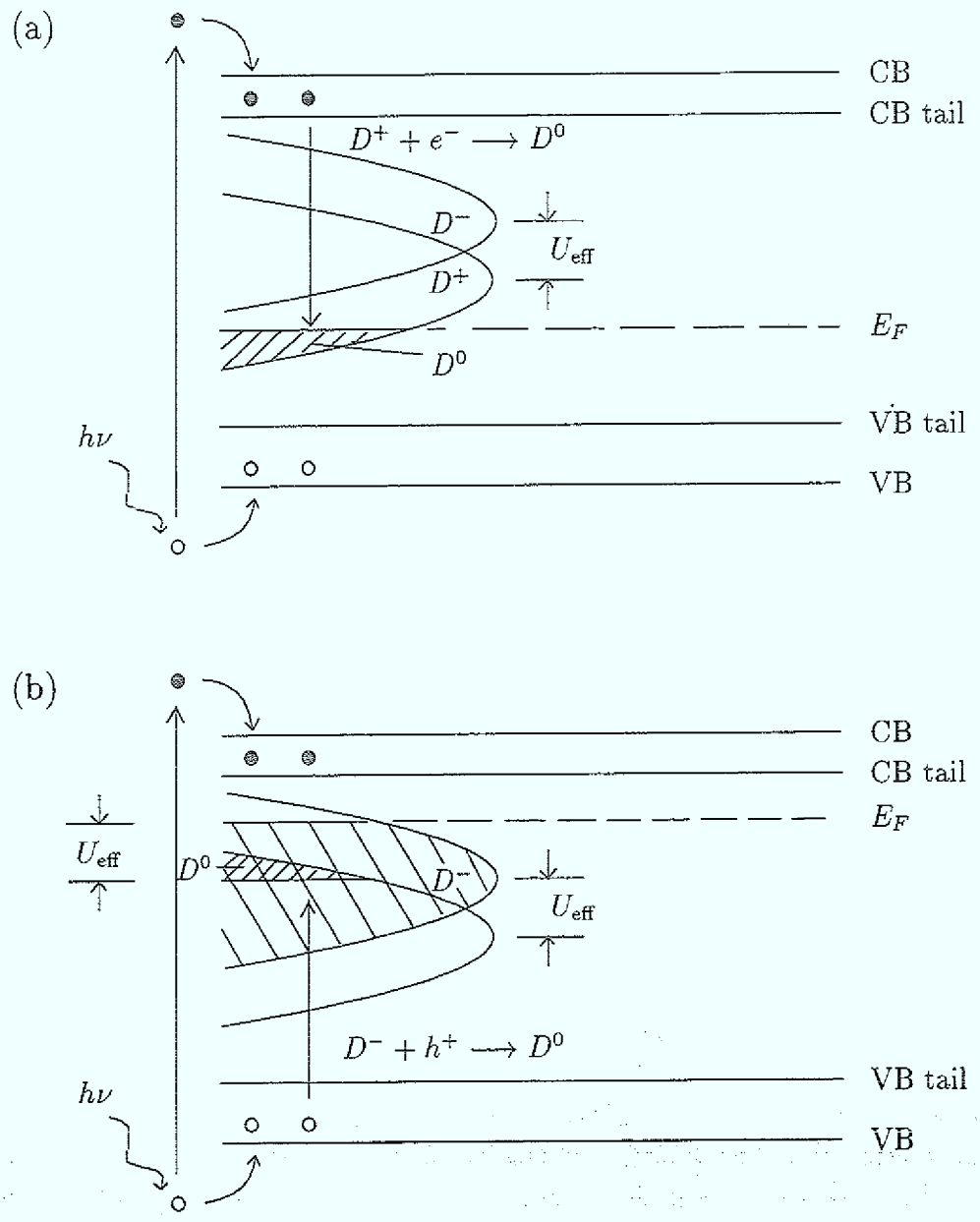

Figure 6.6: Illustration of excitation and recombination processes in p- and n-doped semiconductors containing band tails and deep defects (like a-Si:H). Closed and open circles refer to electrons and holes, respectively. The long arrow on the left-hand side symbolizes the creation of electron-hole pairs by bandgap light. Shaded areas indicate occupied states.

In **n-type** material the situation is analoguous (Fig. 6.6b). Here the Fermi level E_F lies close enough to the CB to allow for double occupation (D^-) of most defect states. Only a small number of positively charged (unoccupied) defects is left. Now the light induced *holes* are the minority carriers and they will be captured very efficiently by the D^--states. Hence this time the hole lifetime becomes very short whereas the electrons should not be much affected.

Again such a situation is nicely illustrated in n-type a-Si:H, where light illumination affects both the dangling bond and the conduction band tail resonance, but leaves the broad valence band tail line at g = 2.01 unobservable due to the reduced hole lifetime.

In n-type μc-Si:H, however, the simple model of Fig. 6.6 fails to explain the experimental results. According to the model, one would not expect any substantial decrease of the light induced ESR response of defects or conduction electrons (majority carriers!) with rising n-type doping level in contrast to what is observed in Fig. 6.2.

6.1.1.3 Discussion

Naturally the failure of such a simple picture is not unexpected in a material as complex as microcrystalline silicon with its various structural constituents. In the first place there are *two* kinds of defect states whose energy positions and effective correlation energies can only be estimated from the ESR data. Secondly the exact spatial location of these defects is not known, and it can be speculated that they are actually found in different structural environments. Thirdly one cannot define one single bandgap in the material as there are both crystalline regions and rests of amorphous phase present simultaneously. Finally an additional complication is the fact that the behaviour of the holes, which give important complementary information in the case of a-Si:H, cannot be studied as they simply are not observed in CW-ESR.

A more sophisticated model has to distinguish between excitation within different structural domains (such as crystallites or amorphous regions) and take into account the presence of more than one kind of defect states. Furthermore the possibility of charge transfer between adjacent regions must be included.

Note further that the position of the Fermi level in Fig. 6.6(b) was chosen such as to allow for a fraction of the defect states to be neutral and thus visible in ESR, as in section 5.1.2 a considerable ESR spin density was measured even in n-type samples with the highest doping levels. A position of the Fermi level as indicated in Fig. 6.6(b) disregards the fact that the main feature in n-type samples is the CE resonance which was found to originate at low T from donor electrons and band tail states both lying relatively close to the conduction band. The occupation of these states requires a position of the Fermi level closer to the conduction band than as it is drawn in Fig. 6.6.

There are several ways to explain this contradiction and most of them have already been mentioned. For example one could put a fraction of the defect states into amorphous regions with a proper choice of the band offset between crystalline and disordered regions. Other possibilities are the presence of potential fluctuations or the assumption that the

defect states seen in ESR of highly n-doped samples possess a correlation energy U_{eff} large enough to shift the D^--band into the same energy region as the donor and tail states. Which of these model assumptions has the major influence on the ESR behaviour cannot be decided at the present time.

To obtain further information photoconductivity and transient data are presented in the following sections.

Before proceeding it is noted that a recombination process of photoexcited electrons with dangling bonds is also seen in spin dependent photoconductivity (SDPC, Lanz, 1995; Will *et al.*, 1997) and optically detected magnetic resonance measurements (ODMR, Depinna *et al.*, 1983; Malten *et al.*, 1998) on microcrystalline silicon, although in the work by Depinna *et al.* it is called donor-acceptor recombination.

6.1.2 Photoconductivity

Fig. 6.7 shows dark and photoconductivity data for some p- and n-type samples. The data for the dark conductivity σ_d have already been presented in Fig. 5.20 on page 73 but are included for comparison with σ_{photo} ($= \sigma_{ph}$). For each kind of data marker the lower and upper curves refer to σ_d and σ_{ph}, respectively. The light source used was the 752 nm-line of a krypton laser.

Looking first at the data for n-type material it is immediately obvious that the ratio σ_{ph}/σ_d decreases strongly with increasing n-type doping level. Arrows between the σ_d- and σ_{ph}-curves indicate this changing difference between both quantities with doping level at a temperature of T = 40 K (1000/T = 25 K^{-1}). At this temperature the results can be directly compared with the LESR measurements (Fig. 6.2) which have also been performed at 40 K. It is found that the decrease in the (LESR–DESR)-difference signals of both defects and conduction electrons with increasing phosphorus concentration as exhibited by Fig. 6.2 coincides qualitatively with the decreasing σ_{ph}/σ_d-ratio. This would suggest that photoconductivity is mainly governed by an increase in the number of electrons in the conduction band or in CB tail states, as monitored by ESR.

However, the behaviour of LESR signal and photoconductivity differ for sample n17 (open circles in Fig. 6.7). Whereas in LESR no enhancement of the CE resonance is detected, the conductivity increases by more than one order of magnitude under light illumination. Although the illumination conditions, i. e. the respective generation rates, were different for LESR and photoconductivity measurements, the dependence of the LESR signal on light intensity is very weak (see Fig. 6.3) and hence this effect cannot account for the difference. As the carrier density determined from Hall-effect measurements on sample n17 is $3.0 \cdot 10^{17}$ cm^{-3} in the dark (Table 5.2), an increase by one order of magnitude would mean a light induced electron density of $3.0 \cdot 10^{18}$ cm^{-3}, whereas no increase in CE spin density is observed in ESR. To explain this discrepancy other effects influencing LESR on the one hand and σ_{ph} on the other hand have to be considered. One of them is the different mean lifetime of optically excited carriers determining LESR and photoconductivity. It is known that for example in amorphous silicon the recombination lifetimes have a wide

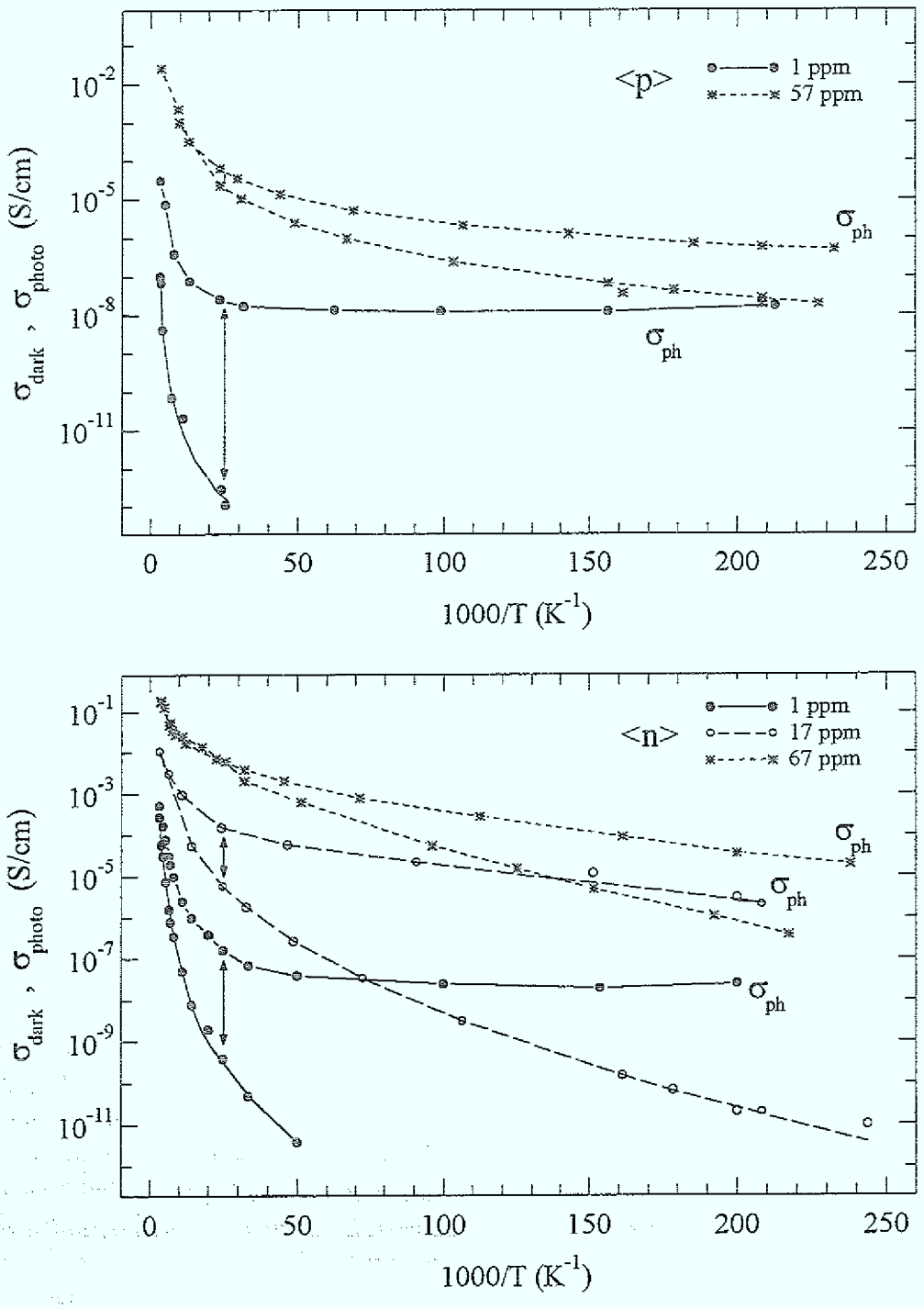

Figure 6.7: Temperature dependence of dark and photoconductivity of p- (top) and n-tpye (bottom) μc-Si:H. For a given kind of data marker the upper curves denote σ_{ph}. Arrows indicate the difference between σ_{ph} and σ_d at T = 40 K.

distribution ranging from 10^{-8} to 10^{3} s (Street and Biegelsen, 1982). Out of this distribution the longest-lived pairs contribute most to the LESR signal. Such long recombination lifetimes are also found in microcrystalline silicon where a residual LESR signal persists for up to several hours after switching off the illumination, as will be shown in section 6.2.

To get an estimate for the mean free carrier lifetime showing up in the photoconductivity data one can, on the other hand, calculate the $\eta\mu\tau$-product (section 3.4) e. g. for sample n1 (solid circles in Fig. 6.7) which exhibits both a significant LESR response and a large σ_{ph}/σ_d-ratio. The power density of the incident 752 nm laser light was 200 mW/cm^2 which is equivalent to an incident photon flux of $7.5 \cdot 10^{17}$ photons/(cm^{2}s). Using the absorption coefficient of μc-Si:H for this wavelength of $\approx 10^3$ cm^{-1} at low T yields a penetration depth of $\approx 10^{-3}$ cm. The generation rate G per unit volume is then obtained as

$$G = \frac{7.5 \cdot 10^{17} \frac{\text{photons}}{\text{cm}^2\text{s}}}{10^{-3}\,\text{cm}} = 7.5 \cdot 10^{20}\,\frac{\text{pairs}}{\text{cm}^3\,\text{s}}$$

For $\sigma_{ph} = 2 \cdot 10^{-8}$ S/cm at T $\leq$ 20 K this leads to

$$\eta\mu\tau = \frac{\sigma_{ph}}{Ge} \approx 1.7 \cdot 10^{-10}\,\frac{\text{cm}^2}{\text{V}}$$

Assuming η as close to unity this result shows that the resulting mean lifetimes of the carriers contributing to photoconductivity are very short compared to the long recombination times appearing in ESR, unless the mobility μ becomes extremely small. Hence the lifetimes mainly governing LESR and photoconductivity, respectively, reflect different parts of a wide distribution. Both experiments cannot be compared solely in terms of the density of optically excited carriers, but their respective lifetimes also have to be considered. Still the general behaviour (decrease of LESR CE signal and σ_{ph}/σ_d-ratio with increasing doping level) is similar in both cases.

A similar behaviour is found for p-type material (upper graph in Fig. 6.7). Here the decrease in the σ_{ph}/σ_d-ratio with doping is also accompanied by a decrease in the (LESR - DESR) response of the CE line as shown in Fig. 6.1. Unfortunately a direct comparison of photoconductivity data with hole concentrations is not possible as holes are not observed in CW-ESR. It is reasonable to assume, however, that the decrease in the light induced CE signal, which is related to a decrease in the mean lifetime of the excited electrons, will be accompanied by a decrease in hole lifetime as their recombination partners. Hence the photoconductivity in p-type samples reflects the lifetime distributions of electrons *and* holes and the connection between σ_{ph}- and LESR-data can be qualitatively discussed in the same manner as was done above for n-type specimens.

Interestingly the photoconductivity is constant below T = 20 K for low doping levels being equivalent to a temperature independent $\eta\mu\tau$-product. Note that such a behaviour is also found in amorphous silicon (Carius, 1986), where $\eta\mu\tau$ reaches a value of $\approx 10^{-11}$ cm^{2}V^{-1} (Hoheisel *et al.*, 1983, 1984) almost irrespective of defect density or doping level and somewhat lower than what is found in μc-Si:H. For higher doping levels, however, $\eta\mu\tau$ for microcrystalline silicon is larger and depends on T.

6.1.3 Summary of Steady State Results

- Illumination of microcrystalline silicon enhances the resonances which are also present in the dark spectra. No additional lines appear. Light induced ESR response is found both for 'white' light ($h\nu > 1.75$ eV) and for infrared illumination ($h\nu < 0.67$ eV) in contrast to a-Si:H.

- Which resonances are preferably enhanced depends on type of doping and doping level. Concerning the defect states one finds enhancement of the dangling bond resonance at g = 2.0052 in n-type samples whereas the line with g = 2.0043 shows LESR response only in p-type specimens. The light induced signal of the CE line vanishes for the highest doping levels irrespective of type of doping.

- The recombination processes governing the LESR signal are non-geminate.

- The recombination of photoexcited electrons with dangling bonds appears to be one dominant process in accordance with published ODMR and EDMR data.

- CE-LESR signal and photoconductivity decrease with increasing doping level. Therefore both experiments reflect the decrease in free carrier lifetime. It has to be kept in mind, however, that LESR and σ_{ph} measure different parts out of a wide distribution of lifetimes, the LESR signal always being governed by the long-lived charge carrier pairs.

6.2 LESR Transients

6.2.1 General Remarks

To obtain more information on excitation and recombination processes, one way is to monitor the behaviour of the respective resonances (i. e. mainly the occupation of the states in this case) as a function of time under changing illumination conditions. In particular this means sequences where (i) the light is simply switched on and off and (ii) the wavelength of the incident light is varied. For the latter experiment comparison of light with energies larger than the (amorphous and crystalline silicon) bandgap, i. e. $h\nu > 1.75$ eV, and light whose energy is lower even than the bandgap in c-Si (1.1 eV) is particularly interesting. In this case the light passes through a germanium filter leading to infrared (IR) light with an energy $h\nu < 0.67$ eV. The important difference is that with IR light no band-to-band transitions of electrons from the VB into the CB can be induced.

The transient behaviour is mainly determined by the recombination lifetimes of light-induced carriers which in turn depends on the various recombination mechanisms, temperature, doping level, concentration and nature of involved electronic states, the presence of traps and recombination centers within the gap and the material structure (e. g. grain boundaries or surfaces). In particular, if transitions between localized states at low temperatures are involved, the recombination probability depends exponentially on the wave function overlap of the localized electron and hole, i. e. on the average separation of recombination partners. This means conclusions about the location of the defects can also be drawn by studying the recombination behaviour.

Experimentally transients of ESR resonances can be quite easily obtained in samples with a strong LESR signal. One simply keeps the position of the magnetic field constant at the maximum (or minimum) of the observed ESR signal which is the 1st derivative of the aborption line. Hence the maxima or minima are equivalent to the points of maximum slope of the absorption curve. In practice (with phase sensitive detection) this means that one modulates the magnetic field around these points, normally using a relatively large modulation amplitude (MA) to get reasonable signal intensity. In our case usually MA = 10 G was chosen. Two restrictions arise from this procedure:

- Closely spaced resonances such as the two defect lines, whose average separation is only about 1.5 G, cannot be distinguished from each other, if both show non-zero light induced ESR response.
- There has to be a compromise between signal-to-noise ratio and time-resolution given by the integration time at each point of the measured curve. Better resolution on the time axis has to be traded for a poorer signal quality and vice versa. Consequently transients faster than about 100 ms are not detectable with this method for the given signal-to-noise ratios of the LESR signals.

To avoid any confusion arising from our definition of LESR as the total signal under illumination, it has to be emphasized at this point that the transients shown in the following

naturally are the *difference* between dark and light induced signal. Thus, when speaking of 'dark level', we refer to the respective point at the maximum or minimum of a spectrum without light illumination (and certainly not to the baseline of the corresponding field sweep measurement).

6.2.2 Dark and Illumination Sequences

A key experiment which clearly exhibits the pronounced difference between amorphous and microcrystalline silicon is illustrated in Fig. 6.8. Here LESR transients (T = 20 K) of a-Si:H and μc-Si:H are shown (the samples are the same as in Fig. 6.5). A temperature of 20 K was usually chosen for transient measurements for sake of a higher LESR intensity and the resultant better signal-to-noise ratio even for moderate time constants. Possible saturation effects at this temperature can be neglected as the qualitative behaviour of the transients will not be affected and no quantitative information is desired. For the amorphous sample the magnetic field was set on the minimum of the resonance of conduction band tail electrons (as described above) and for the microcrystalline sample n1 on the minimum of the CE line. Both magnetic field positions are indicated by the insets in Fig. 6.8. Then the transient behaviour of the signal intensities [2] at the respective points in the spectra is monitored under the following illumination-and-dark sequence: After steady state illumination with white light ($t < 0$, $h\nu > 1.75$ eV) the light is switched off at t = 0. In both samples the resonance decays with a broad distribution of decay times and after some waiting time, at t_{IR}, the samples are re-illuminated with IR-light ($h\nu < 0.67$ eV) for the remainder of the measuring time.

6.2.2.1 Initial Decay

To examine this experiment in somewhat more detail, let's begin with the first decay of the LESR signal after switching off the white light illumination where the behaviour is quite similar for a-Si:H and μc-Si:H. Both signals decay with a distribution of recombination times and would — without further illumination — leave a residual signal at temperatures below 40 K for several hours. Such a behaviour is well-known for amorphous silicon and related alloys and is assigned to trapped carriers and a large distance between recombination partners. For amorphous silicon this means that the electrons and holes remain in the localized band-tail states into which they have thermalized after excitation. Similar findings were reported for porous silicon (von Bardeleben *et al.*, 1993) and crystalline silicon (Honig, 1961) at liquid helium temperatures.

At low temperatures the thermal energy is insufficient to excite trapped carriers into delocalized states from where they can diffuse to their recombination partners and thus easily recombine. Thus the recombination of charge carriers requires an overlap of their

[2] Note that, although one monitors the *minimum* of a resonance line, the transient signal height shown in Fig. 6.8 is given as a positive signal, i. e. more signal intensity corresponds to higher (more positive) values of the signal height. Experimentally this is simply done by turning the phase angle of the phase-sensitive detection by 180°.

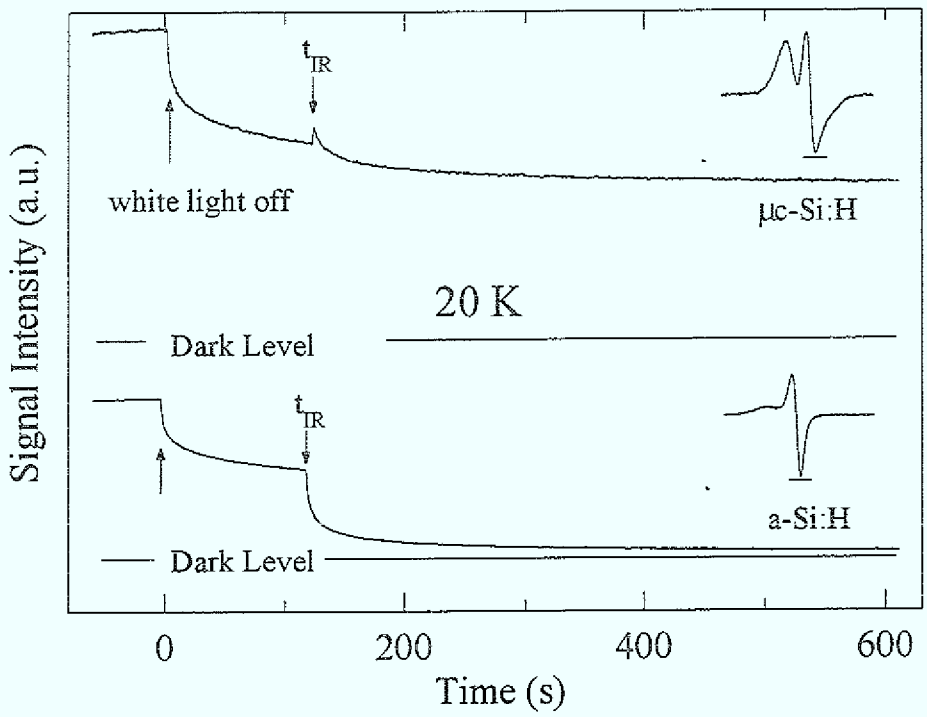

Figure 6.8: LESR transients of a-Si:H and μc-Si:H (sample n1) using a white-light/IR-light sequence (T = 20 K). At time $t = 0$ the white-light illumination is turned off and at t_{IR} samples are re-illuminated with IR-light. The insets on the right-hand side indicate the resonances whose signal height was monitored. The 'dark level' refers to the ESR signal height without any illumination.

respective wave functions and depends exponentially on the distance between electron and hole (see Eq. 3.25, p. 31). A distribution of carrier lifetimes (i. e. in our case: time constants for LESR decay) corresponds to a spatial distribution of electron-hole separations. In an inhomogeneous material like microcrystalline silicon it is additionally possible that pairs get excited into different structural regions and are also separated by potential barriers between these regions.

One has to be aware that there is no simple model for a correct description of the time behaviour of recombination and that a discussion only in terms of pair separations is insufficient. This is easily seen by calculating the average distance between charge carrier pairs say 100 s ($< t_{IR}$) after switching off the initial illumination for sample n1 in Fig. 6.8. The residual light induced CE spin density after 100 s is about 2/3 of the initial value of $2.6 \cdot 10^{16}$ cm^{-3}. Taking this as the density of light induced electron–hole pairs remaining after 100 s yields an average distance of potential recombination partners of $(4\pi/3 \cdot 1.8 \cdot 10^{16}\ \text{cm}^{-3})^{-1/3} \approx 240$ Å. This value is already in the range of the average size

of crystalline domains as discussed in section 2.2, which means that this would actually involve recombination of electrons and holes out of different domains.

These considerations suggest that the strong residual LESR signal and its slow decay after switching off the light source is due — like in amorphous silicon — to a spatial separation of recombination partners. Whether this separation is into different regions of the material and which particular states are involved cannot be decided by looking at the decay alone. To gain more insight one can examine the behaviour under IR illumination as was further done in the experiment illustrated in Fig. 6.8.

6.2.2.2 Re-Illumination with IR Light.

Applying infrared light to the samples after a time t_{IR} during the signal decay (in Fig. 6.8: $t_{IR} = 2$ min.) leads to very different effects in amorphous and microcrystalline silicon. In a-Si:H the IR-light causes the residual signal to be quenched almost down to the dark level. In some cases (like in Fig. 6.8), depending on the dark Fermi-level position, there might remain a small residual signal which can be quenched thermally. The quenching is due to optical re-excitation of trapped carriers out of the localized tail-states so that they can freely diffuse to each other and recombine very fast. At the same time IR-light cannot excite additional carriers from the VB into the CB as its energy ($h\nu < 0.67$ eV) is substantially smaller than the a-Si:H mobility gap of about 1.75 eV.

In microcrystalline silicon IR-light has several distinct effects: initially the LESR signal is enhanced seen as the pronounced 'spike' at t_{IR} in the upper trace of Fig. 6.8. Very soon, however, a quenching effect sets in. In contrast to a-Si:H this does not result in the decay of the signal to the dark level, but the IR-LESR signal approaches a steady-state for long waiting times well *above* the dark level. The relative intensities of (i) the decaying white-light residual signal without IR illumination and (ii) the IR steady-state signal depend on the initial white-light intensity.

The interesting effects of infrared light illumination of μc-Si:H exhibited by the LESR transients in Fig. 6.8 give rise to a number of additional questions:
(i) Does the defect resonance in μc-Si:H show a similar behaviour as the CE line or is there a principal difference?
(ii) Does the appearance of the fast transient at t_{IR} depend on the 'history' of the LESR signal? In particular this means: What happens if the dark/IR-illumination sequence is repeated while the signal is approaching its IR steady-state value? How is the behaviour influenced by variation of the initial white light, e. g. using discrete energies instead of the broad spectrum of the halogen lamp, and is there some kind of threshold energy, especially for the observation of the fast transient?
(iii) Is the steady-state signal level under IR-illumination influenced by the preceding illumination conditions?
(iv) What is the dependence on type of doping and doping level?

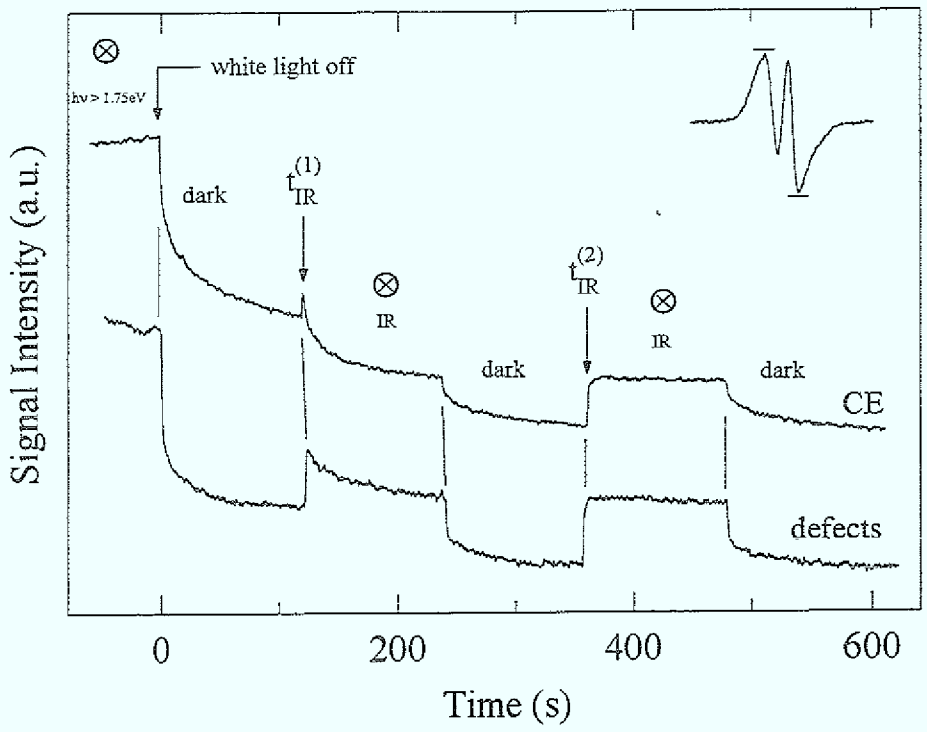

Figure 6.9: LESR transients of CE (upper trace) and defect resonances (lower trace) in μc-Si:H (sample n1) using a repeated dark and illumination sequence. At times $t_{IR}^{(1)}$ and $t_{IR}^{(2)}$ the sample is re-illuminated with IR light. The inset indicates the respective magnetic field positions.

6.2.2.3 CE and Defect Signal – Repeated Illumination/Dark Sequences

The experiment illustrated in Fig. 6.9 addresses question (i) and the first part of question (ii). Here LESR transients of sample n1 are shown similar to Fig. 6.8 but this time including an LESR transient of the defect line (lower trace). The dark level is not included to have a better resolution. The inset marks again the position of the points in the spectra where the magnetic field was fixed. A further difference is that after the first white-light/dark/IR-light sequence (as before) the IR illumination was again switched off, on and off again with respective waiting times of 2 minutes. Two observations have to be emphasized:

Firstly the defect resonances and the CE line show a similar behaviour, i. e. both exhibit the fast transient and approach a non-zero IR-LESR signal value. This suggests that the recombination process reflected by both transients is similar for the defects and the conduction electrons. However, there is obviously a difference in the time constants so that recombination of excited electrons with dangling bond states cannot be the only relevant process.

Secondly it is found that turning off the IR light at $t_{IR}^{(2)}$ after 2 min. causes a further

decay of the signal below the level which would have been reached without the IR light. This means states have been emptied which would have had a longer lifetime in the dark, once more proving that the quenching effect of IR illumination is also present in μc-Si:H. Subsequent IR light causes only an enhancement of the signal to the steady-state IR illumination level with no fast transient observable. Obviously states had been filled by white light incidence, then have been de-populated by IR illumination but cannot be re-filled again with infrared light.

6.2.2.4 Variation of Initial Light Energy

To investigate this further, the energy of the initial light excitation was varied, which corresponds to the second part of question (ii). Instead of illumination with $h\nu > 1.75$ eV different band-pass filters with transmission at 0.95, 0.80 and 0.75 eV were used.

Fig. 6.10 compares the response of the CE line upon initial excitation with energies of $h\nu = 0.75$ eV and $h\nu < 0.67$ eV (Ge filter), respectively, and a subsequent dark and IR illumination sequence. For higher initial light energies (0.80, 0.95 eV) the results are similar. For the initial excitation with $h\nu = 0.75$ eV an interference filter with a bandwidth of 0.05 eV was used. The Ge filter acts as a band-pass at approximately 0.60 eV with a bandwidth of 0.11 eV (see section 4.1, p. 34).

Two observations have to be mentioned. The first is that even with a light energy as low as 0.75 eV (compared to heat-filtered halogen light with $h\nu > 1.75$ eV) the principal signal behaviour upon the initial-light/IR-light sequence does not change. However, a further decrease of light energy changes the signal behaviour: the transient disappears completely if the initial illumination energy is reduced to 0.60 eV.

6.2.2.5 Steady-State IR Levels - Doping Dependence

Before discussing the implications the transient measurements have for the microscopic picture of μc-Si:H, the two remaining questions (iii,iv) will be treated briefly.

CE–Resonance. Figs. 6.11(a)–(c) compare two different illumination sequences in n-type samples with doping levels of 1,2 and 3 ppm. The CE resonance was monitored. The upper trace shows a sequence like in Fig. 6.8, i. e. a steady-state white-light illumination is switched off at t = 0 and samples are re-illuminated with IR light after 2 minutes. The dashed line in Fig. 6.11(a) represents the same experiment with a waiting time of about 30 minutes before the IR light was turned on. In both cases the signal level reaches the same value and still exhibits the fast transient enhancement and quenching effect *independent* of the waiting time between switching off the initial and turning on the infrared light. As the signal (for the dashed trace) has already decayed even below the steady-state IR level, in this case the netto effect of the IR illumination at time t_{IR} is an enhancement. The interpretation of this result is straightforward: During the initial LESR decay electrons excited by white light gradually recombine with their recombination partners. A certain fraction of them occupies states which can only be populated by white light but not by

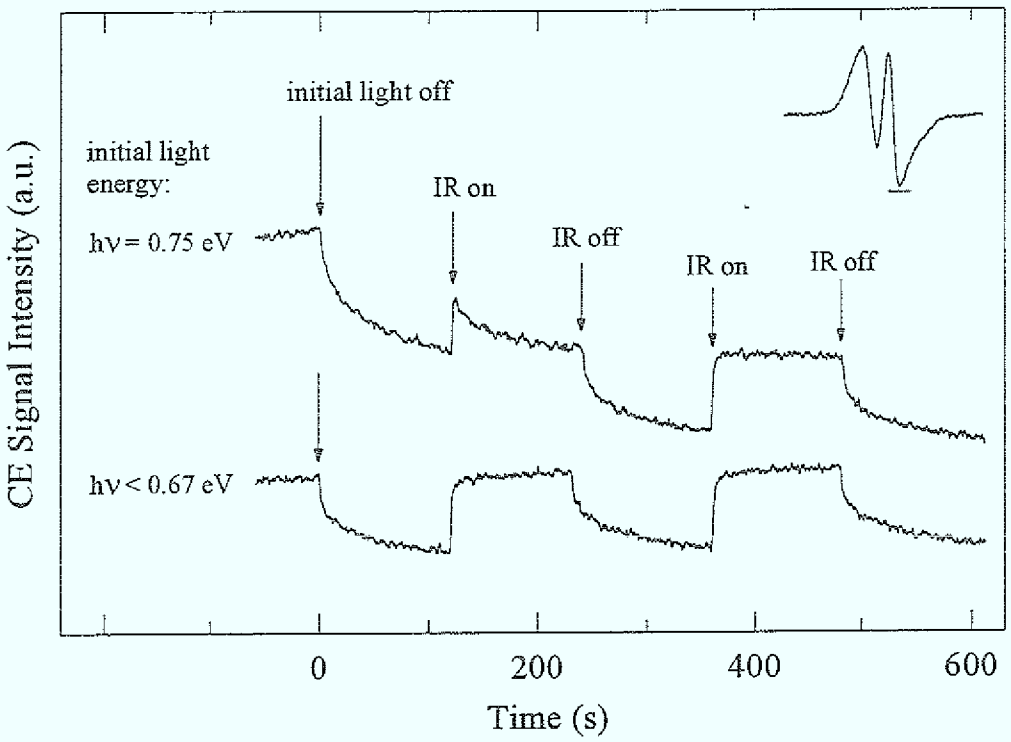

Figure 6.10: LESR transients of the CE resonance in μc-Si:H (sample n1) using a repeated dark and illumination sequence. The difference between both curves is the initial excitation energy indicated on the left-hand side of each trace.

IR illumination. Some of these states have very long lifetimes and are still filled with electrons even after a long waiting time. If IR light is applied after that time these states are emptied and recombine fast causing the same transient as in the case when t_{IR} is much shorter.

The fact that there is no netto quenching effect of the IR light applied at t_{IR} in samples n2 and n3 can be attributed to a reduced lifetime of optically excited electrons with increasing doping level, as was already proposed in section 6.1.

Now one has to consider the lower trace in Figs. 6.11(a)–(c). Here simply the onset of the signal and its approach of the steady state is shown, if IR illumination is turned on at t = 0 starting from the dark level. Independent of doping, the steady-state IR signal intensity without preceding white light in n-type material always remains *below* the intensity reached after an initial white-light/dark sequence.

A similar experiment for p-type samples is shown in Fig. 6.12. Here the initial rise of the white light signal is included, but will not be interpreted here. It exhibits, however, that in fact a situation close to steady-state is already reached after several minutes.

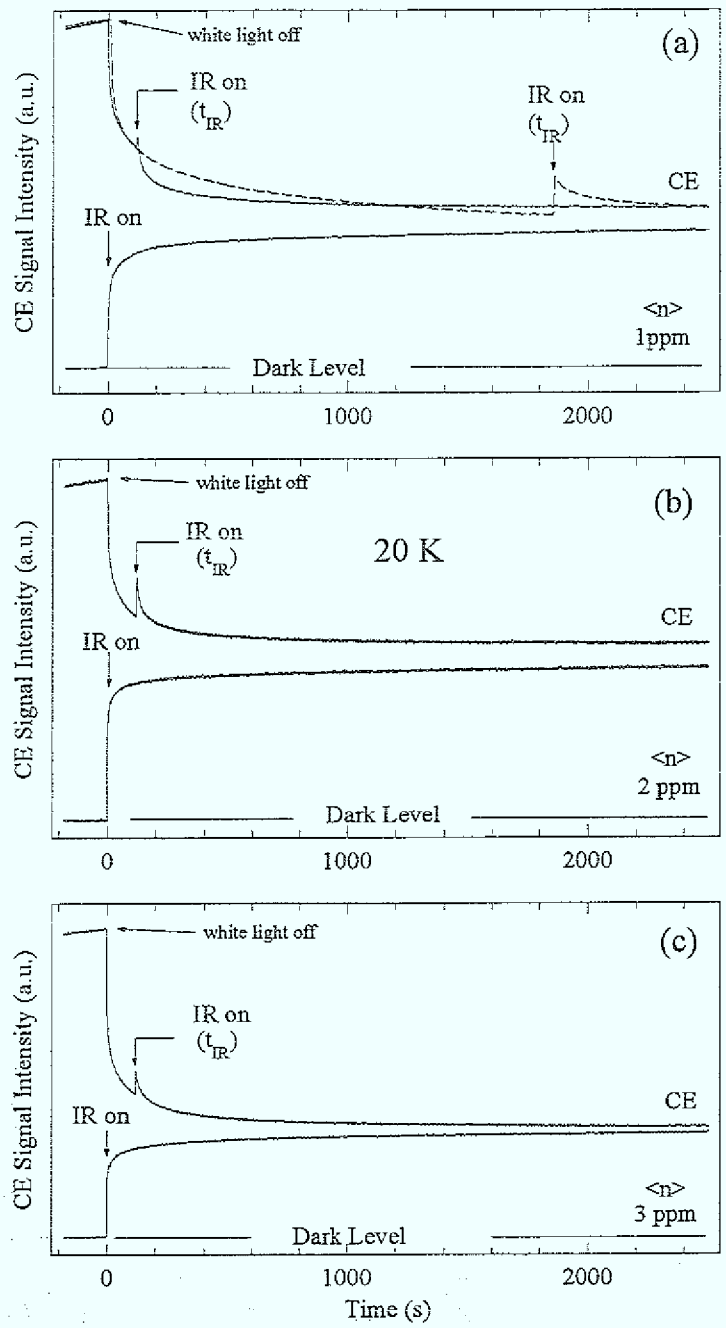

Figure 6.11: LESR transients of the CE line for samples n1 (a), n2 (b) and n3a (c) upon IR illumination with and without preceding white light. Upper traces: At t = 0 the white light is switched off and samples are re-illuminated after time t_{IR} = 120 s. For sample n1 the dashed curve shows the same transient with $t_{IR} \approx 1850$ s. Lower traces: For t < 0 there is no light incident on the samples. At t = 0 IR light is turned on and the IR LESR signal approaches its steady-state level. Note the increased time scale compared to previous figures.

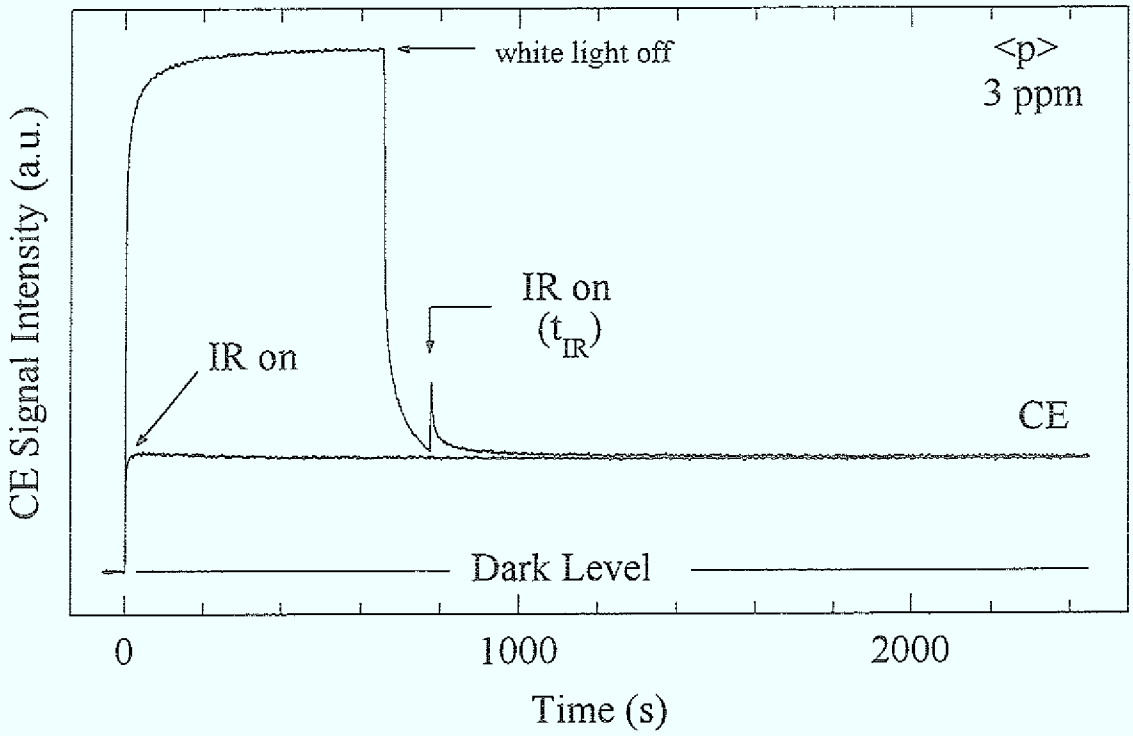

Figure 6.12: LESR transients of the CE line for sample p3 upon IR illumination with and without preceding white light similar to Fig. 6.11. At time t = 0 white light (upper trace) and IR light (lower trace) are turned on.

Fig. 6.12 also monitors the CE resonance, which can still be nicely resolved at this low p-type doping level. The qualitative features observable (non-zero steady-state IR LESR response, superposition of fast transient enhancement and quenching effect at t_{IR}) are similar to n-type samples. In contrast to n-type material, however, the levels reached with IR illumination both with and without preceding white light exactly coincide already within several minutes after t_{IR}.

Defect State Resonances. Fig. 6.13 gives a comparison of the results found for the CE line with the behaviour of the defect resonances. Note that it is mainly the DB line at g = 2.0052 which is monitored according to the results of section 6.1.1 (in particular Fig. 6.4, p. 88). For the uppermost trace in Fig. 6.13 t_{IR} = 30 s was chosen (compared to t_{IR} = 120 s in case of the CE lines), since from Fig. 6.9 it has become clear that the part of the signal which can be quenched by subsequent IR illumination decays faster for the DB line, making the transient IR quenching effect not observable any more for long waiting times. This is also nicely illustrated by the dashed curve in Fig. 6.13: If the sample is re-illuminated with IR light after a waiting time of about half an hour (1850 s), no transient

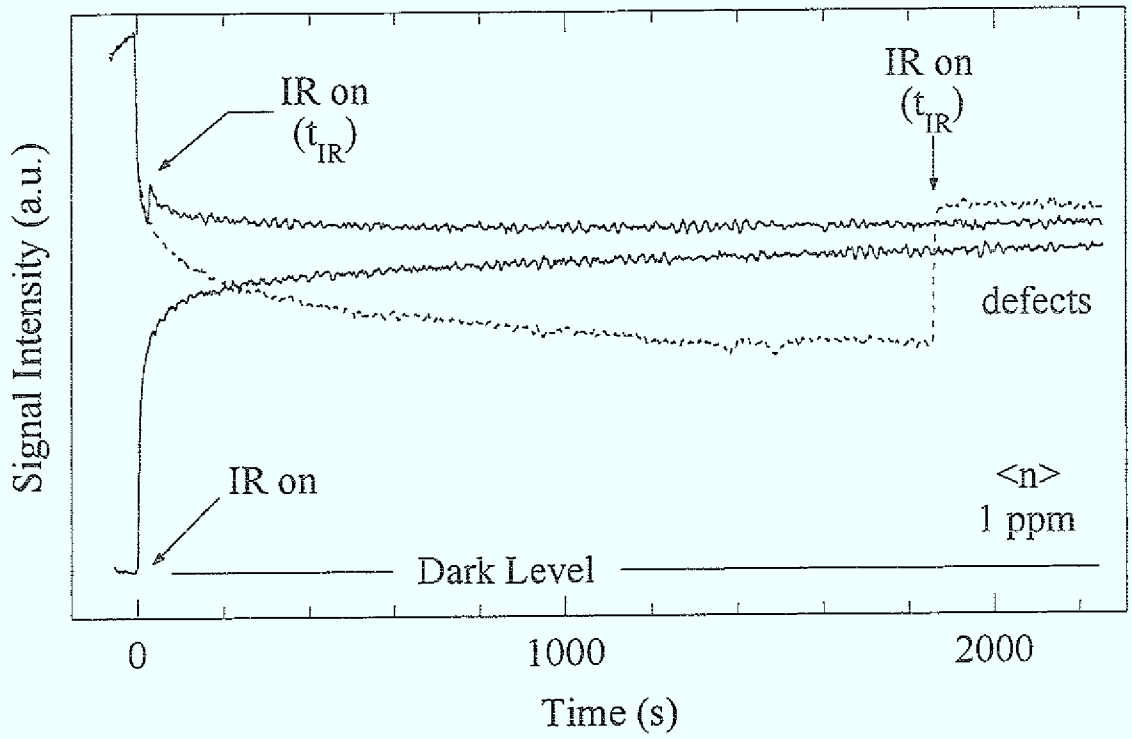

Figure 6.13: LESR transients of the DB line for sample n1 upon IR illumination with and without preceding white light similar to Fig. 6.11(a). Upper traces: At t = 0 the white light is switched off and samples are re-illuminated after times $t_{IR} = 30$ s (solid curve) and $t_{IR} \approx 1850$ s (dashed curve). Lower trace: For t < 0 there is no light incident on the sample. At t = 0 IR light is turned on and the signal approaches its steady-state level.

quenching effect is observed when monitoring the dangling bond resonance.

Generally, the levels reached with the 3 different illumination sequences do not align. The difference in the transients with and without preceding white light is similar to what is observed in case of the CE line and will be interpreted using similar arguments at the end of this section. However, there is no obvious explanation for the difference in the curves obtained with preceding white light. As smaller variations in the signal heights (due to experimental uncertainties like small baseline drifts and time-dependent signal offsets) cannot be excluded when comparing different transients with each other, this difference will not be examined further.

Finally the behaviour of the defect resonance in p-type samples was investigated, and the result is shown in Fig. 6.14. In this case the observed signal exclusively results from the defect line at g = 2.0043, in contrast to n-type samples where g = 2.0052 is enhanced. Two main differences between n- and p-type samples are evident. In the first place the IR LESR

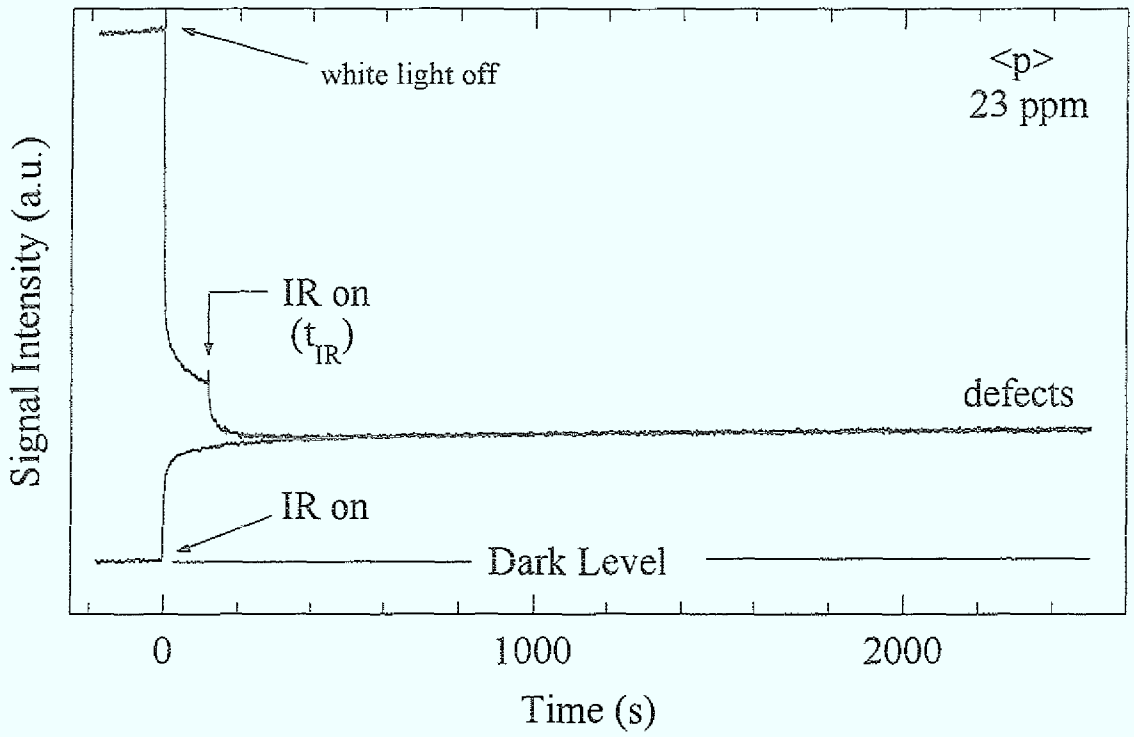

Figure 6.14: LESR transients of the defect line at g =2.0043 for sample p23 upon IR illumination with and without preceding white light similar to Fig. 6.11.

intensity relative to the signal height under white light illumination is appreciably smaller in p-type samples (Fig. 6.14) than in n-type material (Fig. 6.11), i. e. the quenching effect of infrared light is more pronounced than the enhancing effect. Secondly the IR signal levels with and without preceding white light coincide exactly, i. e. are totally independent of the 'history' of the illumination, as has already been observed for the CE line in p-type specimens (Fig. 6.12).

6.2.2.6 Summary

- After illumination with white light ($h\nu > 1.75$ eV) the LESR signal of all resonances decays, as in a-Si:H, with a wide distribution of time constants leaving a residual signal for several hours at T = 20 K. This reflects a large spatial separation of the long-lived recombination partners also including separation into different structural regions of the material.
- Application of infrared light after switching off the initial white light illumination causes both fast transient enhancement and quenching and yields a considerable IR steady-state signal. This is in contrast to a-Si:H where the LESR intensity can almost

completely be quenched by IR light and is evidence for an excitation process within the crystalline regions of μc-Si:H.

- The effects are similar for defect and conduction electron states suggesting recombination processes which involve both kinds of states. This is in accordance with EDMR and ODMR results. However, the time constants of LESR decay for the respective resonances are different pointing to the simultaneous presence of alternative recombination mechanisms.

- The fast transients occur only after illumination with light of energy > 0.67 eV, the threshold energy lying between 0.67 eV and 0.75 eV. This means IR light induces recombination of charge carriers which cannot be excited again by infrared illumination.

- Comparison of the IR steady-state levels with and without preceding white light yields different results for n- and p-type samples: Whereas in n-doped material the signal level without initial white light illumination remains below the one with preceding white light, the same level is reached in p-type samples. In other words, the steady-state signal level under infrared illumination in n-type μc-Si:H depends on the 'history' of the sample. Obviously in n-type material white light populates states deep enough so that they cannot be emptied by IR illumination. Such deep traps do not exist in p-type material.

6.2.3 A Simple Band Diagram

From the LESR results presented so far, microcrystalline silicon appears as a material where different excitation and recombination processes play together to determine the light induced properties in a quite complicated manner, leading to the observed effects in the steady-state and transient data. The problem of the location and identification of the states responsible for the *CE line* was resolved satisfactorily in chapter 5. Unfortunately the exact location of the defect states can only be speculated on, even though their energy position was estimated from the doping dependence of the ESR signals. Probably a large fraction of the defects is located at the boundaries between adjacent columnar grains.

At this point it is therefore not possible to develop a quantitative model for the description of carrier recombination processes in μc-Si:H. Instead, the experimental results (especially of the transient measurements) will be interpreted in a qualitative band diagram of microcrystalline silicon which can serve to explain a number of important observations described in the preceding sections. Due to the unknown location of the defects and to avoid too much complexity (which inherently involves the danger of loosing sight of the important features) the presence of two distinct defect resonances was neglected.

One obviously has to distinguish between electronic states which can be populated by IR light ($h\nu < 0.67$ ev) and states which cannot. Two experimental findings support this assumption: Firstly, in n-type material the IR steady state level without preceding white light never reaches the signal height obtained after initial white light illumination.

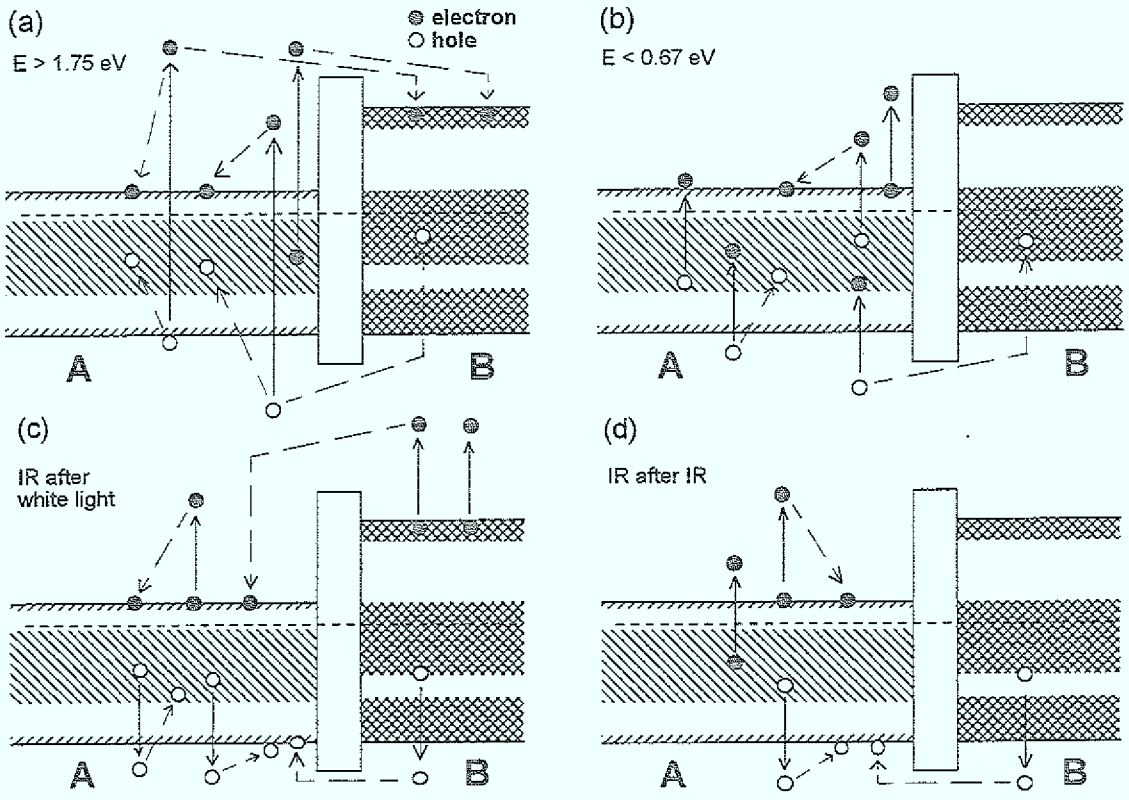

Figure 6.15: Simple band diagram describing the illumination sequences white-light/IR-light (a,c) and IR-light/IR-light (b,d). Letters A and B refer to crystalline and amorphous/grain-boundary regions, respectively.

Secondly, the form of the 'spike', which occurs when the IR light is turned on during an LESR decay, suggests that it consists of a superposition of a fast enhancement and a slower quenching effect (best visible for long waiting times; see dashed curve in Fig. 6.11(a)). If one now assumes that IR light populates the same states as bandgap light, it should be expected that a similar transient behaviour (fast enhancement + quenching) is found if IR light is applied during the decay of a purely *infrared* LESR signal. This is, however, not observed as shown in Fig. 6.10.

Figs. 6.15(a) and (c) describe the white light/IR light illumination sequence shown in Fig. 6.8 (upper curve, μc-Si:H) whereas Figs. 6.15(b) and (d) refer to an experiment like in Fig. 6.10 (lower curve) where only IR light is employed. They are drawn for an n-type sample (like n1) with the position of the Fermi level in the upper half of the gap in the crystalline regions. The parts denoted A and B refer to the crystalline grain columns and to amorphous and grain boundary regions, respectively. In the crystalline areas the crystalline silicon bandgap of 1.1 eV is used whereas in the amorphous part the mobility

gap is 1.75 eV like in a-Si:H. In addition both regions contain CB- and VB-tail states, and there is a wide distribution of defect states within the energy gaps. For the band offset between both regions several contradictory reports exist (see for example Lucovsky *et al.*, 1993; Grebner *et al.*, 1993; Xu *et al.*, 1995; Kolter, 1997). The fact that in p-type samples the equilibrium spin density of defects decreases for doping levels higher than 7 ppm (Fig. 5.4, p. 44) whereas it is almost constant in case of n-type doping suggests an offset in the conduction band. This would allow defect states in the amorphous/grain boundary regions to be singly occupied even for positions of the Fermi level close to the CB of the crystallites and hence a CB offset was chosen in Fig. 6.15. Furthermore regions A and B are separated from each other by a potential barrier. Excitation of charge carriers mainly takes place in the crystallites or from their grain boundaries. This directly follows from the strong IR LESR signal, as in the amorphous parts IR light would solely cause a quenching effect (Fig. 6.8, lower curve, a-Si:H).

Figs. 6.15(a) and (b) describe the processes during the initial illumination of the sample with white light (a) and IR light (b). In both cases the illumination can excite electrons or holes out of band tails or defect states within the gap, making transitions like $D^{-/0} \longrightarrow D^{0/+} + e^{-}(CB)$ or $D^{+/0} \longrightarrow D^{0/-} + h^{+}(VB)$. In case (a) with white light illumination band-to-band excitations are the dominant process, and additionally carriers have enough excess energy to be excited over the top of the barrier and get trapped in region B. This is impossible with infrared light according to Fig. 6.10 with a threshold energy between 0.67 eV and 0.75 eV.

After switching off the initial illumination carriers begin to recombine. Some of them, however, are far apart from each other or even separated by the potential barriers so that the recombination lifetimes can be as long as several hours. Applying IR light after the time t_{IR} (Figs. 6.15(c) and (d)) now has very different effects depending on the preceding illumination: In case (c) the IR light can re-emit trapped carriers from region B, increasing the electron concentration, and excite more carriers out of defect states in region A (thus also creating more D^0 states and also increasing the defect signal intensity). This, of course, only gives an enhancement signal on a short time scale, and the increased number of free electrons and holes, which have been freed from their traps, will soon increase the recombination rate and lead to a quenching effect. Once the carriers have been emitted out of their traps, IR light cannot fill them again as its energy is insufficient for the electrons and holes to cross the potential barriers. Thus the distinct 'spike' in the transients appears only once.

Doping Dependence. In n-type samples the IR steady-state level depends on the 'history' of the sample, i. e. is different with and without preceding white light illumination. The non-coincidence of both signal levels can be attributed to trapping of electrons or holes in states that cannot be de-populated by infrared light. Obviously such deep traps do not exist in p-type material.

To prevent re-excitation of charge carriers out of these deep traps by IR light they have to lie deeper in the gap than 0.67 eV (the maximum IR light energy) or be separated from their recombination partners by a potential barrier higher than 0.67 eV. The former case

can only be realized with states located within disordered regions as evidently a bandgap is required which allows for states being farther than 0.67 eV away from *both* band edges.

If electrons occupied such deep-lying defects this would, of course, mean that the electrons get lost for the CE line. Therefore, explaining the above result looking only at the electrons requires that these in fact occupy conduction band or tail states in crystalline regions after excitation, but are 'protected' from re-excitation (into regions where they 'find' holes to recombine) and subsequent recombination via IR light by a high potential barrier.

As a more likely possibility one can imagine that it is not the electrons themselves, but the holes as their recombination partners which get deeply trapped after white light illumination. In n-type samples this would lead to a reduced recombination probability for electrons (as part of their recombination partners are missing) and thus also increase the residual CE signal after white light. It can also explain why the difference in steady-state IR LESR levels shows up in n-type samples, but is missing in p-doped specimens: Only in n-type material there will be a sufficient number of D^0- and D^--states which can capture holes and are far away from the valence band edge, whereas in p-type material most of the defects are positively charged D^+-states with a small capture cross section for an additional positively charged hole. Assuming such a mechanism, one would expect a decrease in the number of holes in valence band or valence band tail states. Unfortunately this cannot be checked, as holes are not observable with the CW-ESR techniques employed.

Remarks. It has to be emphasized that for a number of reasons the model of Fig. 6.15 cannot be the whole truth. In particular such a picture is only valid for a certain fraction of the material, as generally high potential barriers between adjacent regions are in contrast to the high conductivities observed, and regions with lower or negligible potential barriers are required to allow for a sufficient number of percolation paths. However, a limited number of potential barriers within the material is in accordance with experimental data, as electrons or holes can by-pass high barriers. Furthermore, it is recalled that the fraction of disordered areas within the microcrystalline material studied comprises less than 10% of the sample volume. Thus the regions denoted as B in Fig. 6.15 have to be mostly understood as disordered grain boundary regions rather than extended amorphous areas, although considerable amounts of amorphous tissue always exist close to the interface between material and substrate (as seen in the TEM-image on page 10). For a complete discussion one finally has to include the presence of potential fluctuations between neighbouring regions.

A number of experimental findings in light induced steady state or transient ESR cannot be explained in detail on the basis of the data available at this point, but the model of Fig. 6.15 can qualitatively describe some of the important features and serve as a good starting point for future discussions.

Chapter 7

Summary

In the present work the electronic properties of VHF-PECVD grown micro-crystalline silicon with various amounts of n- and p-type doping were studied in a systematic way employing continuous wave electron spin resonance in the temperature range between 4.2 and 300 K. The comparison with crystalline and amorphous silicon was made whenever it turned out to be helpful in interpreting and understanding the experimental data. Microscopic information was obtained about the nature and energy position of defect and dopant-related (conduction electron) states as well as their interplay in recombination processes. Note that, like in crystalline silicon, no resonances of hole states could be observed. The most important results are summarized in the following.

Two different kinds of defect states are observed in μc-Si:H which are located in different structural environments. A resonance at g = 2.0052 is due to Si dangling bond states, while a line at g = 2.0043 probably originates from dangling bond defects in Si-O layers due to incorporated oxygen. It is likely that defects are preferably located along grain boundaries but there is no conclusive proof for such an assumption.

Defect states in μc-Si:H are observed over a large doping range. This is indicative of either a wide distribution in energy (0.6 eV) or considerable potential fluctuations throughout the material. The energy distribution is somewhat flatter for the DB resonance with g = 2.0052, but in the dark they are both centered at the same energy position. Their temperature independent spin density (equivalent to a decrease of the ESR signal intensity proportional to 1/T) points to a relatively large effective correlation energy similar to a-Si:H or polycrystalline Si. Using U_{eff} = 0.3 eV the density of defect states within the energy gap of μc-Si:H can be estimated to be below 10^{17} cm^{-3}eV^{-1}.

Both resonances are enhanced under light illumination, but doping has a significant influence: While in n-type samples only the spin density of the resonance at g = 2.0052 is increased, in p-type material light illumination enhances the line at g = 2.0043.

A third contribution to the ESR spectra, appearing in n-type and some intrinsic samples or under light illumination, is referred to as conduction electron (CE) resonance and occurs at g-values between 1.9972 and 1.9985. The g-values decrease both with

temperature and doping level. The values are slightly but distinctly lower than for the resonance of electrons located at donor sites or conduction band electrons in phosphorus-doped crystalline silicon. The CE line in μc-Si:H has to be attributed to different electronic states depending on temperature and phosphorus concentration.

For an unambiguous identification ESR results were compared with temperature dependent conductivity measurements between 4.2 and 300 K. At higher temperatures transport cannot be described by a single activation energy. Here the conduction process is understood in terms of a percolation model where carriers move in an interconnected network with variable barrier heights between adjacent regions. At low T transport proceeds via hopping between neutral and ionized donors similar to the low-temperature conduction mechanism observed in n-type crystalline silicon. This kind of transport is characterized by one single activation energy of the order of several meV. In microcrystalline silicon 3.5 meV are found.

The combination of ESR and transport data together with additional information from SIMS and Hall effect measurements yields the following picture for the conduction electron resonance in n-type μc-Si:H:

During deposition the phosphorus dopants are incorporated into the solid with a build-in ratio of P to Si of 0.5. Their doping efficiency is unity like in crystalline silicon. At low temperatures the electrons introduced by the doping process are either localized at their donor sites or occupy conduction band tail states within the crystalline grains. The ESR spin density deduced from the CE resonance is *equal* to the donor density. With rising temperature an increasing number of electrons is excited into delocalized conduction band states, but at any temperature the charge carriers are non-degenerate for the doping range investigated. The electrons in the conduction band are still observable with ESR, but the transition to delocalized states is accompanied by appreciable line broadening and a slight decrease in g-value. The ESR signal intensity decreases according to the Curie law in the whole temperature range. However, slight deviations for some of the samples might indicate a partial excitation into states with weaker ESR response.

The strong line broadening of the CE line at high temperatures results from a decrease in spin-lattice relaxation time as measured by pulsed ESR. A distinct minimum around T = 30 K in the linewidth of highly n-doped samples is explained, like in crystalline silicon, with incomplete exchange narrowing at the lowest temperatures.

Interestingly hyperfine interaction of donor electrons with phosphorus nuclei is only observable at intermediate doping levels. From the value of the hyperfine splitting a localization length of 12 Å is estimated for the donor wavefunction which is between the values found in crystalline (16.7 Å) and amorphous (10 Å) silicon. The absence of visible hyperfine interaction for the highest doping levels is in accordance with observations in crystalline silicon. It is explained by donor clustering and averaging of the hyperfine interaction as a result of the hopping motion of electrons between phosphorus donors. Although clustering effects possibly also play a role, the main reason for the lack of

hyperfine interaction at *low* doping levels (in contrast to c-Si) is the occupancy of conduction band tail states.

Under light illumination the CE resonance is enhanced in both n- and p-doped specimens for low doping levels, but no light induced increase of the CE spin density is observed for higher dopant concentrations irrespective of type of doping. This is a result of the decreasing lifetime of optically excited charge carriers and agrees qualitatively with photoconductivity measurements where the ratio of photo- to dark conductivity σ_{ph}/σ_d also decreases with doping. The LESR signal is governed by the long-lived charge carrier pairs (like in a-Si) and the recombination process is non-geminate. The lifetimes deduced from photoconductivity measurements are much shorter and both techniques reflect different parts out of a broad distribution.

This broad distribution of recombination lifetimes is also seen in the time decay of the light induced ESR signals after turning off the illumination, which yields values of several hours for the longest-lived pairs. This reflects a large separation of recombination partners, in particular including separation into different structural regions of the material.

A distinct difference between the LESR behaviour of amorphous and microcrystalline silicon appears upon illumination with infrared ($h\nu < 0.67$ eV) instead of 'white' ($h\nu > 1.75$ *eV*) light. Whereas no IR LESR signal is observed in amorphous silicon, in microcrystalline silicon infrared light can excite charge carriers out of deep defect states thus yielding a considerable light induced signal enhancement. This points to an excitation process within the crystalline regions where the bandgap is taken as that of crystalline silicon (1.1 eV). From the similar behaviour of defect and CE resonances upon various dark and illumination sequences it is concluded that recombination of photoexcited electrons via dangling bonds is one dominant process in accordance with ODMR and EDMR literature data.

Dark/illumination sequences employing white and infrared light strongly suggest the existence of states in μc-Si:H which can be emptied by IR light but populated only by using light of higher energy. In n-type samples a fraction of them lies deep enough so that they cannot even be emptied by IR illumination.

A number of transient ESR results can be satisfactorily explained in a model where such states exist in disordered regions (where the mobility gap of amorphous silicon, 1.75 eV, is assumed) and are separated from neighbouring crystalline grains by potential barriers. Keeping in mind the high conductivities and the low amorphous volume fraction in the μc-Si:H material used, it is emphasized that this picture can only be valid in certain regions. In general excitation and recombination in μc-Si:H involves different structural environments. Consequently the processes occuring are very complex, and for a detailed description the structural inhomogeneities and the transfer of charge carriers between different regions have to be taken into account.

Due to the complex nature of the material the discussion had to remain qualitative at some points and might stimulate future, more quantitative work. This includes mainly the extension of ESR work on powder samples to thin films where possible, thus permitting light induced ESR experiments under well-defined illumination conditions. In conjunction with additional optical measurements like transient photoluminescence and optically detected magnetic resonance (ODMR) – the latter being already under way – this should finally lead to a more quantitative understanding of recombination mechanisms.

In conclusion the present work fulfills two purposes. On the one hand, it provides detailed results on defect and conduction electron states in microcrystalline silicon. The energy positions and the densities of these states were determined and the origin of the CE resonance was clarified as a function of doping and temperature. Additional information was obtained on recombination processes, and the sum of the data presented gives valuable insights on the way towards an understanding of this complex material.

Secondly, it is emphasized once again that ESR has the great advantage of being a *microscopic* probe and provides a very specific and accurate way of characterization. In its simplest form this means detailed information on defect and, as shown in this work, donor densities. With many fundamental problems of data analysis and interpretation having been resolved in the present study, ESR might at least get a little bit closer to becoming an 'every-day technique' for the characterization of microcrystalline materials and hence contribute to the improvement of devices like microcrystalline thin film solar cells.

Appendix A

The Calculation of Spin Densities

As mentioned in section 4.1 spin densities were calculated by comparison with a sputtered amorphous silicon sample ($1.6 \cdot 10^{15}$ spins) as a secondary standard. If A_{sample} and $A_{standard}$ denote the respective areas under the absorption curves and V_{sample} is the sample volume, the spin density N_s is given by

$$\begin{aligned} N_s\,[cm^{-3}] &= \left.\frac{A_{sample}}{A_{standard}}\right|_{corr} \cdot \frac{1}{V_{sample}} \cdot (\#of spins)_{standard} \\ &= \left.\frac{A_{sample}}{A_{standard}}\right|_{corr} \cdot \frac{\rho}{m_{sample}} \cdot 1.6 \cdot 10^{15} \\ &= 3.6 \cdot 10^{18} \cdot \left.\frac{A_{sample}}{A_{standard}}\right|_{corr} \cdot \frac{1}{m_{sample}(mg)}\,[cm^{-3}] \end{aligned} \tag{A.1}$$

where $\rho = 2250$ mg/cm^3 is the mass density of silicon and m_{sample} the mass of the powder sample in mg. The subscript '*corr*' in Eq. A.1 indicates that for the formula to be applicable in this simple form one has to use the absorption curve areas corrected by a number of parameters. This will be outlined briefly in the following.

Calculating the area under the absorption curve means an integration and is equivalent to a double integration over the absorption derivative as obtained in an ESR experiment. Denoting the absorption derivative (ESR signal) and the absorption curve itself by $y'(\omega, B)$ and $y(\omega, B)$, respectively, yields y as a function of the magnetic field B with a constant microwave frequency ω (see e. g. Connell and Pawlik, 1976)

$$\begin{aligned} y(\omega, B) &= \int_0^B y'(\omega, B')dB' \\ \Longrightarrow area\ A &= \int_0^\infty y(\omega, B)dB \\ &= K\sqrt{P_{mw}}\,Q B_0 \eta V \chi_0 \\ \text{where}\quad \chi_0 &\propto \frac{N_s}{T} \quad \text{(according to Eq. 3.12)} \end{aligned} \tag{A.2}$$

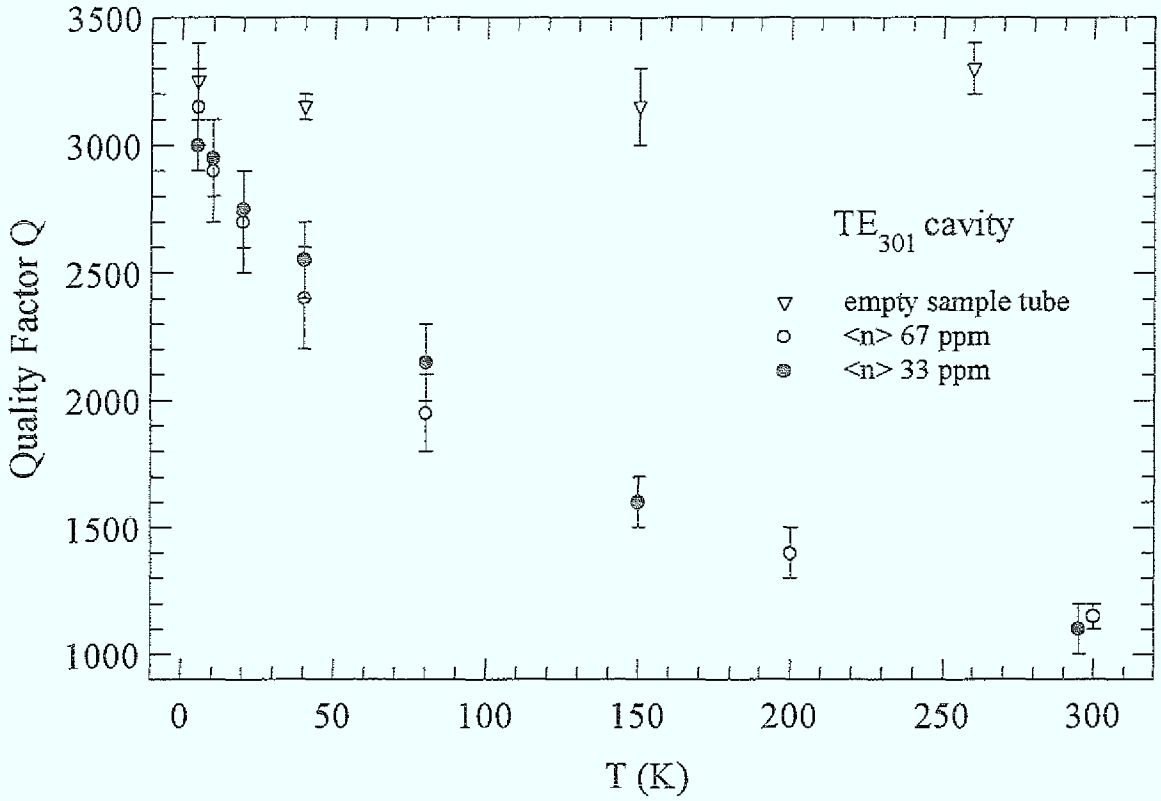

Figure A.1: Temperature dependence of the cavity quality factor Q for samples n33, n67 and an empty sample tube between 5 K and room temperature. At low T the values of Q coincide.

In Eq. A.2 K includes a number of spectrometer parameters and a numerical factor, P_{mw} is the microwave power incident on the cavity (provided the detector is operating in its linear range), Q is the quality factor of the cavity (with sample) when the sample is not at resonance, B_0 is the magnetic field at the center of the resonance line (maximum absorption), η is related to the cavity filling factor and assumed to be independent of the specific sample, V stands for the sample volume and χ_0 is the static magnetic susceptibility, which is proportional to N_s and inversely proportional to T in case of Curie-like behaviour (see Eq. 3.12, section 3.1.3.1).

The factor K incorporates modulation amplitude, conversion time and receiver gain of the spectrometer, number of scans and finally the number of points taken for one spectrum as well as the sweep width of the magnetic field scan, since the numerical integration is a summation over all data points.

The so-called quality factor Q of the resonant cavity needs some further attention. It is defined as the ratio between the energy stored in the resonant cavity and the dissipated

energy per cycle (Poole, Jr., 1982, p. 125), i. e.

$$Q = 2\pi \frac{\text{energy stored}}{\text{energy dissipated per cycle}} \tag{A.3}$$

As long as the dielectric losses inside the cavity resulting from the presence of the sample can be neglected, Q is essentially independent of temperature or the specific nature of a sample. However, if samples are very lossy, the quality factor decreases significantly, and this decrease has to be taken into account when comparing intensities or calculating spin densities. This was for example the case for highly doped n-type μc-Si:H samples (section 5.1.3.4) where the conductivity increases strongly with T thus leading to a significant deterioration in Q.

An approximate value for Q can be obtained using a numerical procedure which analyses the tuning mode pattern of the clystron microwave source. The results for samples n33, n67 and an empty sample tube for comparison are shown as a function of temperature in Fig. A.1 (TE_{301} cavity). At low T the values of Q coincide and are around $Q = 3100$. Increasing the temperature results in a strong decrease in Q due to the increasing conductivity in case of the n-type samples, whereas the quality factor of the cavity without sample does not change.

The results of Fig. A.1 were used to correct the temperature dependent ESR intensities shown in Fig. 5.18, section 5.1.3.4 by dividing the areas obtained from numerical integrations by the quality factor Q (taking account of the other experimental factors in Eq. A.2).

Bibliography

F. R. Allen and C. J. Adkins (1972), Electrical conduction in heavily doped germanium, *Philosophical Magazine* **26**, 1027.

P. W. Anderson (1954), A mathematical model for the narrowing of spectral lines by exchange or motion, *Journal of the Physical Society of Japan* **9**(3), 316.

P. W. Anderson and P. R. Weiss (1953), Exchange narrowing in paramagnetic resonance, *Reviews of Modern Physics* **25**(1), 269.

N. M. Atherton (1993), *Principles of Electron Spin Resonance*, Ellis Horwood, PTR Prentice Hall, Chichester.

K. R. Atkins, R. Donovan, and R. H. Walmsley (1960), Low-temperature impurity conduction in n-type silicon, *Physical Review* **118**(2), 411.

G. Baccarani, B. Riccò, and G. Spadini (1978), Transport properties of polycrystalline silicon films, *Journal of Applied Physics* **49**(11), 5565.

U. Backhausen (1996), *Elektrischer Transport in mikrokristallinen Siliziumschichten*, Diplomarbeit, Universität Köln.

U. Backhausen, R. Carius, F. Finger, P. Hapke, U. Zastrow, and H. Wagner (1997), Hall-effect studies on microcrystalline silicon with different structural composition and doping, *Materials Research Society Symposium Proceedings* **452**, 833.

D. Ballutaud, M. Aucouturier, and F. Babonneau (1986), Electron spin resonance study of hydrogenation effects in polycrystalline silicon, *Applied Physics Letters* **49**(23), 1620.

E. Becquerel (1839), Mémoire sur les effets électriques produits sous l'influence des rayons solaires, *C. R. Acad. Sci. Paris* **9**, 561.

D. K. Biegelsen and M. Stutzmann (1986), Hyperfine studies of dangling bonds in silicon, *Physical Review B* **33**(5), 3006.

F. Bloch (1946), Nuclear Induction, *Physical Review* **70**, 460.

K. W. Böer (1990), *Survey of Semiconductor Physics*, Van Nostrand Reinhold, New York.

J. C. Bourgoin, G. Frossati, A. Ravex, D. Thoulouze, M. Vandorpe, and B. Waksmann (1979), Conduction at low temperature in ion-implanted silicon, *physica status solidi (b)* **92**, 585.

R. Carius (1986), *Rekombination in amorphem Silizium*, Ph.D. thesis, Philipps-Universität Marburg, Marburg/Lahn.

R. Carius (1998), private communication.

R. Carius, F. Finger, U. Backhausen, M. Luysberg, P. Hapke, L. Houben, M. Otte, and H. Overhof (1997a), Electronic properties of microcrystalline silicon, *Materials Research Society Symposium Proceedings* **467**, 283.

R. Carius, F. Finger, M. Luysberg, P. Hapke, and U. Backhausen (1997b), Microcrystalline silicon II: Electrical and optical properties, in: J. M. Marshall, N. Kirov, A. Vavrek, and J. M. Maud (eds.), *Future Directions in Thin Film Science and Technology*, pp. 11–22, World Scientific, Singapore.

D. E. Carlson and C. R. Wronski (1976), Amorphous silicon solar cell, *Applied Physics Letters* **28**(11), 671.

B. N. Chapman (1980), *Glow Discharge Processes*, John Wiley & Sons, New York.

J. A. Chroboczek (1987), Impurity conduction in semiconductors, in: M. Pollack (ed.), *Noncrystalline Semiconductors Vol. III*, chap. 4, p. 109, CRC Press Inc., Boca Raton, Fl.

G. Connell and J. Pawlik (1976), Use of hydrogenation in structural and electronic studies of gap states in amorphous germanium, *Physical Review B* **13**(2), 787.

E. M. Conwell (1956), Impurity band conduction in germanium and silicon, *Physical Review* **103**(1), 51.

P. R. Cullis and J. R. Marko (1975), Electron paramagnetic resonance properties of n-type silicon in the intermediate impurity concentration range, *Physical Review B* **11**(11), 4184.

S. P. Depinna, K. Homewood, B. C. Cavenett, I. G. Austin, T. M. Searle, G. Willeke, and S. Kinmond (1983), O.D.M.R. investigation of recombination in μc-Si:H, *Philosophical Magazine B* **47**(5), L57.

J. Dubois, G. Willeke, K. Prasad, O. Blenk, A. Shah, and E. Bucher (1992), Hall effect studies on VHF-prepared gdμc-Si thin films, in: *Proceedings of the 11th E.C. Photovoltaic Solar Energy Conference*, p. 718, Montreux.

F. J. Dyson (1955), Electron Spin Resonance Absorption in Metals. II. Theory of Electron Diffusion and the Skin Effect, *Physical Review* **98**(2), 349.

A. L. Efros, B. I. Shklovskii, and I. Y. Yanchev (1972), Impurity conductivity in low compensated semiconductors, *physica status solidi (b)* **50**, 45.

T. Ehara (1997), Electron spin resonance study of nitrogen-doped microcrystalline silicon and amorphous silicon, *Applied Surface Science* **113/114**, 126.

G. Feher (1959), Electron spin resonance experiments on donors in silicon. I. Electronic structure of donors by the electron nuclear double resonance technique, *Physical Review* **114**(5), 1219.

G. FEHER AND R. FLETCHER (1956), Relaxation effects in donor spin resonance experiments in silicon, *Bulletin of the American Physical Society* **1**, 125.

G. FEHER AND E. GERE (1959), Electron spin resonance experiments on donors in silicon, *Physical Review* **114**(5), 1245.

G. FEHER AND A. KIP (1955), Electron spin resonance absorption in metals. I. Experimental, *Physical Review* **98**(2), 337.

G. FEHER, R. C. FLETCHER, AND E. A. GERE (1955), Exchange effects in spin resonance of impurity atoms in Si, *Physical Review* **100**(6), 1784.

G. FEHER, J. C. HENSEL, AND E. A. GERE (1960), Paramagnetic resonance absorption from acceptors in silicon, *Physical Review Letters* **5**(7), 309.

E. FERMI (1930), Über die magnetischen Momente der Atomkerne, *Zeitschrift für Physik* **60**, 320.

F. FINGER, R. CARIUS, P. HAPKE, K. PRASAD, AND R. FLÜCKIGER (1993), Microcrystalline silicon prepared by VHF-GD: Structure, transport and optical properties, *Materials Research Society Symposium Proceedings* **283**, 471.

F. FINGER, P. HAPKE, M. LUYSBERG, R. CARIUS, H. WAGNER, AND M. SCHEIB (1994a), Improvement of grain size and deposition rate of microcrystalline silicon by use of very high frequency glow discharge, *Applied Physics Letters* **65**(20), 2588.

F. FINGER, C. MALTEN, P. HAPKE, R. CARIUS, R. FLÜCKIGER, AND H. WAGNER (1994b), Free electrons and defects in microcrystalline silicon studied by electron spin resonance, *Philosophical Magazine Letters* **70**(4), 247.

F. FINGER, R. CARIUS, P. HAPKE, L. HOUBEN, M. LUYSBERG, AND M. TZOLOV (1997a), Growth and structure of microcrystalline silicon prepared with glow discharge at various plasma excitation frequencies, *Materials Research Society Symposium Proceedings* **452**, 725.

F. FINGER, R. CARIUS, P. HAPKE, M. LUYSBERG, AND M. TZOLOV (1997b), Microcrystalline silicon I: Growth and structural properties, in: J. M. Marshall, N. Kirov, A. Vavrek, and J. M. Maud (eds.), *Future Directions in Thin Film Science and Technology*, pp. 1–10, World Scientific, Singapore.

F. FINGER, J. MÜLLER, C. MALTEN, AND H. WAGNER (1998), Electronic states in microcrystalline silicon, *Philosophical Magazine B* **77**(3), 805.

R. C. FLETCHER, W. A. YAGER, G. L. PEARSON, A. N. HOLDEN, W. T. READ, AND F. R. MERRIT (1954a), Spin resonance of donors in silicon, *Physical Review* **94**, 1392.

R. C. FLETCHER, W. A. YAGER, G. L. PEARSON, AND F. R. MERRIT (1954b), Hyperfine splitting in spin resonance of group V donors in silicon, *Physical Review* **95**, 844.

S. GREBNER, F. WANG, AND R. SCHWARZ (1993), Carrier transport through grain boundaries in hydrogenated microcrystalline silicon, *Materials Research Society Symposium Proceedings* **283**, 513.

D. L. Griscom, F. J. Friebele, and G. H. Sigel, Jr. (1974), Observation and analysis of the primary ^{29}Si hyperfine structure of the E' center in non-crystalline SiO_2, *Solid State Communications* **15**, 479.

P. Hapke (1995), *VHF-Plasmaabscheidung von mikrokristallinem Silizium (μc-Si): Einfluß der Plasmaanregungsfrequenz auf die strukturellen und elektrischen Eigenschaften*, Ph.D. thesis, Rheinisch-Westfälische Technische Hochschule Aachen.

P. Hapke, U. Backhausen, R. Carius, F. Finger, and S. Ray (1996), Modulated Hall-effect techniques for the study of transport properties of microcrystalline silicon with different grain sizes, *Materials Research Society Symposium Proceedings* **420**, 789.

N. Harder (1998), private communication.

S. Hasegawa, T. Kasajima, and T. Shimizu (1979), Electrical activation process of phosphorous atoms with annealing for doped CVD poly-Si, *Journal of Applied Physics* **50**(11), 7256.

S. Hasegawa, S. Takenaka, and Y. Kurata (1982), Plasma-hydrogenation effects on conductivity and electron spin resonance in undoped polycrystalline silicon, *Journal of Applied Physics* **53**(7), 5022.

S. Hasegawa, S. Narikawa, and Y. Kurata (1983a), Dependences of ESR and electrical properties on P doping ratio for microcrystalline silicon, *Physica* **117B & 118B**, 914.

S. Hasegawa, S. Narikawa, and Y. Kurata (1983b), ESR and electrical properties of P-doped microcrystalline Si, *Philosophical Magazine B* **48**(5), 431.

S. Hasegawa, E. Fujimoto, T. Inokuma, and Y. Kurata (1995), Structure and grain boundary defects of glow-discharge polycrystalline silicon films deposited using disilane, *Journal of Applied Physics* **77**(1), 357.

M. Hirose, M. Taniguchi, and Y. Osaka (1979), Electronic properties of chemically deposited polycrystalline silicon, *Journal of Applied Physics* **50**(1), 377.

M. Hoheisel, R. Carius, and W. Fuhs (1983), Low temperature photoconductivity in a-Si:H films, *Journal of Non-Crystalline Solids* **59 & 60**, 457.

M. Hoheisel, R. Carius, and W. Fuhs (1984), Photoconductivity and photoluminescence of a-Si:H at low temperature, *Journal of Non-Crystalline Solids* **63**, 313.

E. Holzenkämpfer, F. Richter, J. Stuke, and U. Voget-Grote (1979), Electron spin resonance and hopping conductivity of a-SiO_x, *Journal of Non-Crystalline Solids* **32**, 327.

A. Honig (1961), Infrared pumped paramagnetic excited state in phosphorus-doped silicon, *Bulletin of the American Physical Society* **6**, 118.

L. Houben (1995), *Strukturelle Eigenschaften von mikrokristallinem Silizium im Übergang zwischen mikrokristallinem und amorphem Wachstum*, Diplomarbeit, Heinrich-Heine-Universität Düsseldorf.

L. HOUBEN (1998), private communication.

L. HOUBEN, M. LUYSBERG, P. HAPKE, R. CARIUS, F. FINGER, AND H. WAGNER (1998), Structural investigations of microcrystalline silicon in the transition from highly crystalline to amorphous growth, *Philosophical Magazine A*, in press.

N. ISHII, M. KUMEDA, AND T. SHIMIZU (1981), The g-values of defects in amorphous C, Si and Ge, *Japanese Journal of Applied Physics* **20**(9), L673.

D. JÉROME AND J. M. WINTER (1964), Electron spin resonance on interacting donors in silicon, *Physical Review* **134**(4A), A1001.

D. JOUSSE, S. L. DELAGE, AND S. S. IYER (1991), Grain-boundary states and hydrogenation of fine-grained polycrystalline silicon films deposited by molecular beams, *Philosophical Magazine B* **63**(2), 443.

C. P. KEIJZERS, E. J. REIJERSE, AND J. SCHMIDT (eds.) (1989), *Pulsed ESR: A New Field of Applications*, North Holland, Amsterdam.

H. KODERA (1964), Effect of doping on the electron spin resonance in phosphorus doped silicon, *Journal of the Physical Society of Japan* **19**(6), 915.

H. KODERA (1966), Effect of doping on the electron spin resonance in phosphorus doped silicon. II, *Journal of the Physical Society of Japan* **21**(6), 1040.

H. KODERA (1969), Effect of doping on the electron spin resonance in phosphorus doped silicon. III. Absorption intensity, *Journal of the Physical Society of Japan* **26**(2), 377.

H. KODERA (1970), Dyson effect in the electron spin resonance of phosphorus doped silicon, *Journal of the Physical Society of Japan* **28**(1), 89.

W. KOHN (1957), Shallow impurity states in silicon and germanium, in: F. Seitz and D. Turnbull (eds.), *Solid State Physics*, vol. 5, p. 258, Academic Press, New York.

M. KOHYAMA AND R. YAMAMOTO (1994), Theoretical study of grain boundaries in Si: effects of structural disorder on the local electronic structure and the origin of band tails, *Physical Review B* **50**(12), 8502.

M. KOLTER (1997), *Herstellung und Charakterisierung von a-Si:H/c-Si Heterostruktur-Solarzellen*, Ph.D. thesis, Rheinisch-Westfälische Technische Hochschule Aachen, published as: Berichte des Forschungszentrums Jülich, No. 3471, ISSN 0944–2952.

M. KONDO, T. NISHIMIYA, K. SAITO, AND A. MATSUDA (1998), Light induced phenomena in microcrystalline silicon, *Journal of Non-Crystalline Solids*, in press.

G. LANCASTER, J. A. VAN WYK, AND E. E. SCHNEIDER (1964), Spin-lattice relaxation of conduction electrons in silicon, *Proceedings of the Royal Physical Society* **84**, 19.

D. LANZ (1995), *Spinabhängiger Transport in mikrokristallinem Silizium*, Diplomarbeit, Technische Universität München.

D. J. Lépine (1970), Spin resonance of localized and delocalized electrons in phosphorus-doped silicon between 20 and 30 °K, *Physical Review B* **2**(7), 2429.

K. Lips, P. Kanschat, D. Will, C. Lerner, and W. Fuhs (1998), ESR and transport in microcrystalline silicon, *Journal of Non-Crystalline Solids*, in press.

G. Lucovsky, C. Wang, M. J. Williams, Y. L. Chen, and D. M. Maher (1993), Transport and microstructure of microcrystalline silicon alloys, *Materials Research Society Symposium Proceedings* **283**, 443.

G. W. Ludwig and H. H. Woodbury (1962), Electron spin resonance in semiconductors, in: F. Seitz and D. Turnbull (eds.), *Solid State Physics*, vol. 13, p. 223, Academic Press, New York.

M. Luysberg, P. Hapke, R. Carius, and F. Finger (1997), Structure and growth of μc-Si:H: Investigation by TEM and Raman spectroscopy of films grown at different plasma excitation frequencies, *Philosophical Magazine A* **75**(1), 31.

S. Maekawa and N. Kinoshita (1964), Electron spin relaxation time of heavily P^{31} doped silicon, *Journal of the Physical Society of Japan* **19**, 2240.

S. Maekawa and N. Kinoshita (1965), Electron spin resonance in phosphorus doped silicon at low temperatures, *Journal of the Physical Society of Japan* **20**(8), 1447.

C. Malten (1996), *Pulsed Electron Spin Resonance of Amorphous and Microcrystalline Semiconductors*, Ph.D. thesis, Rheinisch Westfälische Technische Hochschule Aachen, published as: Berichte des Forschungszentrums Jülich, No. 3273, ISSN 0944-2952.

C. Malten, F. Finger, P. Hapke, T. Kulessa, C. Walker, R. Carius, R. Flückiger, and H. Wagner (1995), Spin resonance studies on free electrons and defects in microcrystalline silicon, *Materials Research Society Symposium Proceedings* **358**, 757.

C. Malten, J. Müller, and F.Finger (1997), Pulsed ESR studies on doped microcrystalline silicon, *physica status solidi* **201b**(2), R15.

C. Malten, R. Carius, F. Finger, and S. Yamasaki (1998), ODMR measurements of microcrystalline silicon, *Materials Research Society Symposium Proceedings*, in press.

P. D. Maycock (ed.) (1998), *PV News* **17**(2), 3.

J. A. McInnes and P. N. Butcher (1979), Numerical calculations of d.c. hopping conductivity, *Philosophical Magazine B* **39**(1), 1.

H. Meier, P. Torres, R. Platz, S. Dubail, U. Kroll, J. Anna Selvan, N. Pellaton Vaucher, C. Hof, H. Keppner, A. Shah, K.-D. Ufert, P. Giannoules, and J. Koehler (1996), On the way towards high efficiency thin film silicon solar cells by the "micromorph" concept, *Materials Research Society Symposium Proceedings* **420**, 3.

E. Mooser (1955), Magnetic susceptibility of impurity-trapped electrons and holes in semiconductors, *Physical Review* **100**(6), 1589.

K. MORIGAKI AND S. MAEKAWA (1972), Electron spin resonance studies of interacting donor clusters in phosphorus-doped silicon, *Journal of the Physical Society of Japan* **32**(2), 462.

M. MOROOKA, M. TOKITA, T. KATO, AND I. TSURUMI (1994), Temperature dependence of ESR lines related to phosphorous in silicon, *Japanese Journal of Applied Physics* **33**(4A), 1872.

A. H. MORRISH (1965), *The Physical Principles of Magnetism*, John Wiley & Sons, New York.

N. F. MOTT (1956), On the transition to metallic conduction in semiconductors, *Canadian Journal of Physics* **34**, 1356.

N. F. MOTT (1968), Conduction in glasses containing transition metal ions, *Journal of Non-Crystalline Solids* **1**, 1.

N. F. MOTT AND E. A. DAVIS (1979), *Electronic Processes in Non-Crystalline Materials*, Clarendon Press, Oxford.

A. MÜCK (1997), private communication.

H. NAGASHIMA AND H. YAMASAKI (1976), Electron spin relaxation time of phosphorus-doped silicon, *Journal of the Physical Society of Japan* **41**(2), 711.

H. NEUBRAND (1978), ESR from boron in silicon at zero and small external stress, *physica status solidi (b)* **86**, 269.

J. W. ORTON AND M. J. POWELL (1980), The Hall effect in polycrystalline and powdered semiconductors, *Reports on Progress in Physics* **43**, 1263.

H. OVERHOF AND M. OTTE (1997), Theoretical investigations of models for the electronic transport in microcrystalline silicon films, in: J. M. Marshall, N. Kirov, A. Vavrek, and J. M. Maud (eds.), *Future Directions in Thin Film Science and Technology*, p. 23, World Scientific, Singapore.

H. OVERHOF AND P. THOMAS (1989), *Electronic Transport in Hydrogenated Amorphous Semiconductors*, Springer, Berlin.

S. R. OVSHINSKI (1985), The chemical and configurational basis of high efficiency amorphous photovoltaic cells, in: *Proceedings of the 18th IEEE Photovoltaic Specialists Conference*, p. 1365, Las Vegas.

M. A. PAALANEN, S. SACHDEV, AND R. N. BHATT (1986), Spin dynamics of nearly localized electrons, *Physical Review Letters* **57**(16), 2061.

G. E. PAKE AND T. L. ESTLE (1973), *The Physical Principles of Electron Paramagnetic Resonance*, W. A. Benjamin, Inc., Reading.

W. PAULI (1927), Über Gasentartung und Paramagnetismus, *Zeitschrift für Physik* **41**, 81.

G. PICUS, E. BURSTEIN, AND B. HENVIS (1956), Absorption spectra of impurities in silicon - II. Group-V donors, *Physics and Chemistry of Solids* **1**, 75.

C. P. Poole and H. A. Farach (1971), *Relaxation in Magnetic Resonance*, Academic Press, New York, London.

C. P. Poole, Jr. (1982), *Electron Spin Resonance*, Wiley-Interscience, New York.

C. P. Poole, Jr. and H. A. Farach (1987), *Theory of Magnetic Resonance*, John Wiley & Sons, New York.

A. Portis, A. Kip, C. Kittel, and W. Brattain (1953), Electron spin resonance in a silicon semiconductor, *Physical Review* **90**, 988.

J. D. Quirt and J. R. Marko (1973), Absolute spin susceptibilities and other ESR parameters of heavily doped n-type silicon. II. A unified treatment, *Physical Review B* **7**(8), 3842.

C. H. Seager and T. G. Castner (1978), Zero-bias resistance of grain boundaries in neutron-transmutation-doped polycrystalline silicon, *Journal of Applied Physics* **49**(7), 3879.

J. W. Seto (1975), The electrical properties of polycrystalline silicon films, *Journal of Applied Physics* **46**(12), 5247.

B. I. Shklovskii and A. L. Efros (1984), *Electronic Properties of Doped Semiconductors*, Springer, Berlin.

C. Slichter (1990), *Principles of Magnetic Resonance*, Springer, Berlin.

C. P. Slichter (1955), Spin resonance of impurity atoms in silicon, *Physical Review* **99**(2), 479.

W. E. Spear, G. Willeke, and P. G. LeComber (1983), Electronic properties of microcrystalline silicon prepared in the glow discharge plasma, *Physica* **117B & 118B**, 908.

A. Stesmans and G. De Vos (1986), ESR observation of temperature-dependent g shifts in submetallic P-doped Si at low temperatures, *Physical Review B* **34**(9), 6499.

H. Stiebig (1997), *Entwicklung und Beschreibung von optoelektronischen Bauelementen auf der Basis amorphen Siliziums*, Ph.D. thesis, Rheinisch-Westfälische Technische Hochschule Aachen, published as: Berichte des Forschungszentrums Jülich, No. 3464, ISSN 0944–2952.

H. Stiebig, D. Knipp, P. Hapke, and F. Finger (1998), Three color piiin-detector using microcrystalline silicon, *Journal of Non-Crystalline Solids*, in press.

R. Street (1991), *Hydrogenated Amorphous Silicon*, Cambridge University Press, Cambridge.

R. A. Street and D. K. Biegelsen (1980a), Explanation of light induced ESR in a-Si:H; dangling bonds with a positive correlation energy, *Journal of Non-Crystalline Solids* **35 & 36**, 651.

R. A. Street and D. K. Biegelsen (1980b), Luminescence and ESR studies of defects in hydrogenated amorphous silicon, *Solid State Communications* **33**, 1159.

R. A. Street and D. K. Biegelsen (1982), Distribution of recombination lifetimes in amorphous silicon, *Solid State Communications* **44**(4), 501.

R. A. STREET AND D. K. BIEGELSEN (1984), The spectroscopy of localized states, in: J. D. Joannopoulos and G. Lucovsky (eds.), *The Physics of Hydrogenated Amorphous Silicon II — Electronic and Vibrational Properties*, Topics in Applied Physics, p. 195, Springer, Berlin.

M. STUTZMANN (1983), *Lokalisierte Zustände in amorphem Germanium und Silizium*, Ph.D. thesis, Philipps-Universität Marburg.

M. STUTZMANN (1987), On the structure of dangling bond defects in silicon, *Zeitschrift für Physikalische Chemie, Neue Folge* **151**, 211.

M. STUTZMANN AND D. BIEGELSEN (1988), The microscopic structure of defects in a-Si:H and related materials, in: H. Fritzsche (ed.), *Amorphous Silicon and Related Materials*, pp. 557–594, World Scientific, Singapore.

M. STUTZMANN, D. K. BIEGELSEN, AND R. A. STREET (1987), Detailed investigation of doping in hydrogenated amorphous silicon and germanium, *Physical Review B* **35**(11), 5666.

M. STUTZMANN, C. P. HERRERO, M. INGELS, AND A. BREITSCHWERDT (1989), Hydrogen passivation of doped and undoped microcrystalline silicon, *Materials Research Society Symposium Proceedings* **164**, 189.

M. TANIGUCHI, M. HIROSE, Y. OSAKA, S. HASEGAWA, AND T. SHIMIZU (1980), Current transport in doped polycrystalline silicon, *Japanese Journal of Applied Physics* **19**(4), 665.

C. TSAI (1988), Plasma deposition of amorphous and crystalline silicon: the effect of hydrogen on the growth, structure and electronic properties, in: H. Fritzsche (ed.), *Amorphous Silicon and Related Materials*, p. 123, World Scientific, Singapore.

H. UE AND S. MAEKAWA (1971), Electron-spin-resonance studies of heavily phosphorus-doped silicon, *Physical Review* **3**(12), 4232.

S. USUI AND M. KIKUCHI (1979), Properties of heavily doped gd-Si with low resistivity, *Journal of Non-Crystalline Solids* **34**, 1.

S. VEPŘEK AND V. MAREČEK (1968), The preparation of thin layers of Ge and Si by chemical hydrogen plasma transport, *Solid-State Electronics* **11**, 683.

H. J. VON BARDELEBEN, C. ORTEGA, A. GROSMAN, V. MORAZZANI, J. SIEJKA, AND D. STIEVENARD (1993), Defect and structure analysis of n^+-, p^+- and p-type porous silicon by the electron spin resonance technique, *Journal of Luminescence* **57**, 301.

J. WERNER AND M. PEISL (1985a), Exponential band tails at silicon grain boundaries, *Materials Research Society Symposium Proceedings* **46**, 575.

J. WERNER AND M. PEISL (1985b), Exponential band tails in polycrystalline semiconductor films, *Physical Review B* **31**(10), 6881.

J. H. WERNER (1989), Band tailing in polycrystalline and disordered silicon, in: J. H. Werner, H. J. Möller, and H. P. Strunk (eds.), *Polycrystalline Semiconductors*, vol. 35 of *Springer Proceedings in Physics*, pp. 345–351, Springer, Berlin.

D. Will (1996), *ESR und EDMR an mikrokristallinem Silizium*, Diplomarbeit, Philipps-Universität Marburg.

D. Will, C. Lerner, W. Fuhs, and K. Lips (1997), Transport and recombination channels in undoped microcrystalline silicon studied by ESR and EDMR, *Materials Research Society Symposium Proceedings* **467**, 361.

G. Willeke (1983), *The structural and electronic properties of μc-Si produced in the glow discharge plasma*, Ph.D. thesis, University of Dundee, unpublished.

G. Willeke (1992), Physics and electronic properties of microcrystalline semiconductors, in: J. Kanicki (ed.), *Amorphous and Microcrystalline Semiconductor Devices. Volume II: Materials and Device Physics*, p. 55, Artech House, Boston.

G. Willeke, W. Spear, D. Jones, and P. L. Comber (1982), Thermoelectric power, Hall effect and density-of-states measurements on glow-discharge microcrystalline silicon, *Philosophical Magazine B* **46**(2), 177.

X. Xu, J. Yang, A. Banerjee, S. Guha, K. Wasnath, and S. Wagner (1995), Band edge discontinuities between microcrystalline and amorphous hydrogenated silicon alloys and their effect on solar cell performance, *Applied Physics Letters* **67**(16), 2323.

S. Yamasaki, J. Lee, T. Umeda, J. Isoya, and K. Tanaka (1996), Spatial distribution of phosphorus atoms surrounding spin centers of P-doped hydrogenated amorphous silicon elucidated by pulsed ESR, *Journal of Non-Crystalline Solids* **198–200**, 330.

J. Yang, R. Ross, T. Glatfelder, R. Mohr, G. H. A. Bernotaitis, E. Chen, J. Burdick, M. Hopson, and S. Guha (1988), High efficiency multi-junction solar cells using amorphous silicon and amorphous silicon-germanium alloys, in: *Proceedings of the 20th IEEE Photovoltaic Specialists Conference*, p. 241, Las Vegas.

J. Yang, A. Banerjee, T. Glatfelter, S. Sugiyama, and S. Guha (1998), Recent progress in amorphous silicon alloy leading to 13 % stable cell efficiency, in: *Proceedings of the 26th IEEE Photovoltaic Specialists Conference*, p. 563, Anaheim.

C. Young, E. Poindexter, and G. Gerardi (1997a), Electron paramagnetic resonance of porous silicon: observation and identification of conduction-band electrons, *Journal of Applied Physics* **81**(11), 7468.

C. Young, E. Poindexter, G. Gerardi, W. Warren, and D. Keeble (1997b), Electron paramagnetic resonance of conduction-band electrons in silicon, *Physical Review B* **55**(24), 16245.

Acknowledgements

I would like to express my thanks to Prof. Dr. Heribert Wagner and Prof. Dr. Hans Lüth for providing the possibility to participate in the research activities of the Institute of Thin Film and Ion Technology. I am especially thankful to Prof. Dr. Wagner for his permanent interest and support as head of the photovoltaics group.

For numerous helpful discussions and for critically revising parts of the manuscript I thank Dr. Reinhard Carius. His profound knowledge was invaluable to resolve many critical questions.

Dr. Claus Malten helped me a lot in getting acquaintanced with the measurement technique and data analysis, developed very important data conversion software and resolved many questions I had on ESR. I wish to thank him very much for his friendship and helpfulness.

I am also thankful to Lothar Houben for the detailed and competent information on TEM measurements, for kindly providing the TEM micrographs and for carefully reading parts of the manuscript.

The discussions with Prof. Dr. Harald Overhof were very important and are gratefully appreciated.

I thank Dr. Peter Hapke for Raman, Nils Harder for Hall effect and Horst Holzbrecher, Uwe Zastrow and Andreas Mück for SIMS measurements.

Melanie Schmitt, Dr. Bernd Rech and Oliver Kluth carefully revised the final manuscript and I am very grateful for this.

Dr. Bernd Rech also helped me a lot by passing on his experience with the LaTeX text processing system and Stephan Wieder installed it on my home computer. I appreciate their help very much.

For technical assistance and many instructive discussions I thank Dana Steinbacher, Johannes Wolff, Thomas Kulessa and Andreas Lambertz.

I am also grateful to Resi Nieveler and Willi Hilgers for their help concerning electronics and computers.

Andrea Mülheims was very helpful with all kinds of organizational and administrative problems and I thank her for this.

I would further like to express my thanks to all my friends and colleagues of the photovoltaics group. Without their support in numerous 'every-day' problems and the very friendly and personal atmosphere this work would surely not have been successful.

In particular, I thank Dietmar Knipp for giving me a ride many times and my long-time room-mate and friend Dietmar Lundszien who was permanently interested in my work, kept me up-to-date concerning solar energy and always had a nice drawing at hand to cheer me up.

Last, but not at all least, I would like to thank Dr. Friedhelm Finger for his scientific and personal support throughout this work. I gained a lot from his critical (but always constructive) comments, his view for the important things and his great experience and scientific knowledge. It was fun working with Dr. Finger and I could always rely on his help and support. For this I thank him very much.

I dedicate this work to my parents.

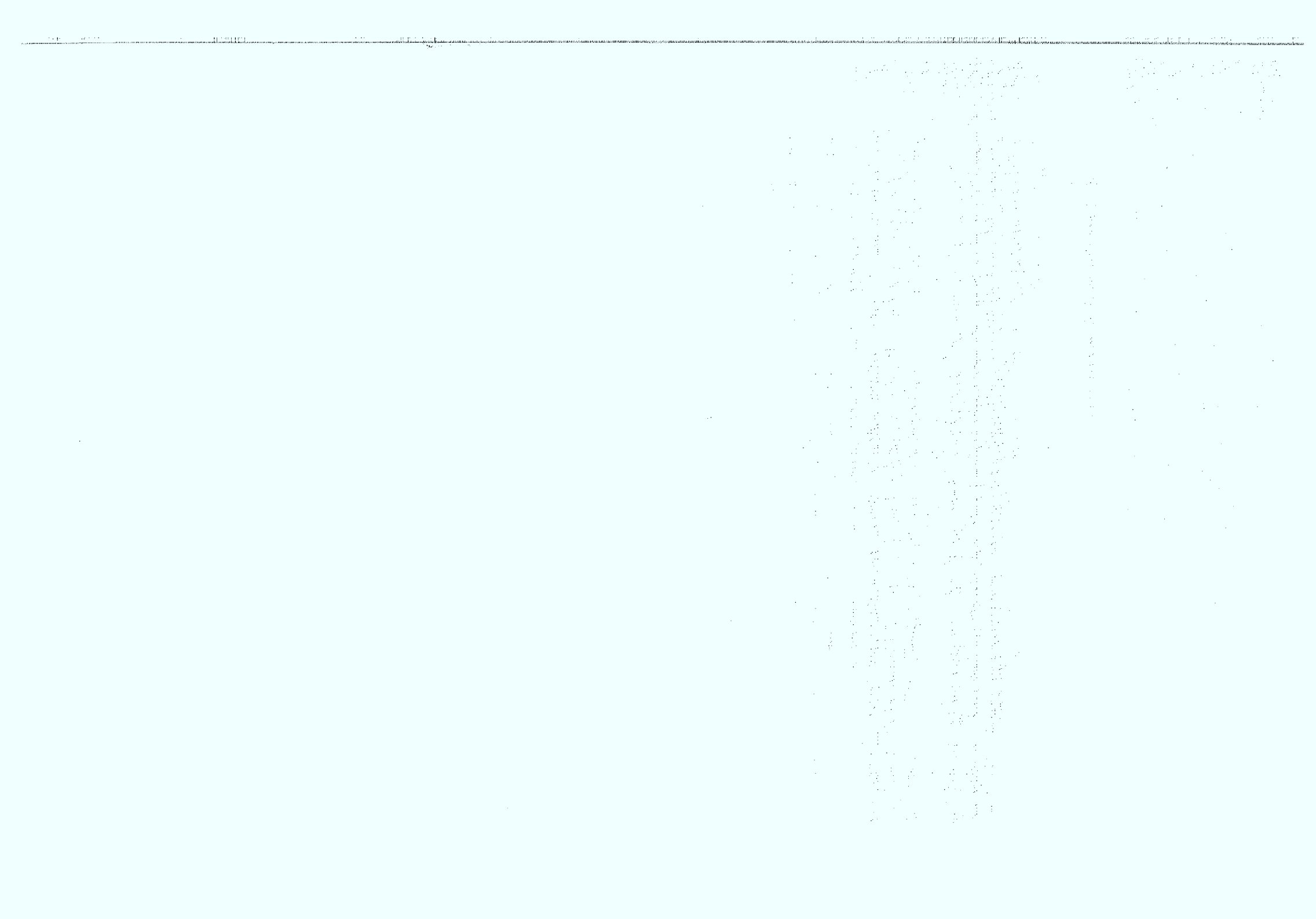

Forschungszentrum Jülich

Jül-3615
December 1998
ISSN 0944-2952